Dynamic Properties of Hybrid Composite Hollow Cylinders: Application for Bicycle Handlebars

Katherine Hay
Mechanical Engineering
McGill University, Montreal

December, 2014

A thesis submitted to McGill University in partial fulfillment of the requirements of the degree of Masters in Engineering (MEng).

I. Table of Contents

II. List of Tables

III. List of Figures

IV. Abstract

Dynamic properties of materials are of special interest to the sports industry, where strength and damping are required for optimal feel and performance. Hybrid composites made of synthetic carbon and natural flax fiber reinforcement were studied for dynamic performance optimization, for the purpose of a mountain bicycle handlebar. Hybrid laminate configurations were first optimized through modeling of handlebar behaviour to ensure the designs met required strength specifications. The effect of flax layer placement and multiple flax layers were experimentally determined through multiple dynamic testing methods in the free-free and clamped boundary conditions. The through-thickness strain energy density was modeled for all laminates to determine the relationship between the observed damping behaviour and the prominent damping mechanisms. Based on the observed dynamic behaviour and modeled strain energy density, an optimal layup was proposed for the handlebar. The design static strength requirements were verified through modeling, and a prototype handlebar was successfully manufactured. The study shows that the hybrid laminate design can be tailored to optimize the damping characteristics of a structure without compromising strength.

KEYWORDS: Natural fibers; hybrid composites; dynamic properties; strain energy density; bicycle handlebars

V. Résumé

Les propriétés dynamiques des matériaux sont d'un intérêt particulier pour l'industrie du sport, où la raideur et l'amortissement sont nécessaires pour toucher et des performances optimales. Des matériaux composites hybrides avec renforcement en carbone et fibre de lin naturel synthétique ont été étudiés pour l'optimisation des performances dynamiques, dans le but de produire un guidon de vélo de montagne. Les stratifiés hybrides ont été optimisés grâce à la modélisation du comportement du guidon pour assurer la conception est conforme aux spécifications de résistance requises. L'effet de la mise en place de la couche de lin et de multiples couches de lin ont été déterminées expérimentalement par de multiples méthodes d'essai dynamique et deux différentes conditions limites. La densité d'énergie dans la direction de l'épaisseur a été modélisé pour tous les stratifiés afin de déterminer la relation entre le comportement observé d'amortissement et les mécanismes d'amortissement de premier plan. Sur la base du comportement dynamique observée et la densité d'énergie de déformation modélisée, un laminé optimal a été proposé pour la conception du guidon. Les exigences de résistance statique de conception ont été vérifiés par la modélisation, et un guidon prototype a été fabriqué avec succès. L'étude démontre que la conception du stratifié hybride peut être adapté pour optimiser les caractéristiques d'amortissement d'une structure sans compromettre la solidité.

MOTS-CLÉS: fibres naturelles; composites hybrides; propriétés dynamiques; souche densité d'énergie; guidon de vélo

VI. Acknowledgements

The author of this thesis would like to thank the following individuals for their support and encouragement in the pursuit of this project:

- Julien Rion and Christian Fischer of BComp, Switzerland for supplying the flax material used in this study as well as their encouragement and support
- The Composites Group at KU Leuven, Belgium, and especially Dr. Joris Baets and Dr. Aart van Vuure for their support and encouragement, and for allowing me the opportunity to experience an exchange to utilize their expertise and equipment.
- Mr. Daniele Brandoliso and Mr. Akhilesh Swarnakar of KU Leuven for their help in conducting the dynamic testing

Last but not least, Prof. Larry Lessard for supervising me and encouraging me in this project, and the rest of the Composites Group at McGill.

1 Introduction

With the advent of composite materials, bicycle design evolved to optimize the stiffness-to-weight ratio of the bicycle to maximize cyclist power transfer. As strength and damping are nonsynchronous material properties, this focus has come at the cost of damping, increasing the vibrations transferred to the rider and perceived discomfort. This exemplifies the interest of the sports industry in dynamic properties, as both damping and strength are required for optimal feel and performance. One method of improving damping behaviour while maintaining strength is to add a compliant layer or core to the laminate, such as a natural fiber composite. Development in natural fiber composites continues to grow, predominately driven by the automobile industry and environmental concerns. However, there is little information available regarding the dynamic behaviour of natural fiber composites, and very little with regards to hybrid synthetic/natural fiber composite behaviour.

The motivation behind this study was thus multi-fold. First, identifying the knowledge gap in hybrid composite dynamic performance, interest was generated to investigate and determine the effect of flax layer placement and the number of flax layers in a hybrid composite on the dynamic properties. By investigating a complex structure such as a hollow cylinder, the investigation would yield unique and novel results and further the understanding of these materials in the literature. Second, by optimizing the chosen hybrid laminates, it was desired to improve upon the existing bicycle handlebar design for cyclist comfort. The strength requirements are critical in a mountain bicycle handlebar due to their loading and use and it was of great interest to determine if the design challenge of maintaining strength while optimizing damping behaviour could be achieved through hybrid composites. Third, subsequent to the study results, it was desired to build a prototype handlebar to determine if what was predicted to be optimal could be manufactured.

1.1 Objectives

The guiding purpose of this investigation was to optimize a hybrid composite laminate for dynamic performance while maintaining strength requirements. This was proposed to be achieved in stages, each with their own purpose as described below:

1) *Determine the static strength characteristics of the pure carbon fiber and flax fiber composites:* This was identified to determine the effect of the hollow cylinder geometry and unique manufacturing method on the static strength characteristics of the material.
2) *Identify hybrid laminate designs that would meet the static strength requirements for dynamic optimization:* This was identified to ensure that the laminates chosen for further study would meet and exceed the strength requirements of the handlebar.
3) *Determine the effect of flax layer position and number of flax layers on dynamic performance:* This was identified to experimentally validate the optimization criteria of improving the damping characteristics of the hollow cylinder.
4) *Develop further understanding of the damping mechanisms of the hybrid composites:* This was identified as a major objective as very little was known about the mechanisms of damping. By modeling the through-thickness strain energy density of the experimental hybrid composites, it was hypothesized that patterns in total strain energy density and through-thickness strain energy distribution would lead to general conclusions about the prominent mechanisms of hybrid composite damping
5) *Verification of optimized laminate and manufacture of a prototype handlebar:* Subsequent to the analysis, verification of the proposed design hybrid composite handlebar was determined to be critical to ensure static strength requirements were met. Finally, manufacturing of the novel hybrid composite handlebar was desired to ensure that the proposed design was achievable.

1.2 Thesis Organization

The thesis is organized in the order of the design process, to highlight the building of the hybrid laminate behaviour documentation and final design recommendations. The thesis begins with **Section 2**, a comprehensive literature review of the state of knowledge of natural fiber composites and hybrid composites. The literature review then focuses on vibration theory. Finally, bicycle design, and methods of evaluating vibration and cyclist discomfort are discussed, and the benchmark bicycle design and laminate are described. **Section 3** describes the manufacturing process for both the hollow cylinders and the prototype handlebar. **Section 4** describes the static mechanical properties investigation, and documents the results of the tensile and compressive strength tests. The results are compared to literature, and the effect of the geometry and manufacturing process are determined. **Section 5** begins the hybrid composite dynamic characterization. First, the optimization process to select the set of hybrid composites is described. The final hybrid composite experimental groups are then chosen and tested using three different dynamic test procedures and two different boundary conditions. The resulting natural frequencies and damping factors are then compared. From this analysis recommendations are made as to the best experimental procedure to determine dynamic properties as well as the effect of boundary condition on the dynamic behaviour. Subsequent to experimental testing, this section then describes the model results of the through-thickness strain energy density to identify the predominant damping mechanisms of the hybrid composites. **Section 6** documents the modeled results of the optimized hybrid laminate handlebar as determined from experimental testing. This section also documents the results of the manufactured handlebar prototype, with suggestions for process improvement. Finally, **Section 7** summarizes the body of work and optimized hybrid laminate handlebar, with **Section 8** identifying potential areas of future research.

2 Literature Review

2.1 Natural Fiber Composites

2.1.1 History of Use

Natural fibers have been used in composite structures since 1941, where hemp and flax fiber was used for bodywork of a Henry Ford car (1). Ford claimed that the impact strength of this material was 10 times that of steel (1). However, due to significant variability in performance, synthetic fiber reinforced composites are preferred in industry. Driven predominately by environmental concerns (2,3) as well as fuel prices, oil and gas scarcity, and shortage of wood substitute materials for buildings (4), research on natural fiber composites began again in earnest for their applications in the early 21st century. In 2000, the European automobile industry represented 71% of natural fiber composite use, predominately short fiber flax mats made from textile waste used in door liners, parcel shelves, seat backs, interior sunroof shields, and headrests (1,3). Although the industrial, building, and commercial market sectors have seen a 13% increase in structural natural fiber composite use in the last 10 years (4), it is the European automobile sector that is the primary driver of development. The EU passed the End-of-Use Directive for automobiles in 2005, requiring that vehicles must be constructed of 95% recyclable material, with 85% recoverable through reuse or mechanical recycling by January 1, 2015 (4-7). In 2008 twenty-seven components of the Mercedes S car were composed of natural fibers; in 2009 the first racing car with a natural fiber composite body was developed (4). Also in 2009, the UN declared it “The International Year of Natural Fiber” - an initiative focused on raising global awareness about natural fibers with a focus on market demand (4).

2.1.2 Natural Fiber Classifications and Characteristics

Natural fibers for use in composite materials can come from a variety of sources, as shown below in Figure 1.

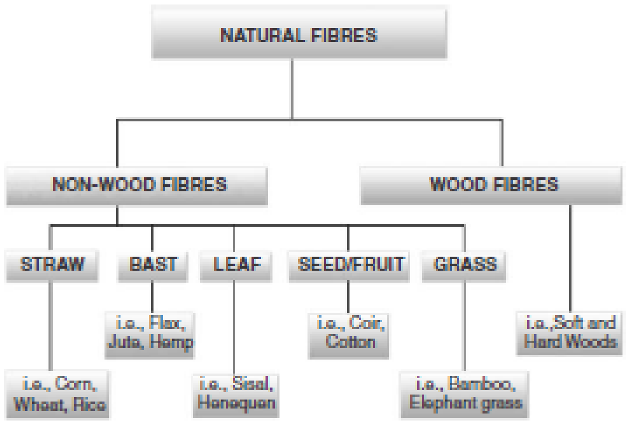

Figure 1 - Classification of Natural Fiber Sources (2)

There are many documented benefits and limitations to using natural fibers in composites, some of which are listed and expanded upon below.

Advantages of Natural Fiber Composites:

- Low density resulting in high specific strength and stiffness (2,4,8-11)
- Environmentally advantageous renewable resource (11); production requires little energy: 1 tonne bast fibers requires 12% of energy required for 1 tonne glass fibers (12); low CO_2 emissions; biodegradable (2,4,9,10,13)
- Low cost renewable resource (2,8-10,13); Low production cost (4)
- Non-abrasive, non-hazardous causing minimal tool wear and skin irritation during manufacturing (2,4,8-10,13)
- Good thermal and acoustic insulating properties (2,4)

Disadvantages of Natural Fiber Composites:

- Low strength, especially impact strength (1,2,4,5,9-12)
- High variability in quality (2,4,5,8-12)
- Hydrophilic properties: Low resistance to moisture (1,2,4,8,14-16); poor adhesion between fibers and hydrophobic matrix (1,4,10,16)
- Poor thermal stability: Restricted maximum processing temperature, as fibers decompose at temperatures greater than 200^{o}C (2,4,5,9-12)
- Lower durability (4)

- Price fluctuation based on harvest results and/or agricultural politics (2,4)
- Poor environmental stability: Degradation due to surrounding environment during use, including effects of humidity, alternate wet/dry cycles, weathering, and biologic attack (3)

2.1.2.1 Structure and Processing of Bast Fibers

Bast fibers themselves are heterogeneous and anisotropic (5). Chemically they are composed of three organic compounds: cellulose microfibril reinforcement, responsible for their tensile properties and lignin/hemicellulose 'cement', responsible for flexibility as well as the hydrophilic nature of the fibers (2,3,13). The structure of a bast fiber is shown in Figure 2 below, illustrating the composite nature of a single fiber.

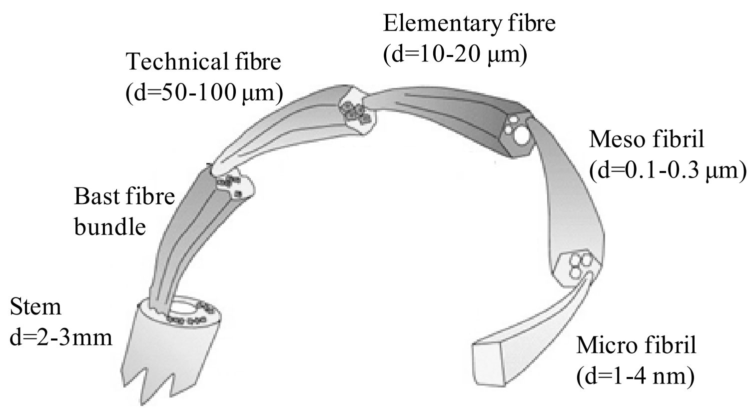

Figure 2 - Schematic of Bast Fiber Structure (17)

In brief, once the bast fibers have reached their mature length, the stems are cut and then undergo retting. Retting is a process that breaks down the chemical bonds that hold the stem together, isolating the flax fiber from the stem (2,14). After retting, the stems are hackled, where the short and long fibers are chemically or mechanically separated, with the long fibers spun into yarns, woven into fabrics, and finished (2,14). This process can have a significant effect on the fiber's properties, as described below.

Harvesting and Processing Factors:

- Geography/location of plant growth: Including growing conditions and environment (1,2,4,8,9,12,14,15)
- Maturity of the plant (2,4,14,15)
- Extraction method and processing (2,4,8,9,12,14,15)
- Geometry of the fiber: Aspect scale (length to width ratio) (3); structure; microfibril angle (2,4,14,15); diameter of fiber (5)
- Location of the fiber harvested on plant (2,4,14,15)
- Degree of moisture in the fiber: Inherent moisture content 8-13% (2,4,8,9,14,15)
- Angle of twist of the yarn: a low twist results in a high fiber stiffness comparable to glass but difficulty in subsequent manufacturing, whereas a high twist allows for easier manufacturing of the fabric but results in lower stiffness and poor wetting (18,19)

All of these factors have a direct impact on the final mechanical properties, including tensile strength, flexural strength, and Young's modulus (2).

2.1.3 Flax Fiber Composites

Flax fibers are of special interest within the bast fiber family, as they exhibit the best material properties and have specific properties comparable to glass/epoxy composites (1,13,18,20). This means that flax has the potential to replace glass fiber composites in stiffness applications, but not in strength applications (20), and are being positioned to appropriately replace glass/epoxy composites (3,8,9). Additionally, of all the natural fibers, flax fibers are the least variable with regards to changes in moisture content (9).

Only 6% of the flax produced is currently used for composite materials (13). Barriers to market penetration include lack of confidence in use and performance, limited understanding of behaviour, and lack of established manufacturing processes (16). In composite materials, load transfer from the matrix to the reinforcing fiber is important when determining the static strength characteristics (8). Due to their hydrophilic nature, flax fibers have poor chemical bonding to the hydrophobic matrix, and thus adhere to the matrix solely through mechanical interaction due to fiber surface roughness (8). Previous research has focused on methods of improving the bond strength between the flax fiber and matrix, to enhance the composite strength properties. It has been shown that the interlaminar bond improves with chemical treatment of the fiber, matrix, or a combination thereof (3,10,12,15). Prepregs, which are sheets of composite material with a reinforcement fabric surrounded by an uncured matrix, are possible after chemical surface treatment of the flax fibers resulting in a better interlaminar bond (11). Prepregs also allow for completely untwisted yarns, which results in the maximum use of the mechanical properties of the flax fibers (11). The final composite product properties are a function of all the mechanical properties and geometric characteristics of the chosen fiber reinforcement, interlaminar bond strength and quality, and the distribution and orientation of fibers (3).

2.1.3.1 Flax Material Properties

As was implied above, there are multiple factors that have an impact on flax fiber composite material performance, in addition to general variability of composite materials due to product manufacturing and processing. Care must be taken when directly comparing published literature mechanical properties, as the post-processing methods, geometry, orientation, and materials will have an effect on the derived material performances. Regardless of the variable performance factors, in general flax composites exhibit the following characteristics. First, flax composites are relatively poor in compression; due to their anisotropic structure they are prone to micro-buckling (18). Second, their interlaminar shear characteristics are comparable to Kevlar/polyethylene composites, and slightly lower than glass/epoxy composites (18). Their performance is also highly dependent on orientation. Due to their yarn structure, misorientation can occur from the micro to macro level: the microfibril angle in a single fiber, the twist of processed fiber yarn, and the macro off-axis loading angle (19). For example, Phillips et. al. (2013) found that the tensile properties of a flax composite decreased by 36% for stiffness and 51% in ultimate tensile strength, as well as an interlaminar shear decrease of 11% and void increase with an increase in crimp of the fiber (11). Voids are especially detrimental to flax composites, and were shown to increase post-cure moisture absorption by 33% (11). This is an example of the effect of post-processing parameters: Phillips et. al. (2013) demonstrated that by varying the pressure only during the cure cycle the void content of the final product ranged from 1-20% (11).

Taking into consideration this high variability and the effect of the final properties, Table 1 below summarizes post-cure mechanical properties of flax/epoxy composites.

Table 1 - Published Flax Prepreg Mechanical Properties

Cure Method/Test Method	Ultimate Tensile Strength [MPa]	Young's Modulus [GPa]	Reference
RTM/DMA	258.8 (1207.7 for Unidirectional Carbon Fiber/Epoxy)	20.2 (101.2 for Unidirectional Carbon Fiber/Epoxy)	Duc et. al. (13)
Vacuum Bag Prepreg/ASTM 3171	286	28.2	Phillips et. al. (2011) (20)

2.1.4 Damping Mechanisms

Composite materials utilize unique mechanisms to achieve damping, due to their anisotropic architecture. Current uses of composite materials in damping applications include automobile bumpers (8), tubes in aerospace, automotive, and civil engineering for energy absorbers, pressure vessels, and pipe lines (21). Damping is of special interest in applications such as sports equipment due to the user's demand for a balance between damping and stiffness for optimal feel and control (13). However, there is little information available comparing the damping performance of natural fibers to that of synthetic fibers (13) and very little in terms of damping of flax tube structures (21).

All composite materials achieve damping through a combination of the following four mechanisms:

1) *Viscoelastic nature of matrix and/or fiber material:* In general, damping is a matrix-dominated property, however more viscoelastic fibers such as carbon and Kevlar have higher damping properties compared to other fibers (21-23).
2) *Interphase disbonding:* For optimal damping, the interface between the fiber and the matrix should be weak. This allows for interlaminar cracking to dissipate energy. However, this compromises strength as the load is no longer transferred from the matrix to the fibers effectively (21-23).
3) *Damping due to damage/crack propagation:* This can be due to frictional damping due to slip in the interphase and/or local areas of high density cracking in the matrix, fibers, or

combination thereof due to local areas of high stress/strain. This viscoplastic behaviour allows for greater energy dissipation in the structure (8,22,24).

4) *Thermoelastic damping:* To a lesser extent, damping can occur due to the cyclic heat flow from a region of compression to tension as a function of load, frequency, laminate thickness, and number of load cycles (22).

Damping may also be promoted by voids (21,23), which may contribute to the weak interphase bond between the fiber and matrix. Most mechanisms are indications of damage in the laminate. Therefore, to increase the damping characteristics, the laminate must decrease in stiffness and strength. This design trade-off should be optimized based on the design requirements of the global static and dynamic structure response, ability to modify the composite laminate, and shape optimization (22). Thus, depending on other structural requirements, to achieve the required damping an additional high-damping layer such as a polymer or the use of hybrid fiber composites may be required (22).

Natural fibers have additional inherent damping mechanisms due to their unique architecture. The fibers themselves are hollow, which results in a decrease in bulk density and act as an acoustic insulator (4,21). They are composite materials in and of themselves, which allow for further energy dissipation in each cell wall and between cells, increasing intrinsic damping (13). This is shown through their unique failure mechanisms which have been observed to include axial splitting along their elementary constituents, radial cracking of the fiber, and multiple fracture sites of elementary fibers (23). Furthermore, the fiber yarn architecture, with the intra/inter yarn friction may contribute further to energy dissipation (13).

There is limited information available regarding the damping properties of continuous natural fiber composites. In their study of the specific energy absorption of woven bast fiber vacuum-assisted Resin Transfer Molding (RTM) specimens, Meredith et. al. (2012) observed that the higher the volume fraction of fiber, the higher the specific energy absorption. This was most likely due to their unique damping mechanisms described above (8). Yan et. al. (2012) studied the damping of plain weave flax composites through impact testing, and observed that chemically treated fibers to improve the interphase bond had a 7.4% decrease in damping characteristics and a higher natural frequency (23). The same authors followed up this study in 2014 by investigating plain weave hollow cylinders (21). In this study they assessed damping of various sizes of tubes through standard vibration test, by exciting the sample with an impact hammer, and the tubes supported by elastics at the node points to replicate the free-free boundary condition. They found that with an increase in tube size the natural frequencies increased and damping factor decreased (21), potentially due to their increased stiffness. More recently, Duc et. al. compared the dynamic behaviour of flax, carbon fiber, and glass fiber fabrics cured with RTM (13). Using Dynamic Modal Analysis (DMA) they found that flax had superior damping properties to both carbon fiber and glass fiber. This behavior was verified in a recent study conducted at McGill, comparing flax prepreg and unidirectional carbon fiber prepreg damping characteristics using DMA (25). Therefore, for design applications such as sports equipment where stiffness and damping are both required, a hybrid composite composed of flax and carbon fiber reinforcement may result in the desired performance.

2.2 Hybrid Composites

A general definition of a hybrid composite is a composite composed of either one fiber reinforcement and a matrix blend, multiple fiber reinforcements in a single matrix, or a combination of the two (4). Hybrid fiber composites are beneficial when the designer wishes to take advantage of the combination of properties from multiple types of fibers, and/or wishes to balance cost and performance of composites (1,4). The result is a unique combination that exhibits a synergistic hybrid effect: the hybrid exhibits better performance than each individual component by itself, and can be tailored for the material requirements of the design application (4). For this study, the hybrid composite is defined as having a synthetic (carbon) and natural (flax) reinforcement system in a common (epoxy) matrix. In general, the hybrid performance is dictated by the rule of mixtures, with the limiting failure strain having the most significant effect on the hybrid performance (4). In addition to the general property dependencies of natural fiber composites described above, hybrids are also dependant on the interface bond between the multiple fiber reinforcement types, the extent of fiber intermingling, and the macro arrangement of fibers (4). One commercial example of a hybrid synthetic/natural fiber composite design is the

Aralite: an off-shore racing boat made of carbon fiber and flax fiber, with 75-80% vol. wt. percent flax fiber for the hull and deck (1).

The performance of carbon/flax hybrids is a new area of research, with few studies documenting performance (26). To the author's knowledge, there are three continuous fiber studies that have been published, investigating the resulting static tensile strength, flexural strength and absorption properties of a single hybrid laminate layup (1,16,26). Two studies examined rectangular plates made of unidirectional (26) and woven (16) prepreg flax with unidirectional carbon fiber. One study was intended for a bone plate, and was designed with a total of 16 flax layers sandwiched between two layers of unidirectional carbon fiber all oriented at 0 degrees, cured under vacuum (26). The second used compression molding to manufacture a 6-ply symmetric layup, with two flax layers sandwiched between two carbon layers, also all oriented at 0 degrees (16). The third study used RTM to manufacture an asymmetric hybrid composed of five woven flax layers and one unidirectional carbon fiber layer, all oriented at 0 degrees (1).

Regardless of the manufacturing method, all studies observed the same hybrid behaviour in testing. All composites showed excellent bonding at the carbon/fiber ply interface (26). The flax layers improved the toughness of the laminate by promoting crack propagation, while the carbon improved the thermal and absorption stability and tested mechanical properties (4,16). Dhakal et. al. found an 11-15% improvement in water absorption resistance and a 282% improvement in the tensile strength compared to pure flax (16). With their RTM samples, Fiore et. al. found a 13-262% improvement in tensile modulus, and a 91-266% improvement in ultimate tensile strength compared to the flax composite (1). The range of improvement was due to the original fiber volume of the flax fibers: the samples which showed the greatest improvement used the flax fabric with an unbalanced weave (i.e. more anisotropic) and lower fiber density. Thus, as is the case with standard composites, the percent fiber volume is important when determine the resulting hybrid performance characteristics. With respect to flexural testing, all observed improvement in flexural strength as well. The hybrid sandwich structures exhibited different load sharing depending on the load applied: for the tensile load, the load was evenly distributed through the thickness resulting in brittle fiber failure (26), whereas for the flexural load, the outer layers experienced more tension/compression and thus for best performance of the hybrid composite, the carbon fiber should be placed in the outer layers with the flax in the centre (16,26). This observation highlights the ceiling effect, where improvement in composite performance is to an extent dependant on the fiber volume fraction ratio of the different fiber reinforcements, with further improvements dependant on the layer placement and orientation.

The above investigations illustrate the potential of synthetic/natural fiber reinforcement hybrid composites. To date, there are no known published results of hybrid composites in complex geometries such as hollow cylinders. Additionally, there are no investigations to date as to the dynamic properties of the hybrid composites, and the resulting design optimization possible with the use of natural and synthetic fibers.

2.3 Dynamic Analysis

2.3.1 Vibration

Vibration analysis is the characterization of a structure which undergoes cyclic motion (27). Under free vibration analysis, the structure's response to cyclic motion can be quantified by determining the resonant (natural) frequencies and damping characteristics. To derive the vibration response, let us first consider a single degree-of-freedom spring-dashpot model as shown below:

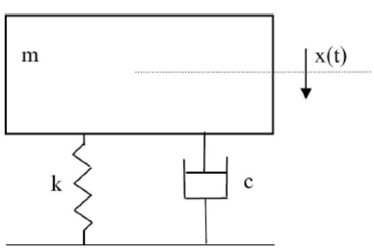

Figure 3 - Single Degree of Freedom Spring-Dashpot Model (28)

The equation of motion for the system can be written as:

$$m\ddot{x}(t) + c\dot{x}(t) + kx(t) = 0 \qquad \textbf{Equation 1}$$

Where 'm' is the mass of the system, 'c' denotes the damping coefficient, and 'k' denotes the spring constant. Solving the characteristic equation in the general case, we obtain:

$$\lambda_{1,2} = -\zeta\omega_n \pm \omega_n\sqrt{\zeta^2 - 1} \qquad \textbf{Equation 2}$$

where ζ is defined as the damping ratio, or c/c_{cr}, and ω_n is the resonant natural frequency of the system. From the above equation, it is evident that the damping ratio determines if the system has real or complex roots. Depending on the roots, the system is classified as under-damped ($0 < \zeta < 1$), critically damped ($\zeta = 1$), or over-damped ($\zeta > 1$). These responses are illustrated below in the time-displacement graph of the simple spring-dashpot system.

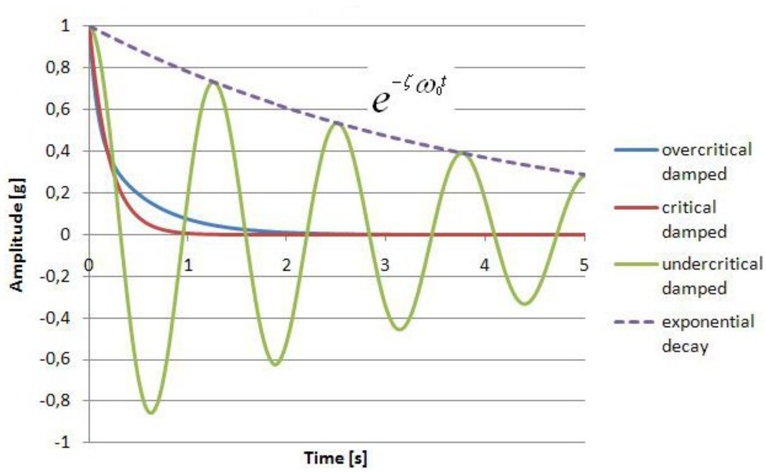

Figure 4 - Time Domain Response of Underdamped, Critical Damped, and Overdamped Vibration Structure Response (28)

From Figure 4 above, we can observe the effect of the damping ratio on the resulting oscillations. The greater the damping ratio, the quicker the structure returns to equilibrium and thus the better the damping response.

Experimental Modal Analysis (EMA) determines dynamic characteristics through vibration testing (27). This can be achieved using multiple methods, dependant on available technology and current standards and developments. However, all EMA systems share the following hardware process flow illustrated below.

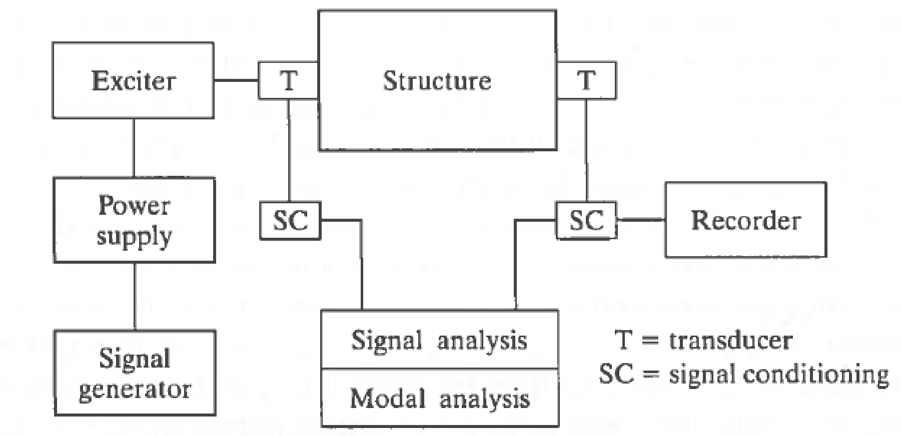

Figure 5 - Schematic of Hardware used in Vibration Testing (27) **(Fig. 7.1, p. 498)**

Often, the EMA signal recorder will convert the recorded signal to a Fast Fourier Transform (FFT), where the user can immediately detect the natural frequencies of the system from the frequency spectra (27). The signal recorder will also record the raw time domain signal, for further processing. In the time domain we can use the logarithmic decrement method to calculate the damping ratio. This method uses the decay envelope of an underdamped system, which has the form of $Ae^{-\xi\omega_n t}$. The logarithmic decrement can thus be defined as:

$$\delta = \ln\left(\frac{x(t)}{x(t+T)}\right) \qquad \textbf{Equation 3}$$

where 'T' is the period of oscillation. Applying this to EMA measurements, one can thus define the logarithmic decrement to be as follows:

$$\delta = \frac{1}{n}\ln\left(\frac{x(t)}{x(t+nT)}\right) = \frac{1}{n}\ln\left(\frac{x(t)}{x(t_n+1)}\right) \qquad \textbf{Equation 4}$$

Where 'n' is an integer denoting the number of successive positive peaks. To decrease the probability of estimation error when using this method, for this analysis 'n' was defined to be the integer where the resulting positive peak magnitude was between 0-0.001. This definition resulted in constant estimation of the damping ratio of the first observed natural frequency. From the logarithmic decrement, one can then defines the damping ratio ζ to be:

$$\varsigma = \frac{\delta}{\sqrt{4\pi^2 + \delta^2}} \qquad \textbf{Equation 5}$$

2.3.2 Through-Thickness Strain Energy Density

In their investigation of the damping behaviour of sandwich-fabric panels, van Vuure et. al. calculated the through-thickness distribution of strain energies in a structure (29). They hypothesized that the higher the strain energy of a compliant layer during bending, the greater the damping effect of the constrained structure. Thus, by examining the through-thickness strain energy and associated loss factor at every natural frequency and mode shape, understanding could be gained of predominate damping mechanisms. In a hybrid composite laminate of carbon fiber and flax, the viscoelastic core is analogous to the flax layers.

In their study of sandwich-fabric beam specimens, they calculated the strain energy density and subsequent loss-factor for the beam in the free-free boundary condition for each identified natural frequency. They noted that for the correlations of damping to be applicable, it is assumed that the mode shapes are independent (i.e. no cross-talk of deformation), and that the deflection is of sinusoidal shape (29). From their study, they found that the sandwich structure should be optimized in terms of stiffness depending on the natural frequencies and mode deflection of interest. For instance, the sandwich structures with a stiff base layer had poor damping at higher frequencies, due to decoupling of the base layer and the skins (29). Thus, they found that the strain energy density was highly dependent on the mode shape of the natural frequency. They also observed that the optimal damping characteristics exhibited by a higher loss factor were achieved with the compliant material located closest to the neutral axis (29).

2.4 Bicycle Design

2.4.1 Assessing Human Comfort and Bicycle Design

Dynamic behaviour of a structure can greatly impact human comfort. In relation to bicycle dynamics, cyclist discomfort is perceived at a certain threshold of vibration transferred at one or more cyclist/bicycle contact points: the hand/handlebar, seat/saddle, and/or foot/pedal (30). In structural analysis, dynamic behaviour can be analyzed by measuring the structural vibration acceleration subsequent to stimulation. Human perception of vibration and associated discomfort is a qualitative property that is subject dependant. Additionally, the human body has a significant range of natural frequencies as well as direction-sensitive responses which compound the measure. To date there is no current standard of natural frequency range or methodology of determining the dynamic behaviour response of a bicycle and the associated cyclist discomfort. Current studies generally employ three methods to assess the bicycle and cyclist interaction: the whole body/hand vibration method as specified by ISO 2631 (31) and ISO 5349 (32) respectively, the absorbed power method (33), and observational studies.

2.4.1.1 Human Vibration Thresholds

Studies investigating human response to vibration started as early as 1818 (33). Previous studies have focused on the general whole body response or localized responses pertaining to occupation, such as tool vibration at the hand/tool interface (34). The human body is a complex organism which has an exceedingly complex dynamic response to vibration (34), and the resulting discomfort is a subjective measure dependant on a variety of physiological and psychological factors (34,35). Griffin summarizes the factors associated with the subjective discomfort due to vibration as follows (34,35):

Extrinsic Variables

- Vibration Variables
  - Magnitude
  - Frequency
  - Direction
  - Input Position
  - Duration
- Other Variables
  - Other Stressors including noise, temperature, etc.
  - Seat Dynamics

Intrinsic Variables

- Intra-Subject Variability
  - Body Posture, Position, and Orientation (sitting, standing, recumbent)
- Inter-Subject Variability
  - Body size and weight
  - Body dynamic response
  - Age and gender
  - Experience, expectation and attitude, personality
  - Fitness

Of the above listed factors relating to human vibration response, the magnitude, frequency, direction, and duration are of key importance (34,35). Multiple vibration sources may also occur simultaneously, which may increase the perceived discomfort (35). The ISO standards are separated by whole body and hand/arm vibration, however both conditions can occur at the same time (34). For instance, on a bicycle whole body vibration is experienced when the body is supported by the seat, and local vibration is experienced at the hand/handlebar contact. The human body is most sensitive to vertical vibrations (34), which implies that in the case of multi-directional vibration the direction with the highest magnitude of oscillation may not be the source of greatest perceived discomfort (34,35). Due to this directional sensitivity, it is common to include weighting factors in the overall assessment of perceived discomfort (31).

The posture and position of the human subject also has a significant effect on the transmitted vibrations. Griffin (1990) found that at higher frequencies, a slight change in subject posture can have a significant effect on the transmitted vibrations, with a much lower impact at lower frequencies (34). Human body parts also have distinct resonance frequencies depending on the position and location of the input (36). These range from 4-8Hz for the trunk to 100-200Hz for the upper jaw (36). One of the most significant sources of perceived discomfort comes from blurred vision (35), with an ocular natural frequency of 60-90Hz (36), dependent upon vibration transmission from the point of contact to the ocular globe. To further compound the issue, there is no standard of agreement of the specific resonant frequencies which are the most likely to cause discomfort due to vibration. As per ISO 2631, the whole body range of discomfort is 0.5-80Hz. Griffin expands the range, stating that 1-100Hz is the threshold of perception of vertical whole-body vibration (34,35). For seated positions, Duarte et. al. observed that subjects appeared to be most sensitive between 10-50Hz, but that 63-80Hz correlated with the natural frequencies of anatomy (36). Griffin disagreed, stating that the seated natural frequency range was between ~4-10Hz (34).

These compounding factors as well as the extrinsic and intrinsic variables which affect the subjective human perception of discomfort led Griffin to conclude that the limits identified in ISO 2631 and ISO 5349 are "illogical and inconsistent" (34) and the best practice of measurement, especially for the hand/tool interface was to measure the acceleration and direction at the point of contact and analyze the data for each specific test condition, as there are too many unknowns in human response for a general procedure to be applicable in all cases (34).

2.4.1.2 Whole Body/Hand Vibration Method

The Whole Body Vibration Method (31) and Hand Vibration Method (32) are the two standardized methods of measuring the vibration effects and human response. Although both have their limitations (34), they are still used today to correlate vibration transmission with human response and thus have been some of the primary methods of evaluation in the study of bicycle behaviour (28,30,37-39). In both methods, the acceleration at the contact points between the structure and the human interface are measured. From these measurements, a correlation between high acceleration and human discomfort is made using a weighted scale average, taking into consideration acceleration direction (28). Thus, the higher the recorded acceleration value, the greater the weighted perceived discomfort at the contact interface.

2.4.1.3 Absorbed Power Vibration Method

The primary difference between the absorbed power method and the ISO standards is that the absorbed power method takes into consideration the magnitude of contact force. Absorbed power is a measure of the average power of the force and velocity of the signal throughout the time period at point of contact. It is a scalar measure, and thus additive. The greater the absorbed power, the greater the human discomfort at the contact point (33). The advantage to this method over the ISO vibration standards is that it takes into consideration the contact force, and thus may be more representative of human discomfort. Qualitatively, if the cyclist is not in contact with the seat, no vibration is transferred at the seat/saddle interface, and thus cyclist comfort is high, contrary to what the ISO methodology may indicate. One limitation to the method is that it is a scalar value, and thus cannot evaluate thus human sensitivity to directional components of acceleration, which has been shown to be significant (34,35,40). However, when compared in case studies evaluating the cyclist discomfort due to bicycle vibration, all cases found that the absorbed power method resulted in a better correlation than the ISO methods between the theoretical level of comfort and qualitative assessment of the test subjects (28,30,37).

2.4.1.4 Alternate Vibration Correlation Methods

As per the recommendation made by Griffin (34), multiple alternate methods evaluating bicycle design parameters and associated cyclist discomfort levels have been used. One theoretical methodology is to stimulate one or more locations of a bicycle frame in isolation with random vertical vibration shakers (28,38,39) a sinusoidal impulse (40), and measure the dynamic response of the structure with accelerometers. This data is then used to draw conclusions regarding the general damping behaviour of the structure, and how it may affect cyclist discomfort.

Alternate studies investigate the whole response of the structure in a controlled environment. The most common methodology is for a small cyclist population to ride specific routes on a variety of different bicycle designs. The variation in vibration input may be modified by changing the riding surface and/or influencing variables such as tire pressure (37,40,41). There is some variability as to the data collected with the road trials. Most consider the acceleration response of the bicycle frame, and may correlate with human threshold values for perceived discomfort (30,37,40, 42). In their study, Seifert et. al. considered the change in human performance by measuring muscle fatigue indicators, changes in time trial performance, and cyclist qualitative assessments of discomfort during the trials (41). These methods are valuable in their role in validating the theoretical response of the bicycle, however due to the significant variability in the model designs and measured parameters, the studies cannot be directly compared and only general conclusions can be drawn.

A third approach that is developing is using finite element analysis (FEA) software to model the dynamic response of the bicycle structure (28,38,40). The developed FEA model can be used both as a predicative tool for behaviour as well as an analysis tool to determine the modal response of the structure post-laboratory tests. Modeling parameters such as the mechanical system used to model the bicycle/cyclist construct, materials used in the model, bicycle design, input stimuli, and boundary conditions significantly affect the model behaviour. Thus, similar to the field trials, studies cannot be directly compared and only general conclusions can be drawn.

Consistent with general studies involving human response to vibration, there is no consensus as to the best practices of measuring and evaluating the dynamic performance of a bicycle. Most studies have been performed for a specific design question, and thus general observations and conclusions as to the various design factors of the bicycles and cyclist discomfort cannot be determined.

2.4.2 Dynamic Properties of Bicycles

2.4.2.1 Holistic Evaluation of Cyclist Comfort

One method to correlate bicycle vibration to cyclist discomfort is to investigate the whole bike structure and qualitative cyclist discomfort response in a controlled environment. Mortier investigated the relative discomfort at the seat and handlebar of a single bicycle design, and varied vibration transmission by varied tire pressures and road track surfaces (37). Using the absorbed power method, the cyclist was most sensitive to vibration changes at the handlebar/hand interface, with no correlation with ISO methods. Mortier concluded that this was due to the consideration of contact force in the absorbed power method.

Richard, S. et. al. (2006) evaluated the holistic bicycle frame with varying fork materials in a laboratory setting, with impulses generated by a custom-designed treadmill surface (42). They then qualitatively correlated measured vibration with cyclist discomfort. Contrary to Mortier, they observed that although cyclist discomfort thresholds were highly variable, only one cyclist was sensitive enough to perceive varying fork compliance, whereas all subjects were sensitive to the bicycle frame behaviour. They conclude that to improve the cyclist comfort, the best method would be to improve the compliance of the bicycle frame.

Using a performance based physiological approach, Seifert et. al. assessed various mechanical dampener fame designs and compared to a rigid frame on a variety of terrain (41). Performance factors included muscle fatigue, time trials, and qualitative rankings of discomfort. All performance factors improved with mechanical dampening; however there was no statistical difference between front fork suspension and full suspension for mountain bicycle courses. In the cross-country course, the time trial performance of the fork suspension was significantly faster than that of the full suspension. They hypothesize that the front suspension allows for sufficient vibration damping to allow the cyclist to maintain pedal cadence with maximum power transfer, while the full suspension may be too compliant, and result in net power loss due to power absorption of the rear suspension (43). As expected, qualitative cyclist discomfort was least with the full suspension, regardless of performance. By correlating physiological performance markers and qualitative cyclist discomfort levels, Seifert et. al. presented a possible explanation for the apparent dichotomy between Mortier and Richard. By increasing the compliance of the front geometry of the bicycle, performance and cyclist comfort improved significantly, as found by Mortier. The higher compliance whole frame design improved cyclist comfort further, as found by Richard. However, Seifert et. al. correlated this with poorer performance, an important consideration in bicycle design. Therefore, based on these experimental studies, the optimal design trade-off between improving cyclist discomfort and maximizing power transfer is to improve the compliance of the front geometry of the bicycle, while maintaining the rigidity of the frame.

2.4.2.2 Individual Component Design Evaluation

The response of a bicycle to dynamic loading is quite complex when considering the whole bicycle geometry. Thus, some studies focus on isolated bicycle component response, often in a laboratory setting. The limitation of this approach is that it decouples the holistic bicycle behaviour with no method of assessing the overall effect.

Isolating the fork design, it has been shown that when stimulated with a vertical vibration shaker the greater compliance of the fork material, the greater the damping at the handlebar (28,38). Extending their investigation, Richard noted when a cyclist mounted the bicycle apparatus, the damping behaviour of the fork improved. This observation agrees with Mortier's assessment that the absorbed power method is the most appropriate to analyze dynamic behaviour of the bicycle and cyclist discomfort. These results are to be expected from material science, as the greater the compliance of a material the better the damping characteristics. As the forks were tested in isolation, the actual effect of increased compliance and power transfer were not addressed (43).

Modeling studies of the influence of the cyclist hand/handlebar contact have shown that the cyclist has a significant damping effect on the transmitted vibrations, and are most sensitive to vertical vibrations (40). This study agrees with the general human vibration sensitivity planes by Griffin (34). To validate the model, Gribb et. al. performed a limited off-road trial to assess the effect of handlebar stiffness on vibration transmission to the cyclist (40). Agreeing with both holistic (37,41) and isolated (38) results, they observed that an increase in handlebar compliance led to a threefold improvement of ride quality, defined by the magnitude of vibration at the handlebar.

Thrite et. al. studied the effect of vibration at the handlebar and seat, to determine which area of the bicycle had the greatest effect on vibration transmission (39). Two frames of varying compliance were studied in the laboratory, with vertical vibration shaker stimuli and a weighted mass at the seat. Dynamic response of the bicycle was correlated with human comfort by comparing the bike natural frequencies at the handlebar and seat to the human sensitivity thresholds, defined as 4-8Hz at the seat and 8-100Hz at the hand/handlebar interface. Thus, improved compliance at these two regions should be within these frequency ranges, as any gain in compliance outside of these ranges would not affect cyclist comfort but may be detrimental to power transfer. They found that in the low frequency range both materials had low peak vibration values, and were not significantly different. However, in the high frequency range of the handlebar, the frame with greater compliance had a greater number of natural frequencies, all with up to ten times lower peak amplitudes. Thus, from their study they conclude that the cyclist discomfort is greatly reduced at the handlebar with the increase in material compliance, with a lesser effect at the seat (43).

2.4.3 Summary of Bicycle Design and Dynamic Response

As is illustrated in the above case studies, the relationship between cyclist discomfort and the dynamic response of a bicycle is very complex and highly dependent on both the methodology of investigation as well as the method of analysis. Due to the variability in methodology, inter-study correlation is difficult. General conclusions can be drawn, and are as follows. It has been shown that the stiffness of a bike frame should vary to achieve maximum cyclist comfort and power transfer. By correlating dynamic response, qualitative cyclist comfort, and various performance measures, the optimal bike design would have a higher compliant front geometry (fork and/or handlebar) with a stiffer whole frame and rear geometry (37,39-41). This was best illustrated by Seifert et. al., who demonstrated superior performance of the fork suspension design in cross-country trail riding, despite greater qualitative cyclist comfort in the full suspension bicycle. This result illustrates the design trade-off of compliance and comfort and performance (43). The increase in compliance for the front geometry should be within the estimated human threshold frequency range of 8-100Hz (39,43). A design improvement outside of the human threshold frequencies may be detrimental to power transfer and performance with no significant improvement in perceived cyclist comfort.

The correlation between individual component dynamic behaviour, cyclist perceived discomfort, and cyclist performance is critical when analyzing bicycle performance. As was shown in laboratory experiments that neglected cyclist performance, a significant improvement in cyclist comfort is only obtained with increased compliance of the whole bicycle frame (42). This laboratory conclusion has limited applications, as in their field study Seifert et. al. found that although cyclist discomfort was least with a compliant bicycle frame, it decreased performance and thus power transfer. Further highlighting the significance of cyclist contact with bicycle dynamic behavior, the difference in vibration amplitude of the handlebar was shown to significantly decrease with the inclusion of the cyclist (40). Essentially, the cyclist both acts as a dampener of the system as well as the feedback response of perception (43).

Bicycle materials have evolved from isotropic materials such as steel and aluminum to anisotropic composite materials. The composite anisotropy further complicates the relationship between bicycle performance and cyclist discomfort. There has been one study which attempted to establish baseline dynamic material behaviour for the application of bicycles, however due to experimental challenges no carbon fiber characterization was successfully achieved (28). Additionally, the study investigated the performance of flat plates, which are not representative of the basic bicycle tubular geometry. As previously discussed, composite materials can be tailored for their intended application, and by using hybrid composites strength and compliance can be optimized. When using these anisotropic materials, benchmark material behaviour should first be understood prior to testing structural response, effect of cyclist damping on the bicycle structure, and performance testing. By understanding the mechanisms of dynamic behaviour of the anisotropic materials in the basic hollow cylinder geometry, the design cycle of the bicycle could be truncated, with the final design taking advantage of tailored composite design.

2.4.4 Flexural Requirements of Mountain Bike Handlebars: EN 14766-2006

Safety standards and test methods for bicycle design are slowly becoming standardized and more common. The European Commission were the first to adopt such standards, with their standards being the basis for subsequent published ISO requirements. With respect to mountain bicycle handlebar design, the EU directive EN 14766-2006 (6), Section 4.7.6.2 applies. This section pertains to the lateral bending strength of a handlebar when mounted in a stem. The procedure requires the handlebar grips to be oriented perpendicular to the stem plane, and a downward force of 1 000N applied 50mm from the end of the handlebar, as shown below in Figure 6. Failure criteria requires the handlebar to not exhibit cracking or fracture of the handlebar, and the permanent deflection at the point of application of the test force should be less than 15mm (6).

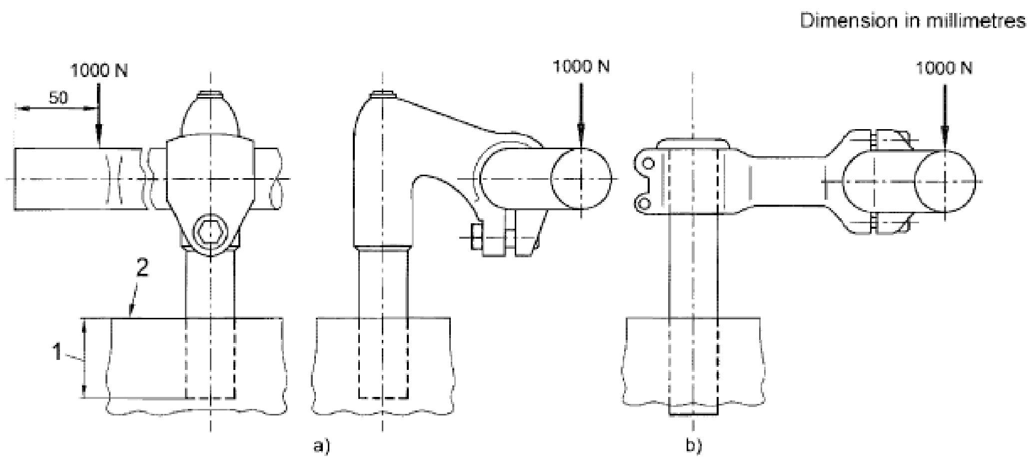

Figure 6 - Handlebar and Stem Assembly for Lateral Bend Test. (6), **Fig. 20**

The standard specifies that the permanent deformation be less than 15mm measured at the point of force application. However, as the handlebar is a cantilever when tested by this method, this does not represent the maximum deflection, which occurs at the end of the handlebar. Thus, for the purposes of this investigation, the maximum end deflection will be used as the pass/fail criteria when comparing the performance of the benchmark handlebar and the hybrid laminates.

2.4.5 Mountain Bicycle Handlebar Benchmark

The mountain bicycle handlebar used for benchmark characterization was the Thomson Flat Carbon Mountain Bike Handlebar (HB-102) (44). The geometry of the handlebar is shown below in Figure 7.

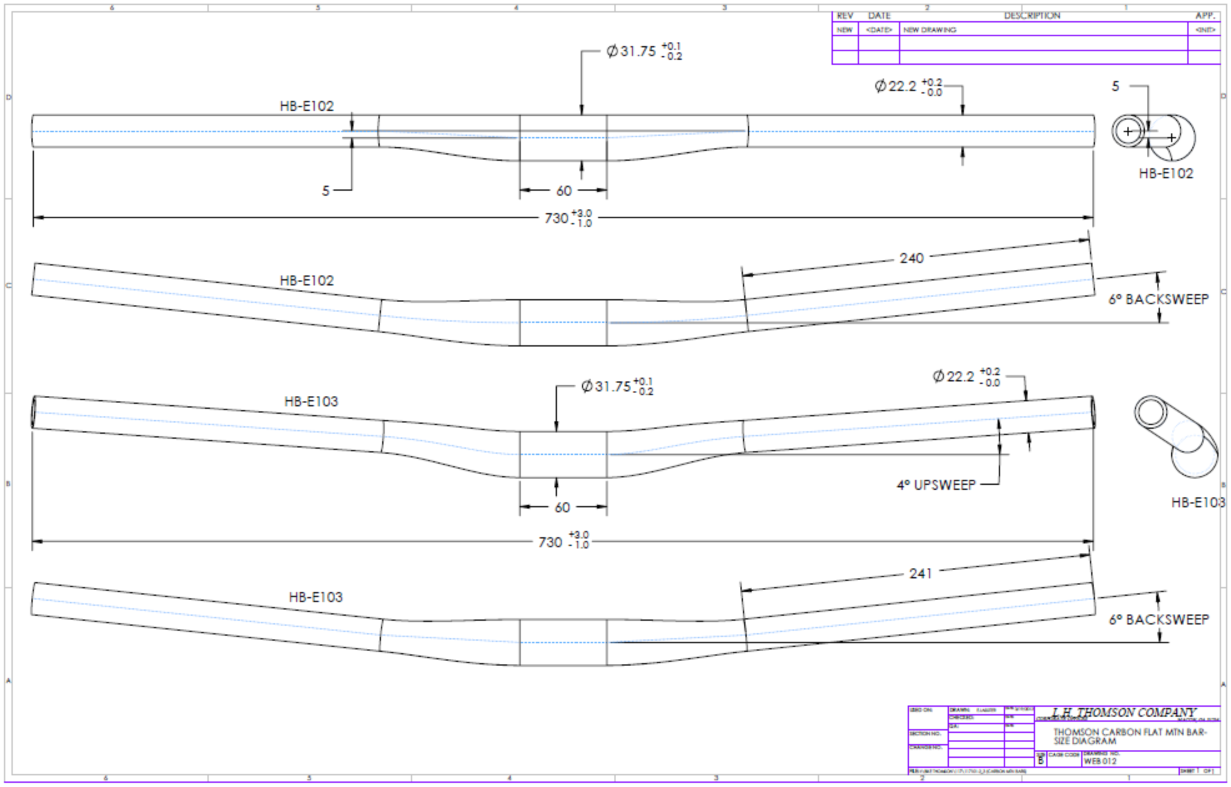

Figure 7 - Benchmark Thomson Mountain Bike Handlebar, HB-102 (44)

The benchmark laminate layup was previously tested by Bonvin, Y. et. al (45). At the thickest region where the stem/handlebar interface is located, the layup is as follows: $[CW/C_5/CW]_T$, where CW denotes plain weave carbon fiber and is oriented at 45^o to the longitudinal axis of the handlebar, and C denotes unidirectional carbon fiber and is oriented at 0^o to the longitudinal axis (along the handlebar). At the thinnest section, past the tapered transition area, the layup is as follows: $[CW/C_2/CW]_{T}$. This design will be used as the benchmark design for all subsequent testing and evaluation of the hybrid laminates.

3 Manufacturing of Composite Components

3.1 Manufacturing of Composite Tubes

To perform the static material characterization tests as well as the initial hybrid composite dynamic property tests, a hollow cylinder with an outer diameter of 22.2mm was used. The outer diameter was determined by the critical section of the handlebar geometry when modeled with the flexural test as described in EN 14766-2006 (6). All materials were tested to determine the ultimate tensile and compressive strength as well as tensile Young's Modulus in the principle directions. The tube manufacturing matrix for material characterization is shown below in Table 2.

Table 2 - Carbon Fiber and Flax Fiber Prepreg Materials

Supplier	Material	Date Received	Date Manufactured	Layup
Newport	Carbon Fiber: Unidirectional NCT301-1, 34-700 G150 Part: 802016m Lot: 79655	21-Mar-2013	22-Aug-2013	$[0]_5$
			26-Aug-2013	$[90]_5$
Newport	Carbon Fiber: Plain Weave Part: NCT321	21-Mar-2013	30-Aug-2013	$[0]_5$
BComp	ampliTex Light UD, non-crimp Part: 5330	25-Oct-2013	30-Oct-2013	$[0]_5$
			02-Nov-2013	$[90]_5$
BComp	ampliTex UD Fabric, light weft, non-crimp Part: 5309	25-Oct-2013	06-Nov-2013	$[0]_4$
			11-Nov-2013	$[90]_2$

All tube samples were manufactured with five layers of laminate, save for the BComp ampliTex unidirectional fabric (5309). This material was received with a maximum width smaller than the cylinder length. Thus, the laminate prepreg geometry was not a simple rectangle as was all other layup configurations, to facilitate laminate joining in the centre of the cylinder length. Due to thickness of the prepreg, only two layers were used for the [90] orientation, to facilitate complete closure of the mold subsequent to layup. The layup procedure is described in the following section. For all cylinders, the longitudinal axis was defined as the [0] direction.

3.1.1 Cylinder Layup Procedure

First, the individual laminate layers were cut with dimensions shown below in Figure 8.

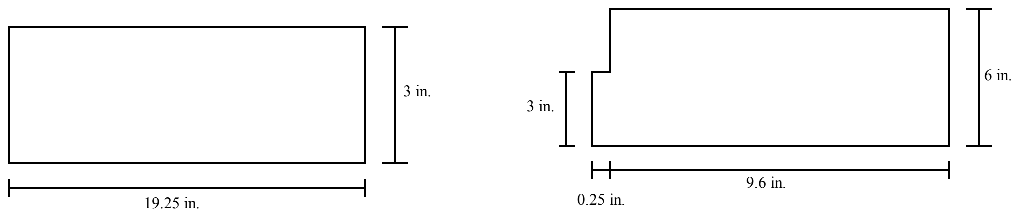

Figure 8 - Laminate Layer Geometry.
Left: Geometry for Carbon Fiber and BComp ampliTex UD Light; *Right:* Layup for BComp ampliTex UD

Each prepreg layer consisted of a single cut-out, as shown above. Subsequent to laminate preparation, a vacuum bag with a diameter of 1in. was placed over an aluminum mandrel. The vacuum bag served as the inner bladder for the cylinder, resulting in a hollow cross section once cured. Each laminate layer was then rolled directly onto the mandrel, aligning the fiber direction as appropriate. For the BComp ampliTex standard (5309) material, the prepreg layers were first oriented with two sections facing each other, and the 0.25in. sections overlapping. This resulted in a rectangular laminate geometry, with a total length of 18.875in. and a height of 6in. One of these rectangular laminates constituted two layers once rolled onto the mandrel, in all sections of the cylinder. Subsequent to layup, the uncured cylinder was placed inside the mold and the mandrel was removed. The end of the vacuum bag was then trimmed to size, and a pressure nozzle valve was sealed. The mold was then closed, and tested for leaks. The tubes were then cured in an oven with a ramp of 1.7^{o}C/min with a hold temperature of 120^{o}C for 2h, and a 1.7^{o}C/min cooling rate, and an internal bladder pressure of 60psi. This cure cycle conforms to both Newport and BComp guidelines. Subsequent to cure, the mold was opened and the pressure nozzle valve removed. This process is illustrated below in Figure 9-Figure 11, with the manufacturing of a plain weave carbon fiber cylinder. Figure 12 depicts a final cylinder specimen, with a unidirectional carbon fiber outer layer.

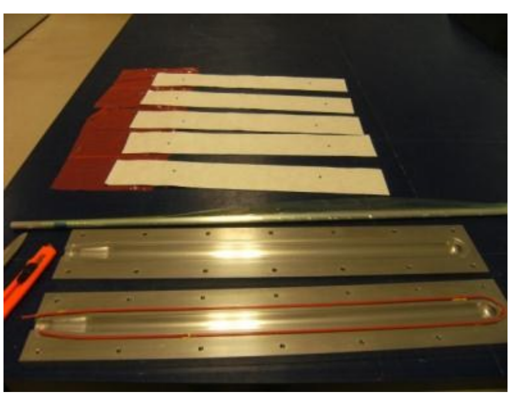

Figure 9 - Preparation of Tube Layup

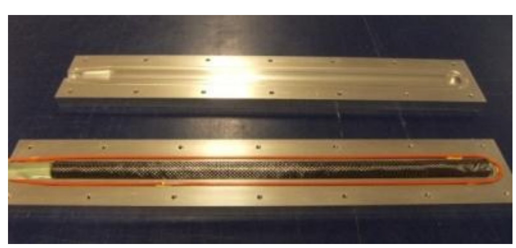

Figure 10 - Uncured Tube in Mould

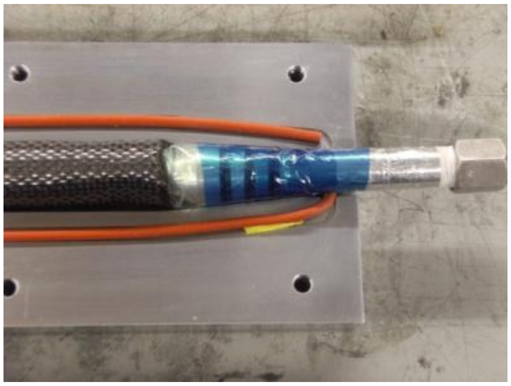

Figure 11 - Pressure Air Nozzle Seal

Figure 12 - Cylinder Specimen

3.2 Manufacturing of Demonstration Bicycle Handlebar

The manufacturing method for the bicycle handlebar was the same as for the hollow cylinders described in Section 3.1. The ply layer thickness and geometry was optimized according to modeling and test results. The layup patterns are shown below in Figure 13.

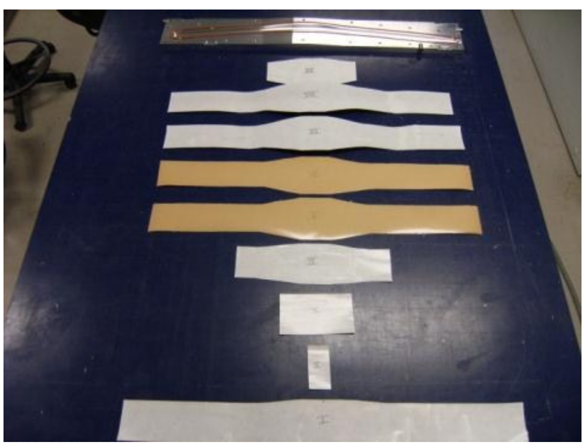

Figure 13 - Handlebar Ply Layers and Geometries
The ply layers are ordered from Ply-1 to Ply-9 starting at the bottom.
Layer material and design were optimized from theoretical and experimental results

Prior to layup, the inner bladder surface was coated with release agent to investigate the possibility of bladder removal post cure. Subsequent to hand-rolling over the straight mandrel, the mandrel was removed and the resulting laminate was gently bent into the handlebar shape and inserted into the mold. The pressure value was then sealed as above, and the part was cured with the same cure cycle and an inner bladder pressure of 60psi.

4 Phase 1: Material Characterization

4.1 Methodology

4.1.1 Manufacturing of Test Samples

For material characterization, tensile testing was first attempted with whole cylinder specimens, as per ASTM D5450-2012 (46). However, the failure location in all instances was at the epoxy/fixture interface and not the test specimen. Therefore, an alternate approach was developed to ensure material failure. The procedures followed were modified versions of ASTM D3039-2008 (47) and ASTM D3410-2003 (48) for tensile and compressive characterization respectfully. Modifications to the standards were required due to the arc geometry of the cylinder specimens.

The cylinders were first cut into four sections, and hand sanded to an approximate arc length of 11mm. Custom tab fixtures were machined with geometry such that the specimen could be mounted into the testing apparatus without specimen damage (Appendix A: Static Strength Test Fixtures) . The tabs were made of mild steel, and had a length of 25mm, width of 11mm, (47) and an inner surface that complied with the specimen arc geometry. The overall length of the tensile test specimens was approximately 190mm, with a gauge length of approximately 140mm, and for compression specimens the overall length was approximately 64mm, with a gauge length of approximately 14mm.

4.1.2 Calculation of Static Strength Properties

4.1.2.1 <u>Cross Sectional Area</u>

To calculate the ultimate tensile and compressive strengths, the cross sectional area of the specimen must first be determined. The cross sectional area is shown in Figure 14 below.

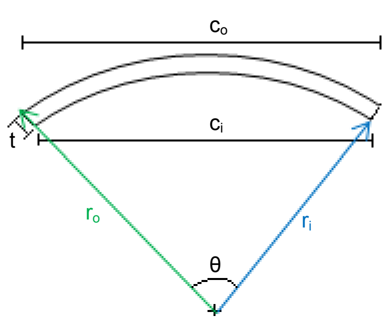

Figure 14 - Sketch of Cross-Section of a Hollow Cylinder

where ‘c’ is the chord length, ‘t’ is the thickness, and ‘θ’ is the arc angle. The subscripts ‘i’ and ‘o’ indicate ‘inner’ and ‘outer’ respectfully. The values t and c_o can be measured directly from the sample preparation. Therefore, the outer arc angle can be calculated from geometry as follows:

$$c_o^2 = 2r_o^2 - 2r_o c_o \cos\theta_o$$

and isolating for the arc angle we obtain:

$$\cos\theta_o = \frac{2r_o^2 - c_o^2}{2r_o c_o} \qquad \textbf{Equation 6}$$

The outer radius (r_o) is fixed for all tubes at 11.1mm. However, as the thickness is material and intra-specimen dependant, the inner radius is also variable. Additionally, the inner chord length, c_i, is dependent upon the thickness and arc angle. A schematic of the relationship between the thickness and arc angle is shown in Figure 15.

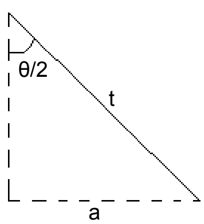

Figure 15 - Relationship between Cylinder Thickness and Arc Angle

where the angle θ/2 represents the angle between the projected end point of the outer chord length (c_o) and inner chord length (c_i) from the vertical axis. From trigonometry, it can be determined that:

$$\sin\left(\frac{\theta}{2}\right) = \frac{a}{t} \text{ where } c_i = c_o - 2a \text{ or}$$

$$c_i = c_o - 2t\sin\left(\frac{\theta_o}{2}\right) \qquad \textbf{Equation 7}$$

Using the relationship derived in Equation 6, the inner arc angle θ_i can be similarly determined:

$$\cos\theta_i = \frac{2r_i^2 - c_i^2}{2r_i c_i} \qquad \textbf{Equation 8}$$

where c_i is calculated as in Equation 7. From these relationships, the cross-sectional area can be derived as follows:

$$A = \left(\frac{\theta_o}{360}\right)\pi r_o^2 - \left(\frac{\theta_i}{360}\right)\pi r_i^2 \qquad \textbf{Equation 9}$$

where θ is expressed in degrees. Due to intra-specimen variability of thickness, all area calculations were performed with the average parameter value.

4.1.2.2 Ultimate Strength

The ultimate strength ($\sigma_{i,j}$) for both tensile (j = T) and compressive (j = C) were calculated as per ASTM D3039-2008 (47) and ASTM D3410-2003 (48) respectfully. The ultimate strength was calculated as follows:

$$\sigma_{ij} = \frac{F}{A} \qquad \textbf{Equation 10}$$

where the subscript 'i' indicates the direction: X = Fiber direction, Y = Matrix direction, and 'j' indicates Tensile (T) or Compressive (C). The force, F, was the ultimate recorded force at failure.

4.1.2.3 Tensile Young's Modulus

The tensile Young's Modulus, E_T, was calculated as per ASTM D3039-2008 (47), and is shown below in Equation 11.

$$E_T = \frac{\Delta\sigma_{iT}}{\Delta\varepsilon} \qquad \textbf{Equation 11}$$

As per the ASTM guidelines, for the fiber tensile Young's Modulus Δε was taken between the recorded strain values which best represented the initial elastic stress behaviour of the sample.

As the purpose of these tests was for material characterization for subsequent use in FEA models, for simplicity it was assumed that the compressive Young's Modulus was equivalent to the tensile Young's Modulus. Thus, the compressive Young's Modulus was not experimentally measured.

4.1.3 Test Procedure: Tensile Strength

The procedure followed was adapted from ASTM D3039-2008 (47). First, the specimens were machined to size, as per the geometry requirements in Section 4.1.1. Specimen mass, length, chord length, and thickness were recorded. The specimen was then potted in the custom test fixtures (Appendix A: Static Strength Test Fixtures) with Loctite 9340 Hysol Epoxy, and cured under pressure applied with a caul plate at room temperature for 72 hours. Figure 16 below illustrates a prepared tensile specimen.

Figure 16 - Sample of a Prepared Tensile Specimen

The prepared specimens were then mounted in the MTS 100kN Load Cell (Model: 661.21A-03, Serial: 3950), with a fixture grip pressure of 1000psi. Strain was measured with an extensometer (MTS Extensometer, Model: 632.31E-24, Serial: 162) mounted in the centre of the specimen. Figure 17 below illustrates a sample set-up.

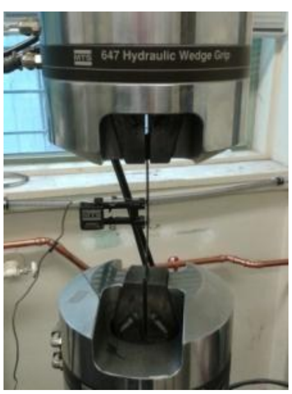

Figure 17 - Tensile Test

As per the ASTM guidelines, five samples (n=5) were tested at a displacement rate of 1.5mm/min, which resulted in failure within the required 1-10 minutes of loading. For each test force, displacement, and strain were measured until ultimate failure. Subsequent to failure, the failure mode and location was recorded. The ultimate tensile stress ($\sigma_{XT/YT}$) and tensile Young's Modulus (E_T) were then calculated.

4.1.4 Test Procedure: Compression Strength

For the compression strength, the specimens were prepared in the same manner as the tensile specimens above, as shown in Figure 19 below.

Figure 18 - Compressive Test Setup

Figure 19 - Sample of a Prepared Compressive Specimen

The test specimens were mounted in the MTS apparatus in the same manner (Figure 18). The procedure followed was slightly adapted from ASTM D3410-2003 (48). As per the ASTM guidelines, five samples (n=5) were tested at a rate of 1.3mm/min, which resulted in failure within the required 1-10 minutes of loading. For each test, force and displacement were measured until ultimate failure. Subsequent to failure, the failure mode and location was recorded. The ultimate compression stress ($\sigma_{XC/YC}$) was then calculated.

4.2 Results

4.2.1 Tensile Results

For all specimens, the average cross-sectional area (A), density (ρ), ultimate tensile stress ($\sigma_{XT/YT}$) and tensile Young's Modulus (E_T) were calculated based on the average specimen measured thickness (t) and chord length (c_o). The average material density, cross-sectional area, ultimate tensile stress, and tensile Young's Modulus for the material were then calculated, excluding identified outliers (Figure 20- Figure 22 and Figure 25- Figure 28).

4.2.1.1 Carbon Fiber

The intra-specimen variability in cross-sectional area for the Newport unidirectional (301) and plain weave (321) carbon fiber is shown below in Table 3.

Table 3 - Intra Specimen Cross Sectional Area Variability for Carbon Fiber Tensile Specimens

Specimen	Average Cross Sectional Area [m^2]	Standard Deviation	
Unidirectional			
Cu02_1.1	1.21E-05	6.15E-06	50.8%
Cu02_1.2	9.60E-06	3.04E-06	31.7%
Cu02_1.3	1.22E-05	2.20E-06	18.1%
Cu02_1.4	**7.44E-06**	**4.11E-06**	**55.2%**
Cu02_2.1	8.84E-06	2.72E-06	30.8%
Cu03_2.1	1.03E-05	3.20E-06	31.1%
Cu03_2.2	7.96E-06	4.33E-06	54.4%
Cu04_1.1	**8.39E-06**	**6.90E-06**	**82.2%**
Cu04_1.2	9.45E-06	2.58E-06	27.3%
Cu04_1.3	8.28E-06	1.50E-06	18.1%
Plain Weave			
Cw01_1.1	1.26E-05	1.94E-06	15.4%
Cw01_1.2	1.38E-05	1.90E-06	13.8%
Cw01_1.3	1.31E-05	1.65E-06	12.6%
Cw01_1.4	1.53E-05	2.76E-06	18.1%
Cw01_2.1	1.36E-05	3.59E-06	26.4%

*The specimens in bold represent outliers in testing results, and were omitted from the characterized material behaviour calculations in Table 4.

The average tensile stress-strain data curves for the materials are shown below in Figure 20-Figure 22.

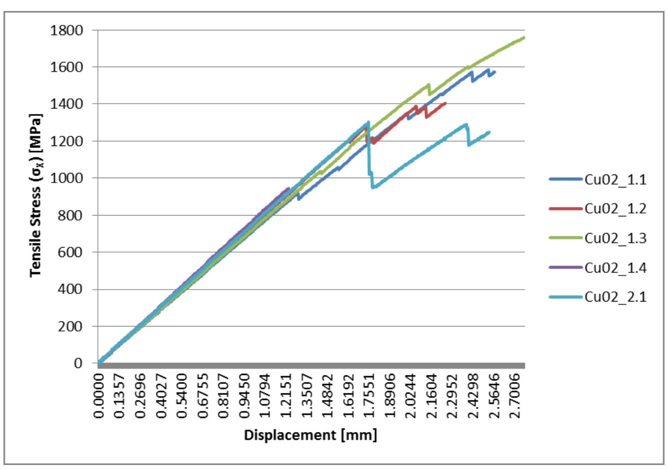

Figure 20 - Average Fiber Tensile Stress (σ_{XT}) for Unidirectional Carbon Fiber

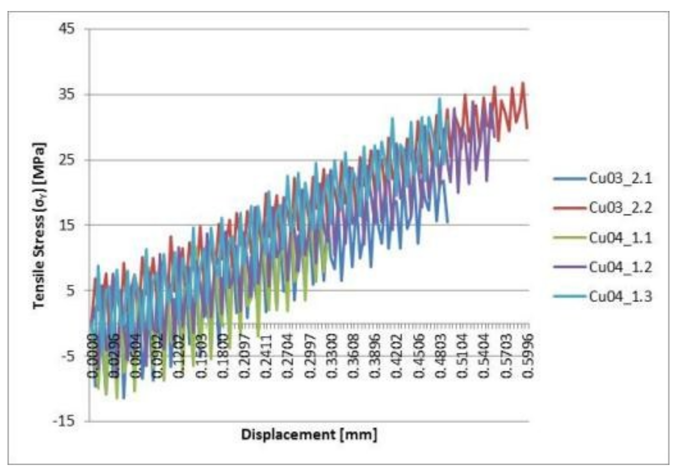

Figure 21 - Average Matrix Tensile Stress (σ_{YT}) for Unidirectional Carbon Fiber

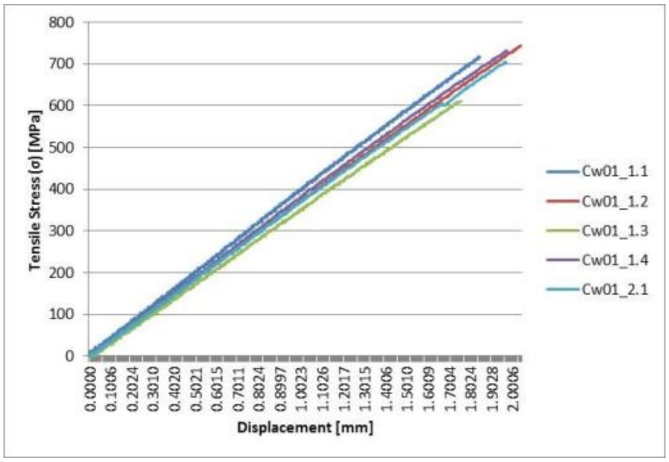

Figure 22 - Average Tensile Stress ($\sigma_{XT/YT}$) for Plain Weave Carbon Fiber

The characterized material behaviour for the unidirectional and plain weave carbon fiber materials is shown below in Table 4, taking into consideration outliers identified in Figure 20-Figure 22.

Table 4 - Newport Unidirectional and Plain Weave Carbon Fiber Tensile Properties

	Unidirectional			Plain Weave		
Property	**Average**	**Standard Deviation**		**Average**	**Standard Deviation**	
Sample Size	4			5		
Density (ρ) [g/cm^3]	1.55	0.52	33.6%	1.52	0.07	4.4%
Cross-Sectional Area (A) [m^2]	9.84E-06	1.60E-06	16.3%	1.37E-05	1.03E-06	7.5%
Ultimate Tensile Strength (σ_{XT}) [MPa]	1,496.29	220.09	14.7%	701.88	52.83	7.5%
Ultimate Tensile Strength (σ_{YT}) [MPa]	32.46	5.13	15.8%			
Young's Modulus (E_{XT}) [MPa]	112,649.17	602.13	0.5%	56,999.31	2,001.32	3.5%
Young's Modulus (E_{YT}) [MPa]	8,921.21	1,604.48	18.0%			

In general, the samples failed in a consistent manner. Figure 23 and Figure 24 below illustrate typical failures observed in the specimens during testing.

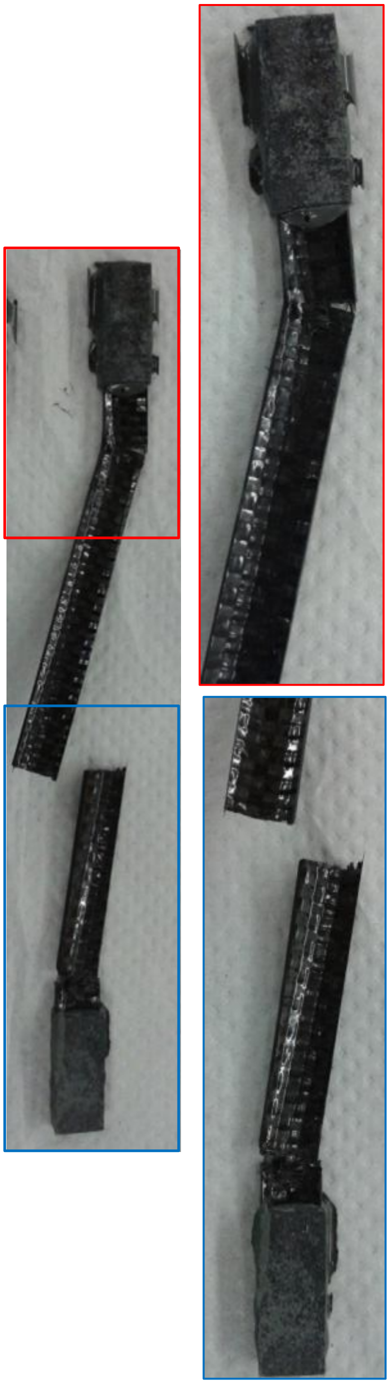

Figure 23 - Typical Failure Mode of Plain Weave Carbon Fiber
Right: Failed Specimen
Left Top: Detailed view of failure location at top of specimen
Left Bottom: Detailed view of failure location at bottom of specimen

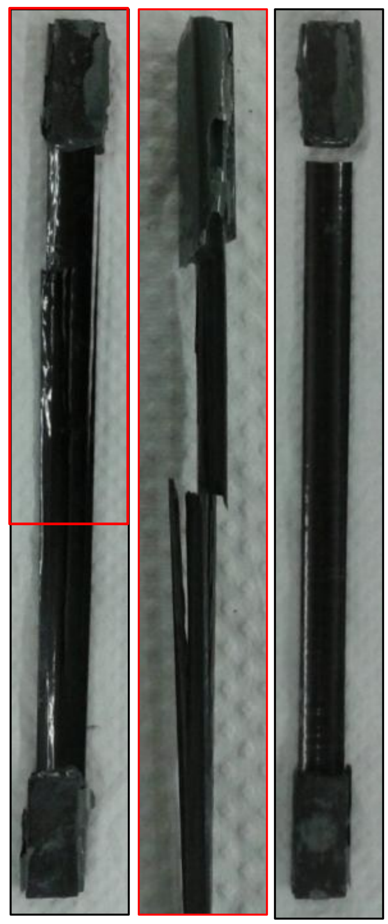

Figure 24 - Typical Failure Mode of Unidirectional Carbon Fiber
Right: Unidirectional Carbon Fiber specimen oriented in the fiber [0] direction.
Centre: Detailed view of failure location of fiber failure
Left: Unidirectional Carbon Fiber Specimen oriented in the matrix [90] direction

4.2.1.2 Flax Fiber

The intra-specimen variability in cross-sectional area of the tensile specimens for the BComp ampliTex light unidirectional (5330) and ampliTex standard unidirectional (5309) flax fiber prepregs is shown below in Table 5.

Table 5 - Intra Specimen Cross Sectional Area Variability for BComp ampliTex Light and Standard Unidirectional Flax Fiber Tensile Specimens

Specimen	Average Cross Sectional Area [m^2]	Standard Deviation	
ampliTex Light Unidirectional (5330)			
FL01_1.1	1.39E-05	2.77E-06	19.9%
FL01_1.2	**1.56E-05**	**3.87E-06**	**24.9%**
FL01_1.3	1.57E-05	4.16E-06	26.4%
FL01_1.4	1.22E-05	4.60E-06	37.5%
FL01_2.1	1.36E-05	2.25E-06	16.5%
FL02_1.1	2.23E-05	5.78E-06	25.9%
FL02_1.2	1.52E-05	5.01E-06	32.9%
FL02_1.3	1.29E-05	8.11E-06	62.8%
FL02_2.1	**1.82E-05**	**7.40E-06**	**40.7%**
FL02_2.2	1.91E-05	5.36E-06	28.1%
ampliTex Standard Unidirectional (5309)			
Fu01_1.1	1.74E-05	2.21E-06	12.7%
Fu01_1.2	2.09E-05	4.30E-06	20.5%
Fu01_1.3	2.23E-05	4.57E-06	20.5%
Fu01_1.4	2.18E-05	3.24E-06	14.8%
Fu01_3.1	2.23E-05	4.10E-06	18.4%
Fu02_1.1	1.13E-05	3.70E-06	32.8%
Fu02_1.2	9.31435E-06	2.37045E-06	12.7%
Fu02_1.3	1.08843E-05	4.82037E-06	20.5%
Fu02_1.4	1.34877E-05	5.67551E-06	20.5%
Fu02_3.1	1.34877E-05	5.67551E-06	14.8%

*The specimens in bold represent outliers in testing results, and were omitted from the characterized material behaviour calculations in Table 6.

The average tensile stress-strain data curves for the materials are shown below in Figure 25-Figure 28.

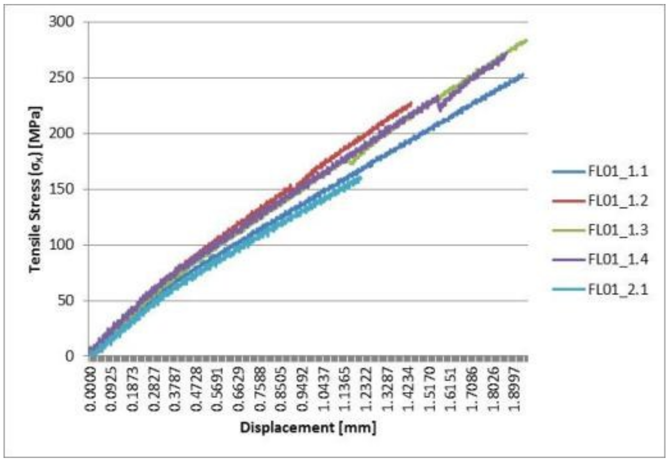

Figure 25 - Average Fiber Tensile Stress (σ_{XT}) for ampliTex Light Unidirectional Flax Fiber (5330)

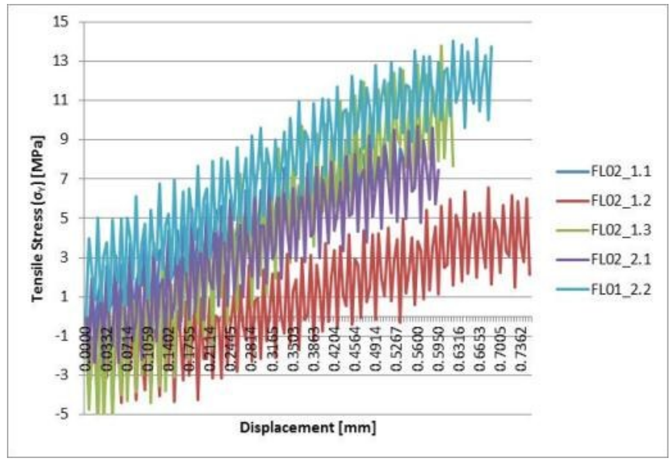

Figure 26 - Average Matrix Tensile Stress (σ_{YT}) for ampliTex Light Unidirectional Flax Fiber (5330)

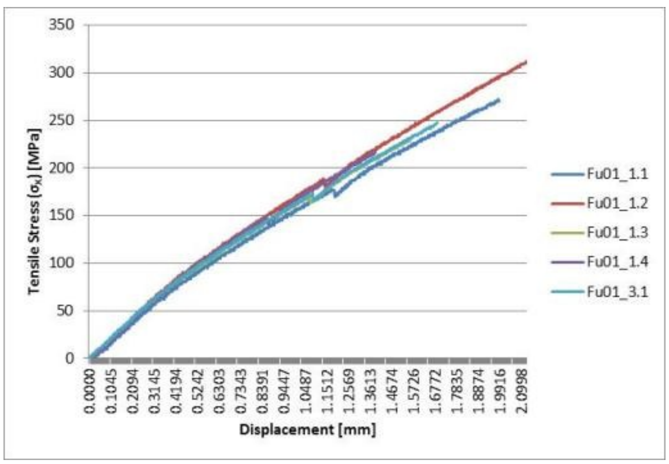

Figure 27 - Average Fiber Tensile Stress (σ_{XT}) for ampliTex Standard Unidirectional Flax Fiber (5309)

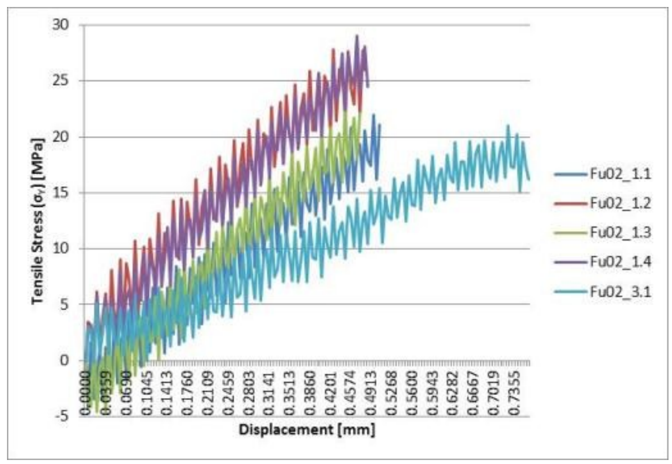

Figure 28 - Average Matrix Tensile Stress (σ_{YT}) for ampliTex Standard Unidirectional Flax Fiber (5309)

The characterized behaviour for the BComp ampliTex light unidirectional (5330) and ampliTex standard unidirectional (5309) prepregs are shown below in Table 6 taking into consideration outliers identified in Figure 25- Figure 28.

Table 6 - BComp ampliTex Light and Standard Unidirectional Flax Fiber Tensile Properties

	ampliTex Light Unidirectional (5330)			ampliTex Standard Unidirectional (5309)		
Property	**Average**	**Standard Deviation**		**Average**	**Standard Deviation**	
Sample Size	4			4		
Density (ρ) [g/cm^3]	1.11	0.12	11.2%	1.33	0.10	7.7%
Cross-Sectional Area (A) [m^2]	1.63E-05	3.43E-06	21.1%	1.60E-05	5.42E-06	33.9%
Ultimate Tensile Strength (σ_{XT}) [MPa]	259.58	24.80	9.6%	265.38	35.19	13.3%
Ultimate Tensile Strength (σ_{YT}) [MPa]	11.66	2.53	21.7%	25.54	3.73	14.6%
Young's Modulus (E_{XT}) [MPa]	29,305.81	1,221.58	4.2%	26,903.80	4,074.58	15.2%
Young's Modulus (E_{YT}) [MPa]	1,683.96	513.65	30.5%	3,020.35	147.41	4.9%

In general, the samples failed in a consistent manner. Figure 29 and Figure 30 below illustrate typical failures observed in the specimens during testing.

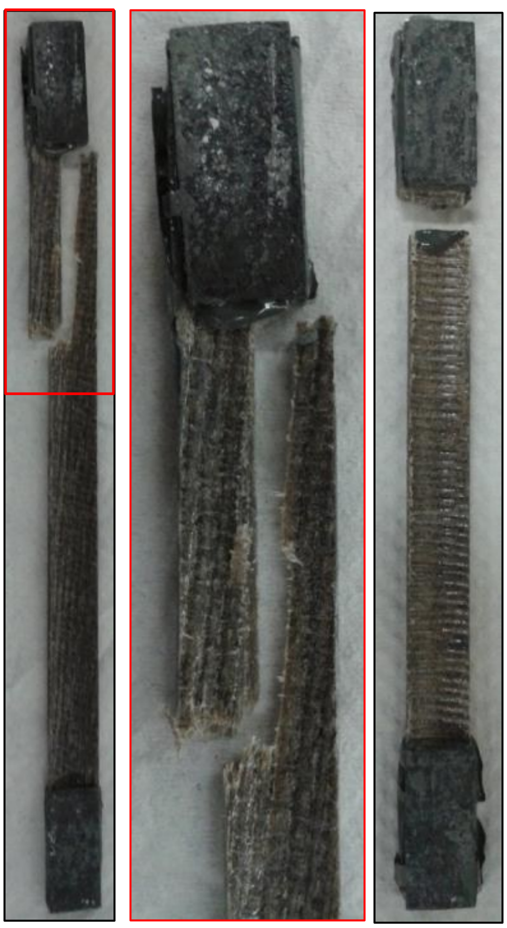

Figure 29 - Typical Failure Mode of ampliTex Light Unidirectional Flax Fiber
Right: Unidirectional Flax Fiber specimen oriented in the fiber [0] direction.
Centre: Detailed view of failure location of fiber failure

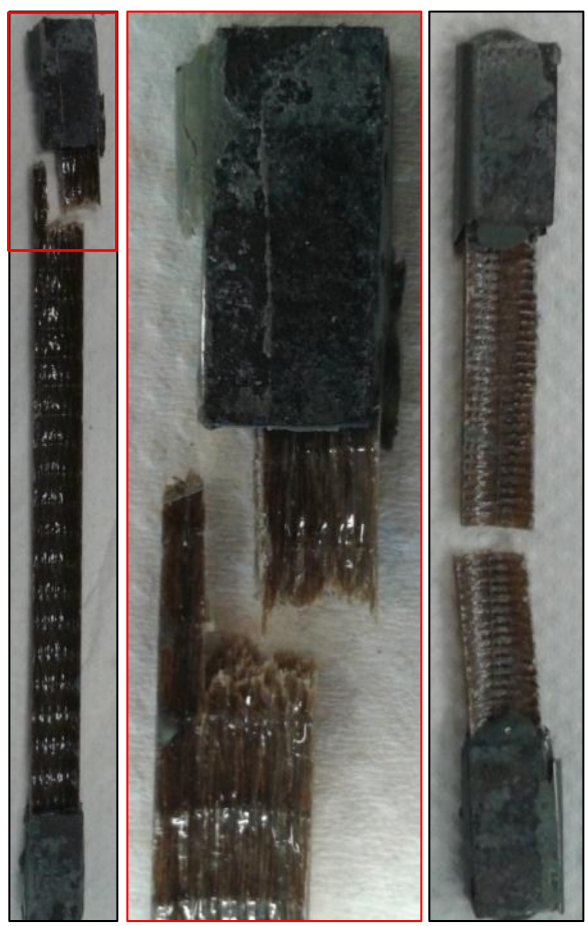

Figure 30 - Typical Failure Mode of ampliTex Standard Unidirectional Flax Fiber
Right: Unidirectional Flax Fiber specimen oriented in the fiber [0] direction.

4.2.2 Compression Results

Similar to the tensile specimens, the average cross-sectional area (A), density (ρ), and ultimate compressive stress ($\sigma_{XC/YC}$) were calculated based on the average measured specimen thickness (t) and chord length (c_o). The average material density, cross-sectional area, and ultimate compressive stress were calculated, excluding identified outliers (Figure 31 - Figure 33, and Figure 37 - Figure 40).

4.2.2.1 Carbon Fiber

The intra-specimen variability in cross-sectional area for the Newport unidirectional (301) and plain weave (321) carbon fiber compression specimens is shown below in Table 7.

Table 7 - Intra Specimen Cross Sectional Area Variability for Carbon Fiber Compression Specimens

Specimen	Average Cross Sectional Area [m^2]	Standard Deviation	
	Unidirectional		
Cu02_2.2.1	**9.90E-06**	**3.20E-06**	**32.4%**
Cu02_2.2.2	**8.75E-06**	**4.65E-06**	**53.1%**
Cu02_2.3.1	1.21E-05	3.03E-06	25.1%
Cu02_2.3.2	1.09E-05	2.45E-06	22.6%
Cu02_2.4.1	1.28E-05	2.37E-06	18.5%
Cu03_2.2.1	8.78E-06	2.36E-06	26.9%
Cu03_2.2.2	1.08E-05	1.92E-06	17.8%
Cu03_2.3.1	9.11E-06	2.97E-06	32.6%
Cu03_2.3.2	**9.63E-06**	**2.40E-06**	**25.0%**
Cu03_2.4.1	**8.99E-06**	**3.20E-06**	**35.6%**
	Plain Weave		
Cw01_2.2.1	1.34E-05	4.21E-06	31.4%
Cw01_2.2.2	1.30E-05	2.20E-06	16.9%
Cw01_2.3.1	1.46E-05	2.26E-06	15.5%
Cw01_2.3.2	1.40E-05	1.50E-06	10.7%
Cw01_2.4.1	1.45E-05	1.86E-06	12.8%

*The specimens in bold represent outliers in testing results, and were omitted from the characterized material behaviour calculations in Table 8.

The average compressive stress-strain data curves for the materials are shown below in Figure 31 - Figure 33.

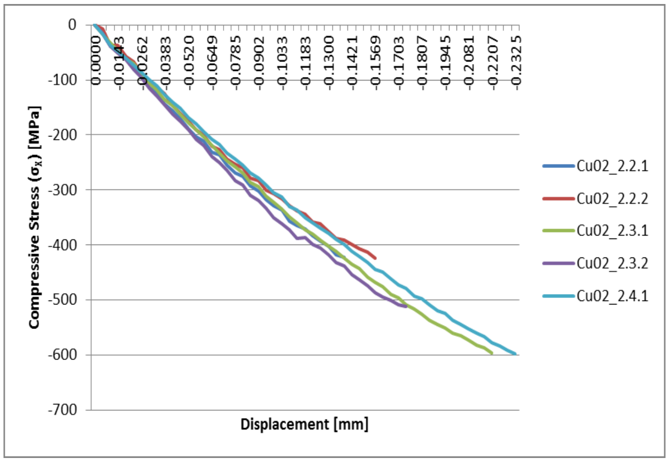

Figure 31 - Average Fiber Compressive Stress (σ_{XC}) for Unidirectional Carbon Fiber

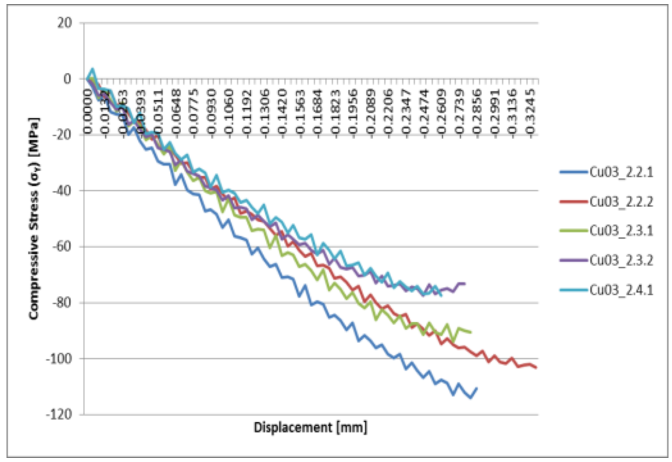

Figure 32 - Average Matrix Compressive Stress (σ_{YC}) for Unidirectional Carbon Fiber

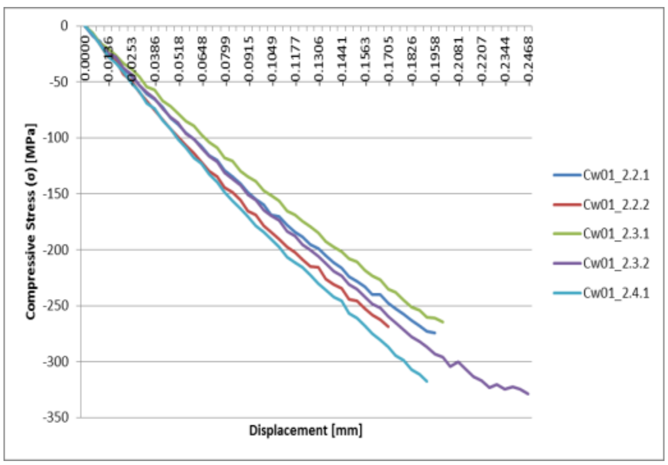

Figure 33 - Average Compressive Stress ($\sigma_{XC/YC}$) for Plain Weave Carbon Fiber

The characterized material behaviour for the unidirectional and plain weave carbon fiber materials is shown below in Table 8, taking into consideration outliers identified in Figure 31 - Figure 33.

Table 8 - Newport Unidirectional and Plain Weave Carbon Fiber Compressive Properties

	Unidirectional			**Plain Weave**		
Property	**Average**	**Standard Deviation**		**Average**	**Standard Deviation**	
Sample Size	3			5		
Density (ρ) [g/cm^3]	1.56	0.07	4.7%	1.51	0.04	2.6%
Cross-Sectional Area (A) [m^2]	1.07E-05	1.59E-06	14.8%	1.39E-05	6.89E-07	5.0%
Ultimate Compressive Strength (σ_{XC}) [MPa]	568.52	49.55	8.7%	290.88	29.83	10.3%
Ultimate Compressive Strength (σ_{YC}) [MPa]	103.68	9.97	9.6%			

In general, the samples failed in a consistent manner. Figure 34 and Figure 35 illustrate typical compression failure of the unidirectional carbon fiber, and Figure 36 illustrates typical plain weave carbon fiber failure. As is shown in Figure 36, the surface failure location was difficult to observe. Failure was best observed looking at the through thickness failure.

Figure 34 - Typical Failure of Unidirectional [90] Carbon Fiber
Left: Mounted Specimen at failure
Right: Detailed view of specimen at location of failure

Figure 35 - Typical Failure of Unidirectional [0] Carbon Fiber
Arrows indicate location of edge crack propagation

Figure 36 - Typical Failure of Plain Weave Carbon Fiber
Left: Inner surface of failed specimen. Red box indicates location of failure
Right: Detailed side view of failure location

4.2.2.2 Flax Fiber

The intra-specimen variability in cross-sectional area of the compression specimens for the BComp ampliTex light unidirectional (5330) and ampliTex standard unidirectional (5309) Flax fiber prepregs is shown below in Table 9.

Table 9 - Intra Specimen Cross Sectional Area Variability for BComp ampliTex Light and Standard Unidirectional Flax Fiber Compression Specimens

Specimen	Average Cross Sectional Area [m^2]	Standard Deviation	
ampliTex Light Unidirectional (5330)			
FL01_2.2.1	1.48E-05	3.61E-06	24.4%
FL01_2.2.2	1.30E-05	4.82E-06	37.2%
FL01_2.3.1	1.84E-05	2.54E-06	13.8%
FL01_2.3.2	1.39E-05	3.07E-06	22.0%
FL01_2.4.1	1.36E-05	2.64E-06	19.4%
FL02_1.4.1	**1.96E-05**	**4.70E-06**	**24.0%**
FL02_1.4.2	2.15E-05	3.39E-06	15.8%
FL02_2.3.1	1.64E-05	3.82E-06	23.3%
FL02_2.3.2	2.03E-05	2.69E-06	13.3%
FL02_2.4.1	1.84E-05	5.07E-06	27.6%
ampliTex Standard Unidirectional (5309)			
Fu01_3.2.1	**1.75E-05**	**2.35E-06**	**13.5%**
Fu01_3.2.2	1.87E-05	1.71E-06	9.2%
Fu01_3.3.1	1.96E-05	2.42E-06	12.3%
Fu01_3.3.2	1.80E-05	1.63E-06	9.1%
Fu01_3.4.1	1.56E-05	1.69E-06	10.9%
Fu02_1.1.2	9.78E-06	2.12E-06	21.7%
Fu02_1.2.2	7.66E-06	2.33E-06	30.5%
Fu02_1.3.2	1.00E-05	4.02E-06	40.2%
Fu02_1.4.2	7.52E-06	1.97E-06	26.2%
Fu02_3.1.2	**1.00E-05**	**2.42E-06**	**24.2%**

*The specimens in bold represent outliers in testing results, and were omitted from the characterized material behaviour calculations in Table 10.

The average compressive stress-strain data curves for the materials are shown below in Figure 37 - Figure 40.

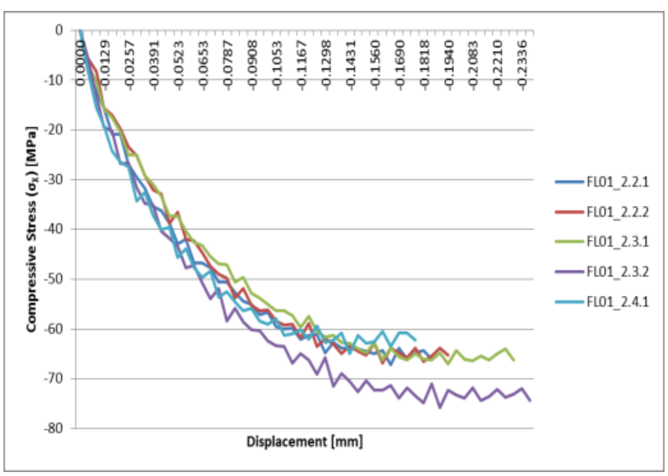

Figure 37 - Average Fiber Compressive Stress (σ_{XC}) for ampliTex Light Unidirectional Flax Fiber (5330)

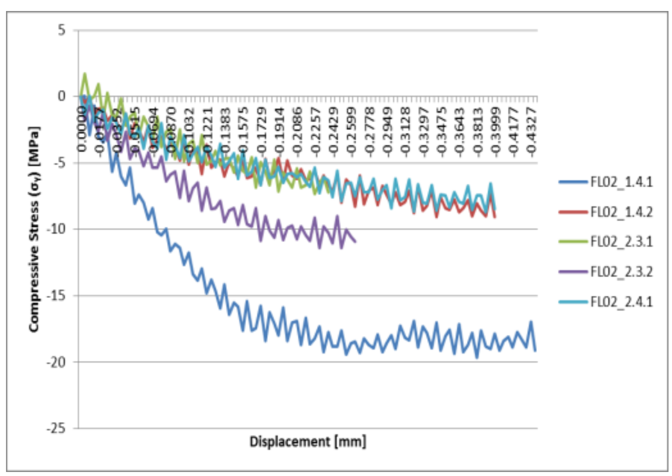

Figure 38 - Average Matrix Compressive Stress (σ_{YC}) for ampliTex Light Unidirectional Flax Fiber (5330)

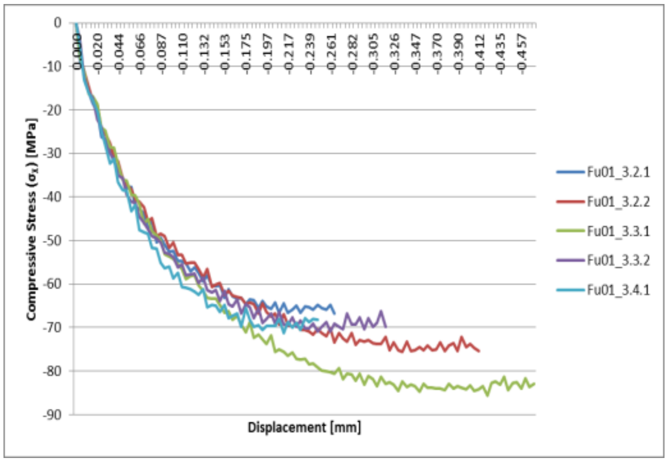

Figure 39 - Average Fiber Compressive Stress (σ_{XC}) for ampliTex Standard Unidirectional Flax Fiber (5309)

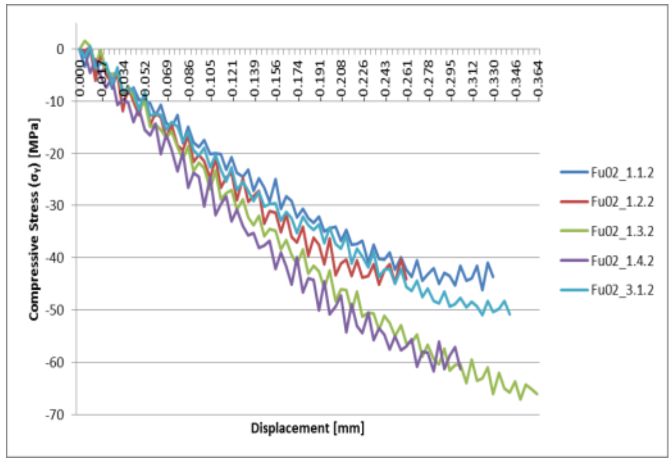

Figure 40 - Average Matrix Compressive Stress (σ_{YC}) for ampliTex Standard Unidirectional Flax Fiber (5309)

The characterized compressive behaviour for the BComp ampliTex light unidirectional (5330) and ampliTex standard unidirectional (5309) is shown below in Table 10, taking into consideration the outliers identified in Figure 37 - Figure 40.

Table 10 - BComp ampliTex Light and Standard Unidirectional Flax Fiber Compressive Properties

	ampliTex Light Unidirectional (5330)			ampliTex Standard Unidirectional (5309)		
Property	**Average**	**Standard Deviation**		**Average**	**Standard Deviation**	
Sample Size	5 (σ_{XC}), 4 (σ_{YC})			4		
Density (ρ) [g/cm^3]	1.11	0.15	13.6%	1.42	0.14	9.9%
Cross-Sectional Area (A) [m^2]	1.67E-05	3.09E-06	18.5%	1.34E-05	5.13E-06	38.4%
Ultimate Compressive Strength (σ_{XC}) [MPa]	68.36	4.25	6.2%	75.84	6.85	9.0%
Ultimate Compressive Strength (σ_{YC}) [MPa]	9.11	1.69	18.6%	51.03	7.63	15.0%

In general, the samples failed in a consistent manner. Figure 41 and Figure 42 below illustrate typical failures observed in the ampliTex light unidirectional (5330) flax material, and Figure 43 and Figure 44 illustrate typical failures observed in the ampliTex standard unidirectional (5309) flax material during testing.

Figure 41 - Failure Mode of [0] ampliTex Light Unidirectional Flax Fiber
Left: Inner surface of failed specimen
Right: Detailed side view of failure location

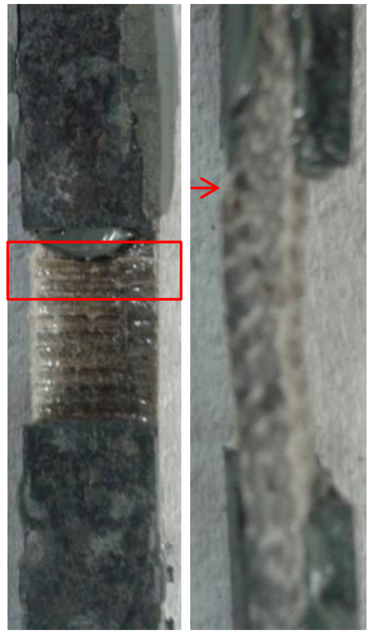

Figure 42 - Failure Mode of [90] ampliTex Light Unidirectional Flax Fiber
Left: Inner surface of failed specimen. Red box indicates location of failure.
Right: Detailed side view of failure location. Red arrow indicates position of failure on

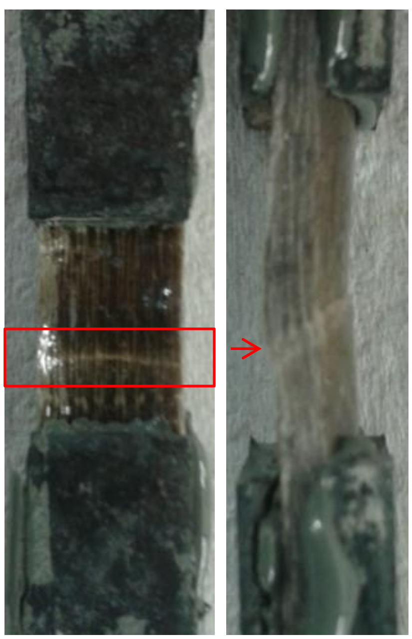

Figure 43 - Failure Mode of [0] ampliTex Standard Unidirectional Flax Fiber
Left: Inner surface of failed specimen. Red box indicates location of failure.

Figure 44 - Failure Mode of [90] ampliTex Standard Unidirectional Flax Fiber
Inner surface of failed specimen. Red box indicates location of failure.

4.3 Discussion

4.3.1 Tensile Results

4.3.1.1 Carbon Fiber Behaviour

From Table 3, the intra-specimen variability of the cross-sectional area due to variability in thickness (t) and chord length (c_o) was significant. For the unidirectional material, this variability ranged from 18% to 54% and for the plain weave 14% - 26% of the average cross-section area. As the cross-sectional area is required for the subsequent stress (Equation 10) and Young's Modulus (Equation 11) calculations, this difference will be propagated to the final material property characterization results. Due to this high variability, it was decided that for modeling purposes the average cross-sectional area of the specimens would be used, and thus the overall averaged ultimate tensile strength and Young's modulus were inputs in the succeeding analysis.

From Table 4, the standard deviation for the calculated fiber tensile properties are 15% for the ultimate tensile strength and 0.53% for the Young's Modulus for the unidirectional carbon fiber, and 7.5% and 3.5% for the plain weave carbon fiber, respectfully. For the matrix direction, the standard deviation ranges from 16-18% for the unidirectional carbon fiber samples. Also from Table 4, the standard deviation of the calculated cross sectional area is 16% for the unidirectional carbon fiber and 7.5% for the plain weave carbon fiber, which would propagate into the strength and Young's Modulus calculations as previously discussed. During testing it was observed that all samples failed with similar failure mechanisms, indicating that the failure modes were consistent for all samples. When compared to the properties obtained for unidirectional carbon fiber as obtained by Duc. et. al. (Table 1), the results obtained are marginally superior with those found in literature. This difference is most likely due to the different manufacturing methods by Duc. et. al. and this study. Therefore, the tensile strength properties obtained through testing are within the expected errors, and can be considered representative of the material behaviour when manufactured with the hollow cylinder method.

4.3.1.2 Flax Fiber Behaviour

From Table 5, the intra-specimen variability of the cross-sectional area due to the variability in the thickness (t) and chord length (c_o) was significant. For the ampliTex light unidirectional

(5330) material, the cross-sectional area variability ranged from 16% to 63% and for the standard unidirectional material (5309) 13% to 44% when compared to the average. These values are similar to the variability in the unidirectional carbon fiber materials, as discussed above. Thus, for modeling purposes the average ultimate tensile strength and Young's modulus will be used for all succeeding analysis.

From Table 6, the standard deviation for the calculated fiber tensile properties are 10-13% for the ultimate tensile strength and 4-15% for the Young's Modulus respectfully. For the matrix direction, the standard deviation ranges from 15-22% for the tensile strength and 5-30% for the Young's Modulus. Also from Table 6, the standard deviation of the calculated cross sectional area was 21% for the light unidirectional (5330) and 34% for the standard unidirectional (5309), which affects the strength and Young's Modulus calculations as previously discussed. During testing it was observed that all samples failed with similar failure mechanisms, indicating that the failure modes were consistent for all samples. When compared to literature values (Table 1), the results obtained here are in close agreement with the experimental ultimate tensile strengths found by Duc et. al. (13), and the Young's Moduli are in close agreement with Phillips et. al. (2011) (20). This difference is most likely due to the different manufacturing methods between the three studies. Therefore, the tensile strength properties obtained through testing are within the expected errors, and can be considered representative of the material behaviour when manufactured with the hollow cylinder method.

4.3.2 Compression Results

Similar to the tensile specimens, there was significant variability in the thickness of the specimen and associated variability in the cross-sectional area, as shown in Table 7 and Table 9. This may have a greater impact on the ultimate compression strength, due to the inherent difficulties in the test procedure. Failure due to pure compression can be difficult to achieve experimentally, as structures that are loaded in compression may be subject to buckling in the unsupported regions prior to failure due to compression. This possibility is limited by minimizing the gauge length: as per ASTM D3410-03 (48) standard, the minimum gauge length is 10-25mm. All tested specimens had a gauge length ranging from 11.2mm-16.7mm, well within the ASTM D3410-03 (48) guidelines.

4.3.2.1 Carbon Fiber Behaviour

From Table 7, the intra-specimen variability of the cross-sectional area due to variability in thickness (t) and chord length (c_o) was significant. For the unidirectional material, this variability ranged from 17% to 32% and for the plain weave 11% to 31% of the average cross-section area, when taking into consideration the outliers. Similar to the tensile stress calculation, this difference will be propagated to the final material property characterization results. Due to this high variability, it was decided that for modeling purposes the average cross-sectional area of the specimens would be used, and thus the overall averaged ultimate compression strength were inputs in the succeeding analysis.

From Table 8, it is shown that the standard deviations for the compressive strength properties were very consistent, ranging from 9-10% for both materials and directions. Also from Table 8, the standard deviation for the average cross-sectional area was 5% for the plain weave and 15% for the unidirectional carbon fiber. This calculation error would have propagated to the ultimate compressive strength calculation as previously discussed. An additional source of error in compression testing is the inherent difficulty in experimental validation, as it is difficult to ensure pure failure in compression and not pre-failure due to buckling. Although all samples failed in a consistent manner, as is illustrated in Figure 35 and Figure 36, it is most likely that the failure was due to buckling as well as compression. The difficulty of compression testing is likely the reason for the minimal available literature on the expected compression strengths of a carbon fiber prepreg. Therefore, although mixed-mode failure was suspected, due to the consistent results and taking into consideration the propagated error associated with the cross-sectional area calculation, these results are within the expected range of error, and consistent with those of the tensile testing. Thus, the methodology followed to test the compression properties can be considered valid and representative of the approximate compression behaviour of the carbon fiber materials when manufactured and processed as in the cylinder manufacturing process.

4.3.2.2 Flax Fiber Behaviour

From Table 9, the intra-specimen variability of the cross-sectional area due to the variability in the thickness (t) and chord length (c_o) was significant. For the ampliTex light unidirectional

(5330) material, the cross-sectional area variability ranged from 13% to 37% and for the standard unidirectional material (5309) 9% to 40% when compared to the average. Unlike the carbon fiber compression specimens, these ranges are inclusive of the identified outliers. However, these absolute ranges are similar to the variability in the Newport unidirectional carbon fiber materials, as discussed above. Thus, for modeling purposes the average ultimate compression strength as calculated from the average cross-sectional area will be used for all succeeding analysis.

From Table 10, the variation in the average ultimate compressive strength for the fiber direction was 6% and 9% for the light (5330) and standard (5309) material respectfully. For the matrix direction, the variation from the average was approximately 19% and 15% for the light (5330) and standard (5309) respectfully. For both materials this is below the propagated cross-sectional area variability of 10% for the standard (5309) and 14% for the light (5330) material. When comparing this variability to the intra-specimen variability found for the tensile testing in Table 6, the compression testing resulted in lower intra-specimen variability in ultimate compression strength in the fiber direction, and approximately equivalent intra-specimen variability in the matrix direction. Therefore, as with the carbon fiber compression testing, the flax fiber ultimate compression results are consistent with the flax fiber tensile results, when taking into consideration the effect of manufacturing processes, material variability due to moisture content, and potential errors associated with misalignment of the laminate layers.

The flax fiber intra-specimen variability is approximately equivalent to that of the carbon fiber ultimate compression strength variability in the fiber direction, and marginally greater than that of the carbon fiber in the matrix direction. As with the carbon fiber compression testing, from Figure 41 and Figure 43 it is most likely that the failure mode was not pure compression but a mixed mode with pre-failure due to buckling as well as compression. This possibility was mitigated as much as possible within this test method by limiting the unsupported gauge length. Thus, when taking into consideration the cross-sectional area variability as well as the intra-specimen consistency and comparison to the carbon fiber test samples, although the failure mode was most likely a mixed mode of buckling and compression, the determined average values of the ultimate compressive strength for both the light (5330) and standard (5309) flax fiber materials will be considered to be representative of an approximation of the ultimate compressive strength.

4.3.3 Limitations

The static tensile and compressive strengths of all tested materials were within expectations when compared to literature. However, for a more thorough understanding and statistical significant result, more tests should be performed. All test samples were from the same hollow cylinder, and thus may only be representative of that specific cylinder. For a greater confidence in data representation, multiple cylinders should be manufactured for a greater variety sample set.

An interesting additional source of data would be microscopy images of the initial failure site, to investigate the failure mechanisms. This may be significant in the compression testing, as it was observed that samples most likely failed due to mixed mode buckling and compression and not pure compression. If the microscopy analysis indicated failure due to buckling, the test procedure could be adapted to attempt pure compression failure.

Finally, only the tensile and compressive static strengths of both the fiber and matrix direction were analyzed. For further characterization and understanding of the static material properties, shear strength, flexural strength, and/or torsional strength could also be analyzed. These additional characterizations were determined to be outside the scope of this study, due to the complex geometry of the specimens and time constraints.

5 Phase 2: Hybrid Dynamic Behaviour

5.1 Methodology

5.1.1 Identification of Laminate Parameters

An initial hybrid laminate optimization procedure was used to identify potential laminate designs for experimental characteristic studies. The variables that were considered in the modeled optimization analysis were as follows:

1) Laminate orientation can vary from 0^o to $\pm 20^o$ in the unidirectional material for maximum flexural stiffness (49). $\pm\theta$ plies will be added in pairs to ensure a balanced laminate
2) Laminate optimization will focus on the handle portion of the handlebar. Assumed variation in core laminate configuration has no significant effect on handlebar stiffness (49).
3) Total number of ply layers will range from 7-12 based on commercially available carbon fiber handlebar designs, dictated by flexural strength requirements
4) Limitation to quantity of flax material(s) used based on flexural strength requirements only
5) Outer core layer to be woven carbon fiber, as per current industry practice. No restriction as to outer layer of handle portion.

A total of 2 000 laminate configurations were identified satisfying the above parameters. To decrease the computational time of the FEA model of the handlebar, the equivalent stiffness (EI_{eq}) of the laminate was calculated assuming a hollow cylinder with the same geometry as the test samples. The equivalent stiffness of a hollow composite cylinder is a function of the laminate material properties and geometry, and can be calculated using Equation 12 below:

$$EI_{eq} = D_x = \frac{\pi}{4}\sum_{k=1}^{M} Q_{11}^{k}\left[(r_i + t_k)^4 - (r_i + t_{k-1})^4\right] \quad \textbf{Equation 12}$$

Where 'r_i' is the inner radius, 't_i' is the thickness of the ply layer, 'Q_{11}' is the modulus of the ply layer in the 11 direction, and 'D_x' is the equivalent flexural modulus of the tube structure. As the outer radius is constant at 22.2mm, the inner radius is a function of the laminate thickness. The modulus is a function of the material properties of the specific ply layer. This calculation was completed using internal McGill software (MLAM, Classical Composites Theory, McGill University 2006). For a hollow circular cross section beam, the input required is the specific laminate sequence and the resulting inner diameter dimension. The output is the equivalent stiffness. The equivalent stiffness at the thickest ("stem base") and thinnest (handle) cross sections were calculated and compared to the benchmark laminate. The benchmark laminate equivalent stiffness at the stem base with the layup of $[CW/C_5/CW]_T$ was calculated to be 1409 Nm^2, and at the handle with the laminate of $[CW/C_2/CW]_T$ was 237.04 Nm^2. All laminate configurations that exceeded these values were identified for further FEA optimization. A final design matrix of 200 laminate configurations were then analyzed using FEA for flexural strength and dynamic characteristics.

5.1.2 Finite Element Analysis Model

All finite element analysis models were generated using the ABAQUS 6.13-3 Software (Dassault Systems).

5.1.2.1 Initial Material Assumptions

Material properties for an anisotropic material in ABAQUS require additional material parameters to those tested for complete definition. Experimentally obtained strength data was used (Section 4.2) and where necessary material assumptions were made as per Table 11.

Table 11 - Anisotropic Material Assumptions

	Carbon Fiber		Flax Fiber	
Material Property	**Unidirectional (301)**	**Plain Weave (321)**	**Light Unidirectional (5330)**	**Standard Unidirectional (5309)**
Density	Test Data	Test Data	Test Data	Test Data
E_1	Test Data	Test Data	Test Data	Test Data
E_2	Test Data	Test Data	Test Data	Test Data
E_3	Due to Transverse Isotropy, $E_3 \approx E_2$			
ν_{12}	Material Data Sheet	Material Data Sheet	Assumed equivalent to Flax 5309	Material Data Sheet
ν_{13}	Material Data Sheet	Due to Transverse Isotropy, $\nu_{13} \approx \nu_{12}$	Estimated using Material Data sheet Flexural Properties [1]	Estimated using Material Data sheet Flexural Properties [1]
ν_{23}	Firehole Composite Estimation (50)		Firehole Composite Estimation for EGlass (50)	
G_{12}	Estimated using Material Data sheet Flexural Properties **[1]**	Material Data Sheet	Estimated using Material Data sheet Flexural Properties **[1]**	Estimated using Material Data sheet Flexural Properties **[1]**
G_{13}	Due to Transverse Isotropy, $G_{13} \approx G_{12}$			
G_{23}	Due to Transverse Isotropy $G_{23} \approx \frac{E_2}{2(1+\nu_{23})}$			
Fail Stress				
X_T	Test Data	Test Data	Test Data	Test Data
X_C	Test Data	Test Data	Test Data	Test Data
Y_T	Test Data	Test Data	Test Data	Test Data
Y_C	Test Data	Test Data	Test Data	Test Data
Shear Strength	Material Data Sheet	Material Data Sheet	Estimated using ratio of matrix tensile shear strength to shear strength **[2]**	Estimated using ratio of matrix tensile shear strength to shear strength **[2]**

Table Notes:

[1] ν_{13} and G_{12} are matrix-dominated properties. For isotropic materials

$$\nu_{13} = \nu_{12}\left(\frac{E_2}{E_1}\right); \quad G = \frac{E}{2(1+\nu)}$$

For the known values of the unidirectional carbon fiber, if the Poisson's Ratio ν_{13} and shear modulus G_{12} are calculated using the isotropic relationship and the given manufacturer flexural strength data, there is good agreement between the estimated value and the manufacturer value. Thus, for the flax materials ν_{13} and G_{12} were estimated using the isotropic relationship above and the given manufacturer flexural strength data.

[2] Shear strength, which is a matrix-dominated property, is approximately equivalent to the matrix tensile strength. For the flax material, the matrix tensile strength to (manufacturer) shear strength ratio of the unidirectional carbon fiber was used to calculate the flax shear strength(s) from the experimental matrix tensile strength.

A material-specific local coordinate system was defined in ABAQUS for all handlebar sections. Due to the multi-planar geometry, the material local coordinate system defined the laminate orientation of [0] about the longitudinal axis of the handlebar. An example of the laminate ply layer orientation for the handle portion is shown below in Figure 45.

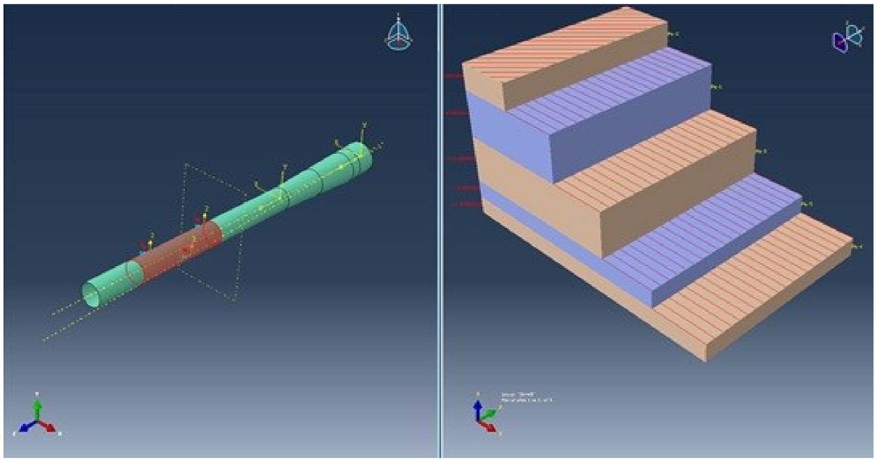

Figure 45 - Material Ply Orientation of Handle
Left: Material Direction of Handle: Local directions are 1 (Blue – Longitudinal), 2 (Yellow – Radial), 3 (Red – through thickness)
Right: Ply Stack Orientation: Ply-1 is the innermost ply, Ply-5 outermost

5.1.2.2 Handlebar Geometry

Due to handlebar geometry symmetry, half the handlebar was modeled in ABAQUS with the dimensions as per the Thompson HB-102 geometry design. The boundary condition was defined to restrict movement in all degrees of freedom for 30mm at the centre of the handlebar. This represented the boundary at the stem/handlebar clamp interface. The handlebar model geometry is shown below in Figure 46.

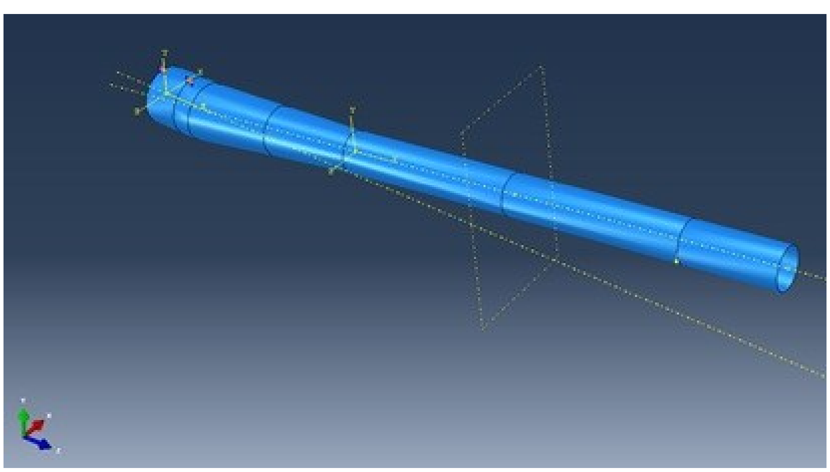

Figure 46 - ABAQUS Handlebar Half Geometry Model

5.1.2.3 Mesh

The model was meshed with 82 803 Continuum Shell S8R elements, with free mesh generation to allow for mesh convergence over the entire complicated geometry. Continuum Shell S8R elements are similar to conventional shell elements, where sections perpendicular to the shell plane remain perpendicular and transverse strain is neglected. However, continuum shell elements discretize a three-dimensional body, with the thickness of the element determined by the node position. This allows for great accuracy in applications such as composite modeling, as the built-in two-sided contact takes into account change of thickness within the layer. Material properties are individually specified for each laminate layer, increasing the accuracy of the model results.

5.1.2.4 Flexural Behaviour

The flexural behaviour of the proposed laminate was analyzed with the loading recommended by EN 14766-2006 (6). The load of -1 000N in the global y-direction was applied 50mm from the end of the handlebar. Maximum deflection at the handlebar tip was recorded. The Hashin-Rotem safety criterion was used to evaluate flexural failure. The safety criterion is defined as follows (51):

Fiber Tension ($\hat{\sigma}_{11} \geq 0$):

$$F_f^t = \left(\frac{\hat{\sigma}_{11}}{X^T}\right)^2 + \alpha\left(\frac{\hat{\tau}_{12}}{S^L}\right)^2$$

Fiber Compression ($\hat{\sigma}_{11} < 0$):

$$F_f^c = \left(\frac{\hat{\sigma}_{11}}{X^C}\right)^2$$

Where:

X^T: Longitudinal Tensile Strength

X^C: Longitudinal Compressive Strength

α = 0.0 for the Hashin-Rotem (1973) Criterion

Matrix Tension ($\hat{\sigma}_{22} \geq 0$):

$$F_m^t = \left(\frac{\hat{\sigma}_{22}}{Y^T}\right)^2 + \left(\frac{\hat{\tau}_{12}}{S^L}\right)^2$$

Matrix Compression ($\hat{\sigma}_{22} < 0$):

$$F_m^c = \left(\frac{\hat{\sigma}_{22}}{2S^T}\right)^2 + \left[\left(\frac{Y^C}{2S^T}\right)^2 - 1\right]\left(\frac{\hat{\sigma}_{22}}{Y^C}\right) + \left(\frac{\hat{\tau}_{12}}{S^L}\right)^2$$

Where:

Y^T: Transverse Tensile Strength

Y^C: Transverse Compressive Strength

S^L: Longitudinal Shear Strength

S^T: Transverse Shear Strength

$$S^T = \frac{Y^C}{2}$$

For each failure mode, a safety factor was calculated using the calculated failure force denoted by F_i and the associated ultimate strength in that failure mode direction. A safety factor of less than one indicated compliance, and a safety factor greater than one indicated structural failure in that failure mode.

5.1.2.5 Initial Dynamic Analysis

The first three natural frequencies their associated modal directions of the hollow cylinder geometry with a boundary condition of free-free and clamped were first predicted in ABAQUS. The extraction of the modal behaviour was performed with the Lanczos Eigensolver in ABAQUS. This preliminary step is dependent on the boundary conditions only; thus no load was applied. The ABAQUS model was designed as per Section 5.1.2, with the tube length 37.7cm, associated with the half length of the handlebar. The material directions and ply stacking orientation were verified to ensure that the 1-axis correlated with the longitudinal axis of the cylinder, and the 3-axis correlated with the through-thickness of the laminate. This is shown below in Figure 47.

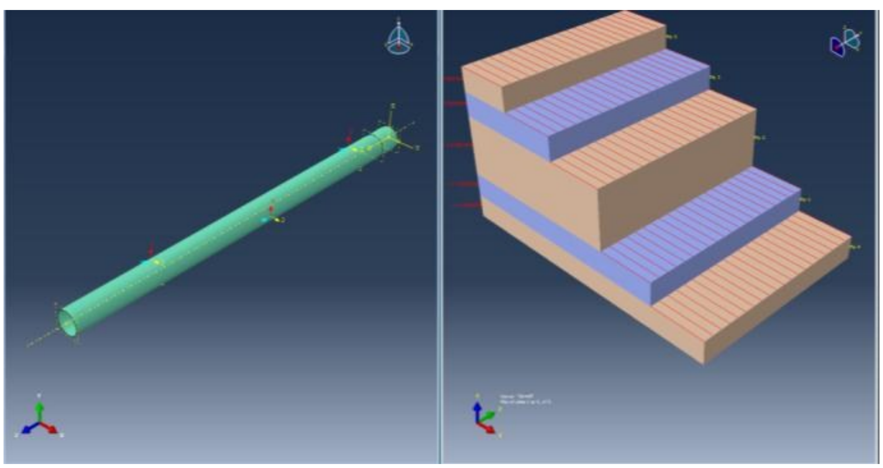

Figure 47 - Material Direction and Ply Stack Plot for Hollow Cylinder Test Specimen
Left: Material direction of composite: 1-axis (Blue), 2-axis (yellow), 3-axis (red)
Right: Ply stack orientation for FP2

For the clamped boundary condition movement was restricted in all degrees of freedom, applied 22mm from the end of the cylinder, correlating to the full length of the stem clamp length used in experimental verification. From the dynamic analysis the resulting mode shape and node and anti-node locations were determined. For the preliminary analysis, damping of the specimen was assumed to be proportional to the relative displacement of the sample at the anti-node location. The identified natural frequencies and relative damping behaviour were then compared for all specimens.

5.1.3 Microscopy

Microscopy was used to determine the fiber volume ratio and laminate quality. The specimens were cut to a length of 1cm with a fine-tooth band saw, cleaned, and then potted in clear epoxy. The potted specimens were then wet polished at low speed with three successive grade grit sandpapers and a final polish paper for 3 min/grade. After each grade, the samples were visually inspected with a microscope to determine polish quality. Subsequent to sample preparation, each cross section was visually inspected in a microscope, with four measurements taken to average laminate thickness. The fiber volume fraction was calculated as in Equation 13 below.

$$V_f = n\left(\frac{\frac{aerialdensity}{vol.density}}{t}\right) \qquad \textbf{Equation 13}$$

where ‘n’ is the number of layers, aerial density is the fiber density of the material given by the manufacturer [g/m^2], volume density is the specific volume density of the individual fiber: $1.45g/cm^3$ for flax and $1.76g/cm^3$ for carbon fiber (52) and ‘t’ is the total thickness of the laminate [μm].

5.1.4 Dynamic Testing of Hybrid Composites

From the results of the initial dynamic analysis performed in ABAQUS, twelve hollow cylinders were manufactured as per Section 3.1. The justification of laminates used is discussed in Section 5.2.2.3, and are shown below in Table 12.

Table 12 - Hybrid Composite Test Specimens

Specimen Name	Layup
Baseline	
BH	[CW/C_2/CW]
BC	[C_5]
BF	[F_5]
Fiber Placement	
FP1	[C/F/C_3]
FP2	[C_2/F/C_2]
FP3	[C_3/F/C]
FP4	[C_4/F]
Multiple Flax Layers	
DF1	[C/F_2/C_2]
DF2	[C_2/F_2/C]
DF3	[C_3/F_2]
DF4	[C/F/C/F/C]
DF5	[C_2/F/C/F]

where ‘CW’ denotes the plain weave carbon fiber and a [45] orientation; ‘C’ denotes unidirectional carbon fiber, and ‘F’ denotes standard unidirectional flax (5309). Subscripts indicate the number of layers with that material. All unidirectional carbon and flax layers are in the [0] orientation with respect to the longitudinal axis.

All specimens were analyzed for fiber volume fraction and laminate quality with microscopy. All dynamic tests were performed with a cylinder length of 38cm. For experimental methodology comparison, dynamic tests were performed using three measurement techniques: 1) Impact hammer stimulation and accelerometer measurement, 2) Impulse Excitation Technique (IET) with mechanical stimulation and microphone vibration measurement, and 3) IET with mechanical stimulation and laser displacement measurement.

5.1.4.1 Test Setup and Analysis

All experimental testing was performed with the same boundary conditions and analysis of data.

Boundary Conditions:

1) Free-Free: Simulated with the cylinder specimen supported by thin elastics approximately 9cm from either end, correlating to the modeled first natural frequency nodal points.
2) Clamped: Simulated with one end of the cylinder clamped to a bicycle handlebar stem, with a piece of insulating rubber at the stem/cylinder interface. The stem clamp was mounted to the supporting structure with custom-designed mounts.

From the ABAQUS model, the anti-nodes were defined to be at the end of the specimen for all natural frequencies. Thus, the input impulse and output measured vibration parameter were measured at the specimen ends. During testing, the input impulse was recorded, and the resulting time domain vibration response and FRF plots were generated. For all methods, ten input trials were performed and averaged. From the generated data, the natural frequencies were identified and first natural frequency damping factor identified from measurement output (Section 5.1.4.1.2) or calculated using the logarithmic regression method (Section 5.1.4.1.1).

5.1.4.1.1 Impact Hammer Technique

Measurements were obtained using LMS Instruments SCADA data acquisition system (LMS, TestLab, Siemens). The impulse was generated by an impact hammer (20-30VDC, 2-20mA) and recorded. The resulting vibration response was measured by two accelerometers (PCB Piezotronics, Sensitivity 100.9 mV/g) oriented in the arbitrary global y and z directions. TestLab recorded the acceleration response normalized to the input impulse force.

For the free-free boundary condition, the accelerometers were placed at opposite ends, to balance the additional weight of the accelerometers. The impact was applied in the opposite direction of the measuring accelerometer, on the opposite end. The free-free test set-up with impact direction in the arbitrary global y-direction is shown below in Figure 48.

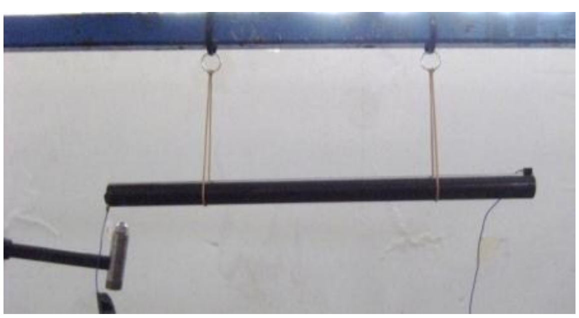

Figure 48 - Impact Hammer Free-Free Test Set-up

For the clamped boundary condition, the accelerometers were placed on the free end, and the impact applied directly opposite the measuring accelerometer. The clamped boundary test set-up is shown below in Figure 49 and Figure 50.

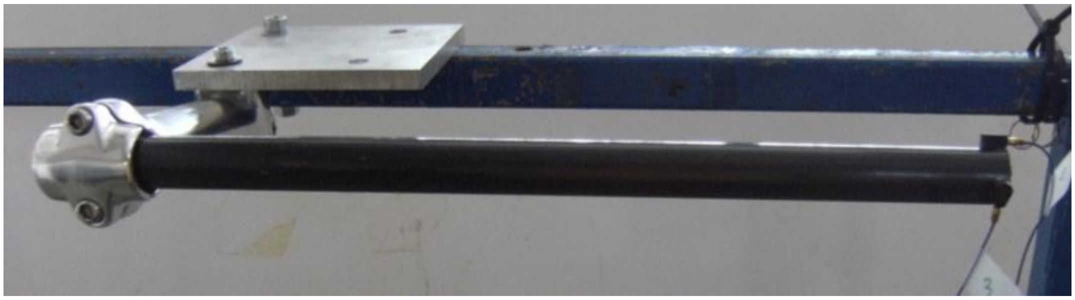

Figure 49 - Impact Hammer Clamped Test Set-Up

Figure 50 - Location of Impact for Clamped Boundary Condition

As is shown in Figure 49, due to the geometry of the stem clamp, the boundary condition in the y-direction may not be a fully clamped boundary condition, due to the small gap in the stem clamp.

The recorded time domain and FRF data were exported from TestLab into MATLAB (R2014a, MathWorks). The natural frequencies were determined from the FRF data using the "damp" function in MATLAB averaged for each impulse direction. The time domain signals were normalized to their individual maximum amplitude and then averaged for both directions. The signal envelope was then calculated for the damping factor calculation. For both boundary conditions, the damping factor was calculated using a curve fit function, assuming a curve described by the logarithmic decrement of the positive signal envelope (Equation 5) over the first natural frequency. In the time domain, the first natural frequency is indicated by the first region of signal decay to approximately 0g/N. The time domain signal was then processed using the Fast Fourier Transform (FFT) functionality. From the FFT plot in MATLAB the natural frequencies were identified. The natural frequencies from the output FRF signal and FFT methods were then compared.

5.1.4.1.2 Impulse Excitation Technique

The Impulse Excitation Technique (IET) used was adapted from ASTM C1259-08 (53). All data was recorded by RFDA-HTVP software, which automatically calculated the natural frequencies and damping factors from the FFT of the recorded raw data response, normalized to impulse. The impulse was generated by using a small tapping hammer in the same relative locations as in the impact hammer technique (Section 5.1.4.1.1). Specimen response was measured using both a microphone and a laser. The microphone measured vibration noise response which was converted to electrical signal, similar to a transducer. The laser (Polytec OFV 303 Sensor Head) measured displacement at the focal point. Due to apparatus limitations, both the microphone and laser measurements were made in the y-direction only. For the free-free condition, the samples were supported by a light nylon string. The clamped condition was tested in the same manner as for the impact hammer technique (Section 5.1.4.1.1). The test set-up for each measurement technique and boundary conditions are shown below in Figure 51 and Figure 52. Ten trials were performed for each sample, and the identified natural frequencies and damping factors were averaged.


Figure 51 - IET Free-Free Test Setup
Left: Laser; *Right:* Microphone


Figure 52 - IET Clamped Test Set-Up
Left: Laser; *Right:* Microphone

5.1.4.2 Hollow Cylinder Model Verification

To investigate the damping mechanisms of the hybrid laminates as suggested by van Vuure et. al. (29), the through-thickness strain energy density for the first three natural frequencies was modeled. The previous cylinder model was adapted to 3D geometry, as the through-thickness strain energy density is a 3D property. The thickness of the cylinder was modeled to correspond to the sum of the thickness of the individual plies of the tested layup. The material direction was specified to be consistent with the 2D Continuum Shell model, and is shown below in Figure 53.

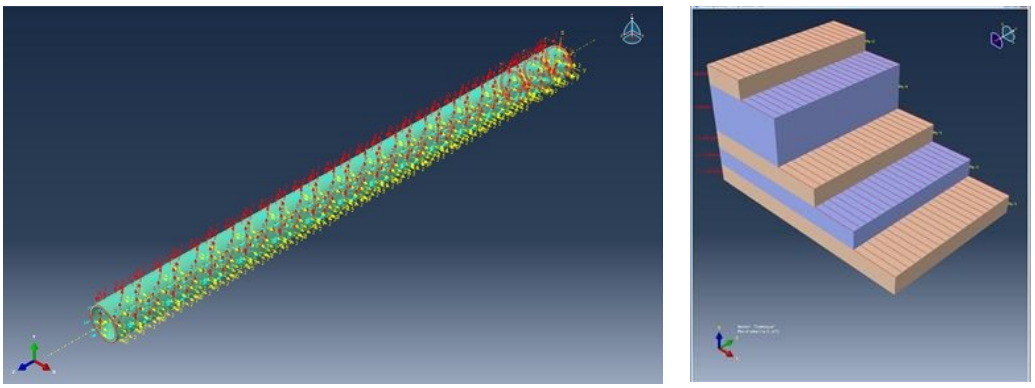

Figure 53 - Material and Ply Direction of Hollow Cylinder
Left: Material Direction of Cylinder: Local directions are 1 (Blue – Longitudinal), 2 (Yellow – Tangential), 3 (Red – Radial)
Right: Ply Stack Orientation: Ply-1 is the innermost ply, Ply-5 outermost

To define the composite material, the solid model was assigned a composite material layup prior to meshing. Three integration points were specified for each ply, associated with the top, middle, and bottom location of each ply. The element type was C3D20, a 20-node quadratic hex-shaped brick. The stacking direction of the elements was assigned to correlate with the laminate layup, with the top surface of the element corresponding to the outer surface of the cylinder. Figure 54 illustrates laminate stacking direction, with brown indicating the top (or outermost) surface of the element.

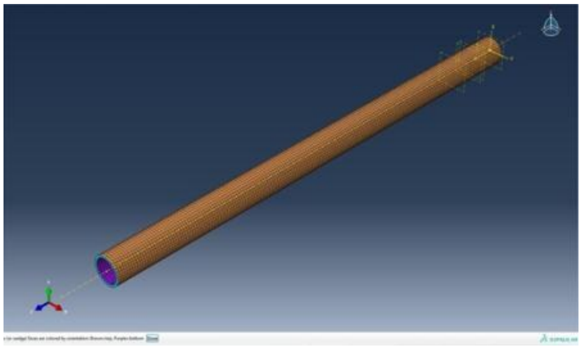

Figure 54 - Element Stack Direction of Hollow Cylinder
Purple: Element Bottom surface; *Brown:* Element Top surface

The model was first compiled for the static flexural bending performance (Section 5.1.2.4) to identify the high-stress area. The high-stress area was then partitioned and the model was re-meshed. The location of the high stress area and the partitioned mesh is shown below in Figure 55. The first three natural frequencies were calculated for each boundary condition using the Lanczos Eigensolver. For each natural frequency the through-thickness strain energy density was calculated at each integration point. To limit the scope of analysis to the critical region, the through thickness strain energy density at the centroid of each integration location was exported for all high-stress elements. The strain energy density was then analyzed for each natural frequency and boundary condition, and a single element was identified for further analysis based on the consistent high strain energy density for all conditions. From this data the effect of laminate, natural frequency, and boundary condition on the strain energy density was analyzed. Finally, the identified natural frequencies for the 3D model were compared to those obtained with the 2D model for model verification.

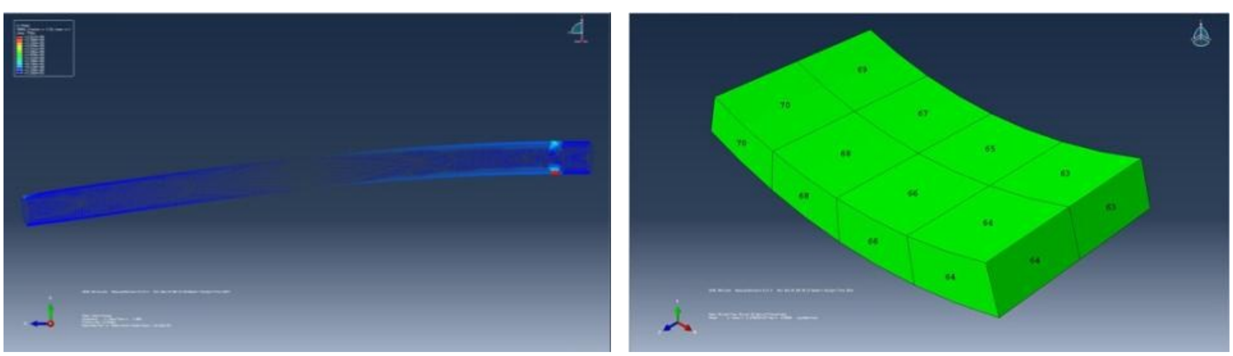

Figure 55 - High Stress Region of Hollow Cylinder Model
Left: Von Mises Stress resultant of flexural load case; Highlighted (Red) area location of high stress elements
Right: Element schematic of high stress elements show on *Left.*

5.2 Results

5.2.1 Identification of Laminate Parameters

As the purpose of the initial modeling was to determine the final laminate configurations for subsequent dynamic testing and verification, the results of interest of the analysis were the general trends of the identified laminates and not the values themselves. Thus, the general trends as observed through the models behaviour will be discussed, with final justification of experimental layups determined.

From the initial calculation of the equivalent stiffness and comparing the value to the benchmark, the laminate configuration iterations reduced in number from 2 000 to 200. This analysis modified the laminate number parameter for the hybrid laminate to be a minimum of nine layers for the stem base and five for the handle, to ensure the hybrid laminate would meet or exceed benchmark equivalent stiffness. The initial hybrid laminate design guidelines were as follows:

1) The first ply layer was included in the handle laminate. If the inner core was composed of a ±θ pair, the first two layers of the handle laminate were the inner core layers.
2) The following layers were composed of additional core thickness layers, of [0] unidirectional carbon fiber. Depending on the final ply of the handle laminate, the core was either three or four layers in thickness.
3) The final ply in the stem and transition handlebar layers was always a [45] carbon plain weave. This was an identified design constraint to decrease the probability of fiber splitting of the handlebar in final assembly.

The variables for handle laminate optimization were as follows:

1) *Effect of number of flax layers and position of flax layers*: All ply layers were oriented in [0], with no outer [45] carbon plain weave layer.
2) *Effect of [45] carbon plain weave outer layer*: All laminate designs identified in **Step 1** were re-modeled with an outer [45] carbon plain weave ply. This isolated the effect of the carbon fiber plain weave layer in the handle laminate.

3) *Effect of ±θ layers*: ±θ pairs were modeled in both unidirectional flax and carbon fiber layers. Position of the ±θ pairs was also varied.
4) *Effect of Hybrid-Hybrid laminates*: In this investigation, *Hybrid-Hybrid* laminate refers to a laminate with carbon and both types of flax materials. Thus, all laminate designs identified in **Step 1**, with one or more carbon fiber layers replaced with one or more layers of unidirectional light (5330) flax and/or unidirectional standard (5309) flax were investigated.

5.2.2 Finite Element Analysis Model: Initial Results

5.2.2.1 Flexural Behaviour

For all laminate configurations the critical Hashin-Rotem safety factor was failure due to fiber compression, at the last ply drop-off between the transition and handle cross section, on the underside of the handlebar. This is illustrated below in Figure 56, with the benchmark laminate.

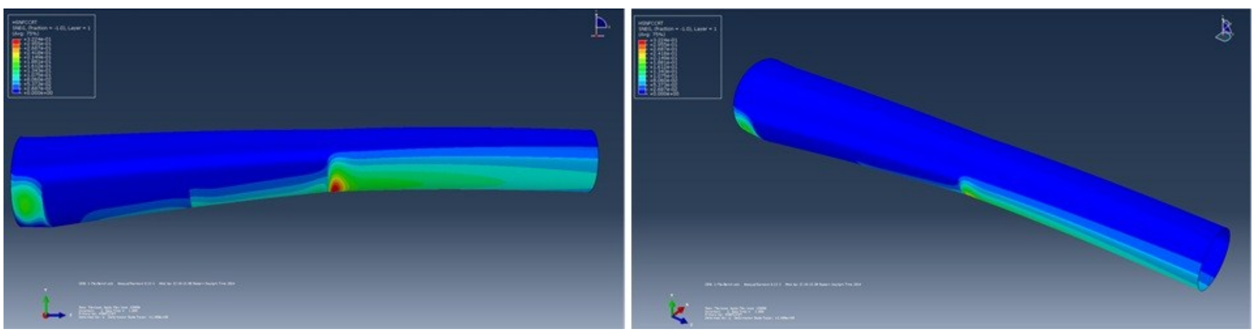

Figure 56 - Hashin-Rotem Failure Criterion Values for Flexure for Benchmark Laminate

With respect to the flexural results, the following observations were made:
Handlebar failure is predicted if:

- The first ply layer is flax
- The number of unidirectional light flax (5330) layers exceed one
- The number of unidirectional standard flax (5309) layers exceed three
- The outer handle layer is the carbon fiber plain weave at [45]
- [±10] layers of carbon unidirectional with a unidirectional light flax (5330) layer if and only if either the [±10] carbon fiber or single flax layers are in ply positions 1 or 2.
- [±10] layers of carbon unidirectional with more than two unidirectional standard flax (5309) layers

- [±20] layers of unidirectional carbon fiber with any flax layers
- Any combination of [±θ] layers made with flax material will most likely fail, with the exception of the [±10] Flax (5309) layers in Plies 2-3 or Plies 3-4.

The safety factor for fiber compression significantly decreases as:

- Flax layers move from innermost position to outermost position
- [±θ] layers move from the innermost positions to outermost positions
- The inclusion of unidirectional light flax (5330) to a hybrid-hybrid including standard flax (5309) decreases the safety factor as according to the rule of mixtures

For all designs, the hybrid composites had a smaller maximum deflection but a significantly greater Hashin-Rotem safety factor when compared to the benchmark laminate: ~140% increase for the inclusion of one flax layer, and ~180% increase with two flax layers. The above observations of hybrid laminate performance act as design guidelines, resulting in hybrid laminate configurations where flexural failure is not predicted, regardless of Hashin-Rotem safety factor increase.

5.2.2.2 Initial Dynamic Analysis

For all laminate configurations that satisfied the flexural failure criteria the dynamic response was compared for the first three natural frequencies. The following observations regarding the laminate design parameters and effect on dynamic properties were made.

Magnitude of natural frequencies:

- All laminates had a first natural frequency greater than 100Hz, with the lowest natural frequency in the order of 300Hz.
- All hybrid laminates with one flax layer have higher natural frequencies than the benchmark; with two flax layers the natural frequencies of the hybrid are marginally lower than the benchmark
- The unidirectional light flax (5330) hybrids have higher first natural frequencies (376 Hz) than the standard flax (5309) hybrids (350 Hz)

- As the number of flax layers increases, the natural frequencies decrease by 50Hz.
- As the flax layers move to the outermost positions, the natural frequencies decrease by ~9Hz.
- Natural frequency is not a function of ply orientation: there was no change in natural frequencies with the addition of ±θ layers.

Mode shape is a function of the ply orientation, and independent of the material composition of the laminate. Thus, the dominate mode shape for the first three natural frequencies for all $[0]_5$ laminates are X-displacement, Y-displacement, and Z-rotation respectfully. The addition of ±θ layers result in a change in direction of the third mode shape only: as the [±θ] pair moves to the outermost position, the dominant mode shape of the third natural frequency changes from Z-rotation to X-displacement to Y-displacement. This is equivalent to the mode shapes of the benchmark laminate.

Damping behaviour of the natural frequencies:

For the initial model, damping was estimated by the given relative amplitude of displacement at the anti-nodes.

- For a single flax hybrid, the damping increases by 3% (light flax 5330) to 5% (standard flax 5309) as the flax layer moves to the outermost position.
- As the number of flax layers increases, the damping of the first two natural frequencies increases by 21% (two flax layers) to 40% (three flax layers). The third natural frequency damping increases by ~16% (two flax layers) and 29% (three flax layers)
- The standard flax (5309) has 13-15% greater damping compared to light flax (5330).
- Damping decreases significantly (~25%) with the inclusion of the [±θ] pair in the third natural frequency only.
- There is no damping improvement of a single flax layer hybrid compared to the benchmark in the first natural frequency: damping decreases (i.e. increase in vibration amplitude) by ~17%. A double flax layer hybrid has an increase in damping of ~9%.

5.2.2.3 Identification of Laminates for Experimental Validation

Based on the above model results and observations, the following experimental hybrid laminates were identified:

1) The unidirectional standard flax (5309) will be used to increase the sample set
2) All hybrid laminates will be made with a $[0]_5$ laminate
3) Benchmark material cylinders of $[0]_5$ of unidirectional carbon fiber and standard flax will be tested for material comparisons
4) Effect of flax on hybrid performance will be assessed with the following two sample groups:
    a. Flax Layer Position: $[C/F/C_3]$; $[C_2/F/C_2]$; $[C_3/F/C]$; $[C_4/F]$
    b. Multiple Flax Layers: $[C/F_2/C_2]$; $[C_2/F_2/C]$; $[C_3/F_2]$; $[C/F/C/F/C]$; $[C_2/F/C/F]$

Additionally, the following design variables were omitted from experimental validation due to their significant decrease in flexural strength and/or minimal impact on damping characteristics:

1) Effect of outer plain weave carbon fiber layer
2) Effect of $[\pm\theta]$ layers
3) Hybrid-Hybrid laminates

5.2.3 Microscopy

5.2.3.1 Fiber Volume Fraction

The average thickness of each sample was measured in four locations using a microscope. The thicknesses were averaged, and the fiber volume fraction for each sample was calculated using Equation 13. The sample thicknesses and fiber volume fractions are shown below in Table 13.

Table 13 - Fiber Volume Fraction of Hybrid Cylinder Samples

			Fiber Volume Fraction		
Sample	**Average Thickness (t) [mm]**	**Thickness Standard Deviation**	**Carbon Fiber - Unidirectional (301)**	**Standard Flax (5309)**	**Total Sample Fiber Volume Fraction**
Benchmark Material Samples					
B-H	0.70	0.16	24.2%	31.5% (Carbon Fiber - Plain Weave (321)	55.7%
B-C	0.90	0.26	47.2%	0.00%	47.2%
B-F	2.53	0.28	0.00%	40.9%	40.9%
Flax Layer Placement Samples					
FP-1	1.27	0.08	26.9%	16.3%	43.3%
FP-2	1.48	0.47	23.0%	14.0%	37.0%
FP-3	1.28	0.17	26.6%	16.2%	42.8%
FP-4	1.36	0.21	25.2%	15.3%	40.4%
Average	**1.35**	**0.10**	**25.4%**	**15.4%**	**40.9%**
Multiple Flax Layer Samples					
DF-1	1.78	0.13	14.4%	23.2%	37.6%
DF_2	1.77	0.58	14.4%	23.4%	37.8%
DF_3	1.65	0.58	15.5%	25.0%	40.5%
DF_4	1.66	0.26	15.4%	24.9%	40.3%
DF_5	1.39	0.31	18.4%	29.7%	48.0%
Average	**1.65**	**0.16**	**15.6%**	**25.3%**	**40.8%**

5.2.3.2 Laminate Quality

In general, the laminate quality of all the samples was very good. The characteristics of the porosities, voids, and potential cracks were dependant on the laminate material and not on laminate configuration. Representative images of the laminate quality and associated properties are shown below in Figure 57 - Figure 63.

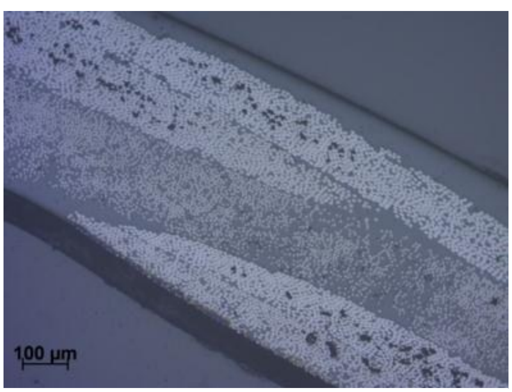

Figure 57 - Cross Section of Benchmark Handlebar

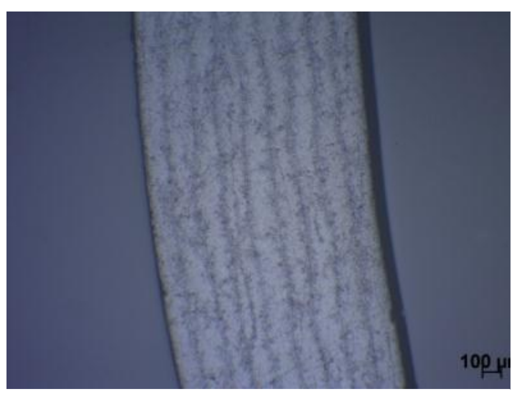

Figure 58 - Cross Section of Carbon Fiber Unidirectional Sample (BC)

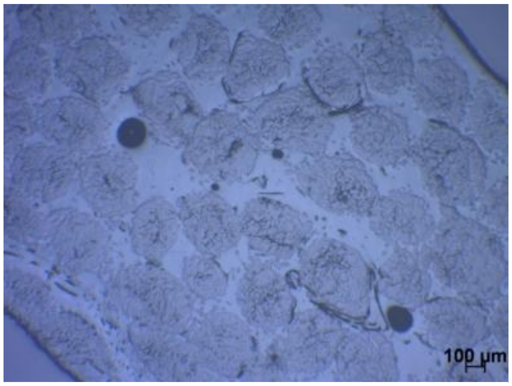

Figure 59 - Cross Section of Standard Flax Sample (BF)

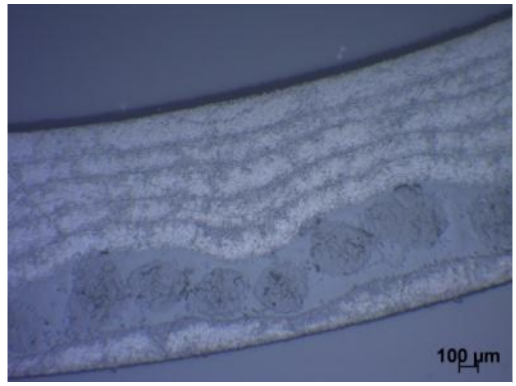

Figure 60 - Cross Section of Single Fiber Layer Sample (FP3): [C_3/F/C]

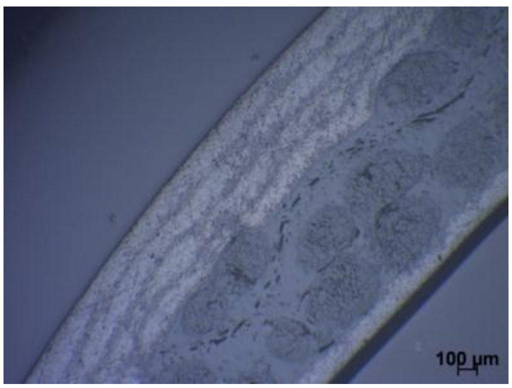

Figure 61 - Cross Section of Single Fiber Layer Sample (FP1): [C/F/C_3]

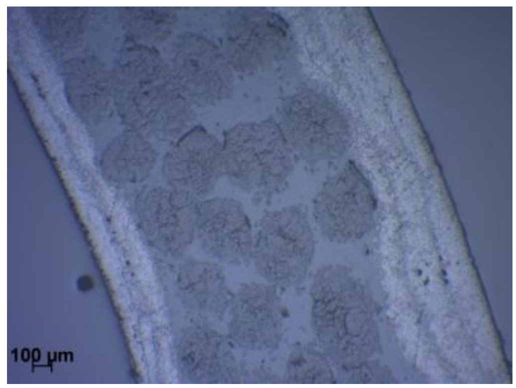

Figure 62 - Cross Section of Multiple Fiber Layer Sample (DF1): [C/F_2/C_2]

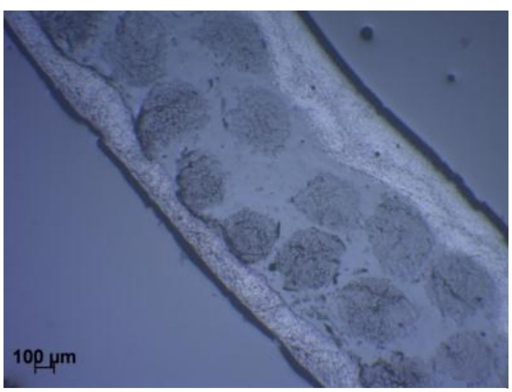

Figure 63 - Cross Section of Multiple Fiber Layer Sample (DF2): [C_2/F_2/C]

Figure 57 above illustrates the difference in material quality between the unidirectional carbon fiber and the plain weave carbon fiber in the benchmark handlebar laminate. The plain weave layers have a higher void density than the unidirectional carbon fiber. This is most likely due to insufficient resin in the prepreg material, and/or material age.

Figure 59 illustrates typical voids and porosities found in the flax layers. The cracks between fibers are porosities at the fiber/matrix interface. Figure 61 depicts the effect of the stabilizing yarn on the laminate quality. The long line of porosities between the first and second flax layer is the stabilizing yarn, which holds the flax fibers in place in the prepreg. As the samples were prepared with the unidirectional fibers pointing out of the page, the stabilizing yarn is along the longitudinal plane. Thus, those porosities may not be an indication of defects in the laminate, but rather just the visibility of the stabilizing yarn.

Figure 63 above depicts a large crack at the carbon/flax interface. This characteristic is most likely an artefact of sample preparation, as it was only observed in the 'bottom' of the band saw cuts, and thus pulled through the blade. The force required to cut the sample may have induced the intralaminar crack, and therefore appears to be a defect. As the tubes are cylindrical, the opposing side ('top' of the cylinder) of the sample was pushed through the band saw. In all cases where the intralaminar crack was present in the pull side, no crack was present in the pushed side.

5.2.4 Dynamic Testing

5.2.4.1 Model Prediction of Natural Frequencies

The ABAQUS program identified natural frequencies are shown below in Table 14 and Table 15 for the free-free and clamped boundary conditions respectfully. The associated mode shapes are shown below in Figure 64 and Figure 65.

Table 14 - Model Predictions of Natural Frequencies: Free-Free Boundary Condition

	Natural Frequency [Hz]				
Sample	**First**	**Second**	**Third**	**Fourth**	**Fifth**
Benchmark Material Samples					
BH	1166	1166	3072	3072	4203
BC	1463	1463	2147	2341	2341
BF	801.6	801.6	1502	1876	1876
Flax Layer Placement Samples					
FP1	1279	1279	1954	2799	2799
FP2	1270	1270	1940	2782	2782
FP3	1261	1261	1926	2765	2765
FP4	1252	1252	1910	2412	2412
Multiple Flax Layer Samples					
DF1	1130	1130	1802	2513	2513
DF2	1113	1113	1776	2479	2479
DF3	1095	1095	1749	2441	2441
DF4	1121	1121	1789	2495	2495
DF5	1104	1104	1762	2459	2459

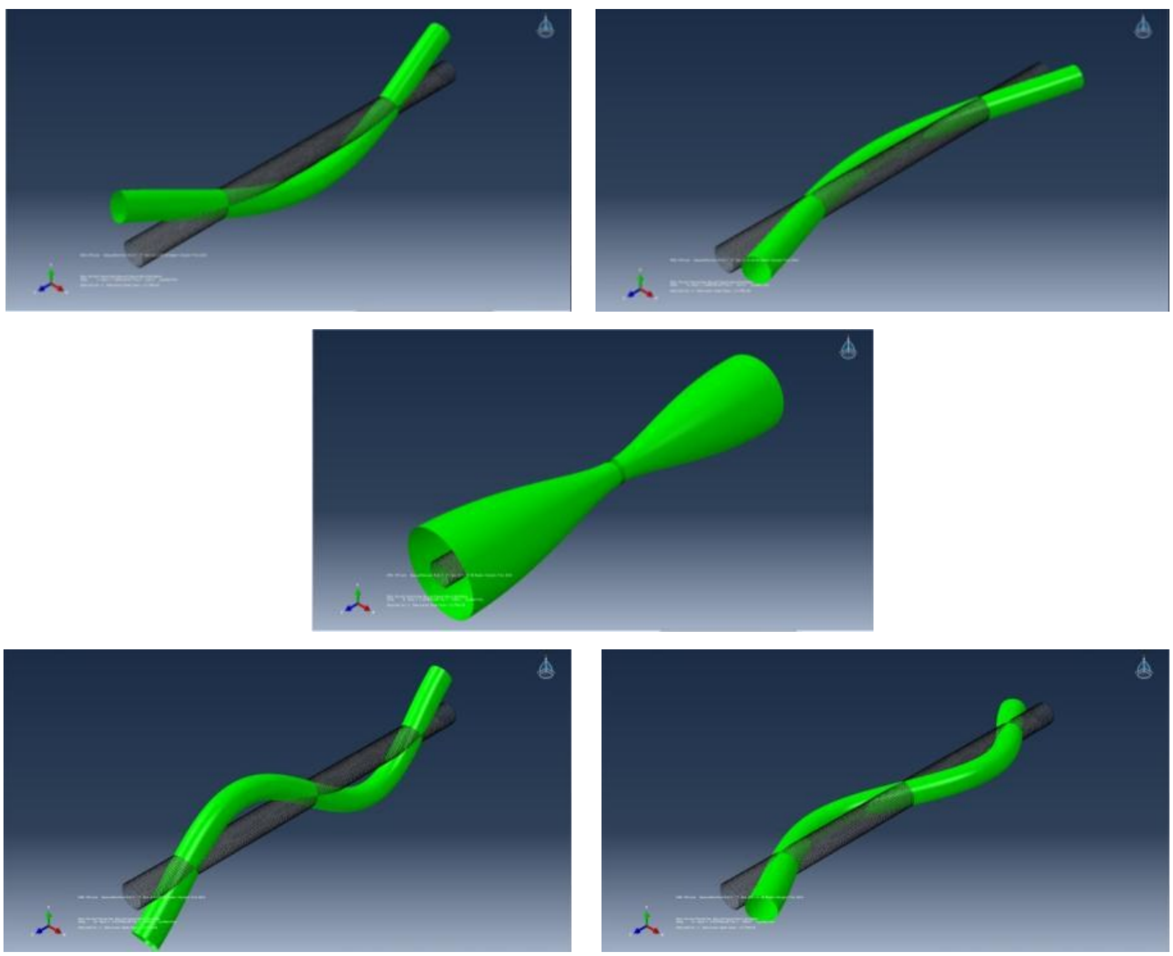

Figure 64 - Free-Free Modal Shapes for Hollow Cylinder
Top: First *(Left)* and Second *(Right)* Modal Shape; *Centre:* Third Modal Shape; *Bottom:* Fourth *(Left)* and Fifth *(Right)* Modal Shape. Note for Sample BH, the Third/Fourth and Fifth modal shapes were reversed.

Table 15 - Model Predictions of Natural Frequencies: Clamped Boundary Condition

	Natural Frequency [Hz]				
Sample	**First**	**Second**	**Third**	**Fourth**	**Fifth**
Benchmark Material Samples					
BH	210.3	210.3	1262	1262	2368
BC	279.5	279.5	1140	1357	1357
BF	149.1	149.1	793.0	793.0	798.0
Flax Layer Placement Samples					
FP1	243.1	243.1	1038	1200	1200
FP2	241.4	241.4	1030	1193	1193
FP3	239.7	239.7	1023	1185	1185
FP4	237.8	237.8	1015	1177	1177
Multiple Flax Layer Samples					
DF1	213.6	213.6	957.1	1074	1074
DF2	210.3	210.3	943.3	1059	1059
DF3	206.9	206.9	928.9	1043	1043
DF4	212.0	212.0	950.0	1066	1066
DF5	208.6	208.6	935.9	1051	1051

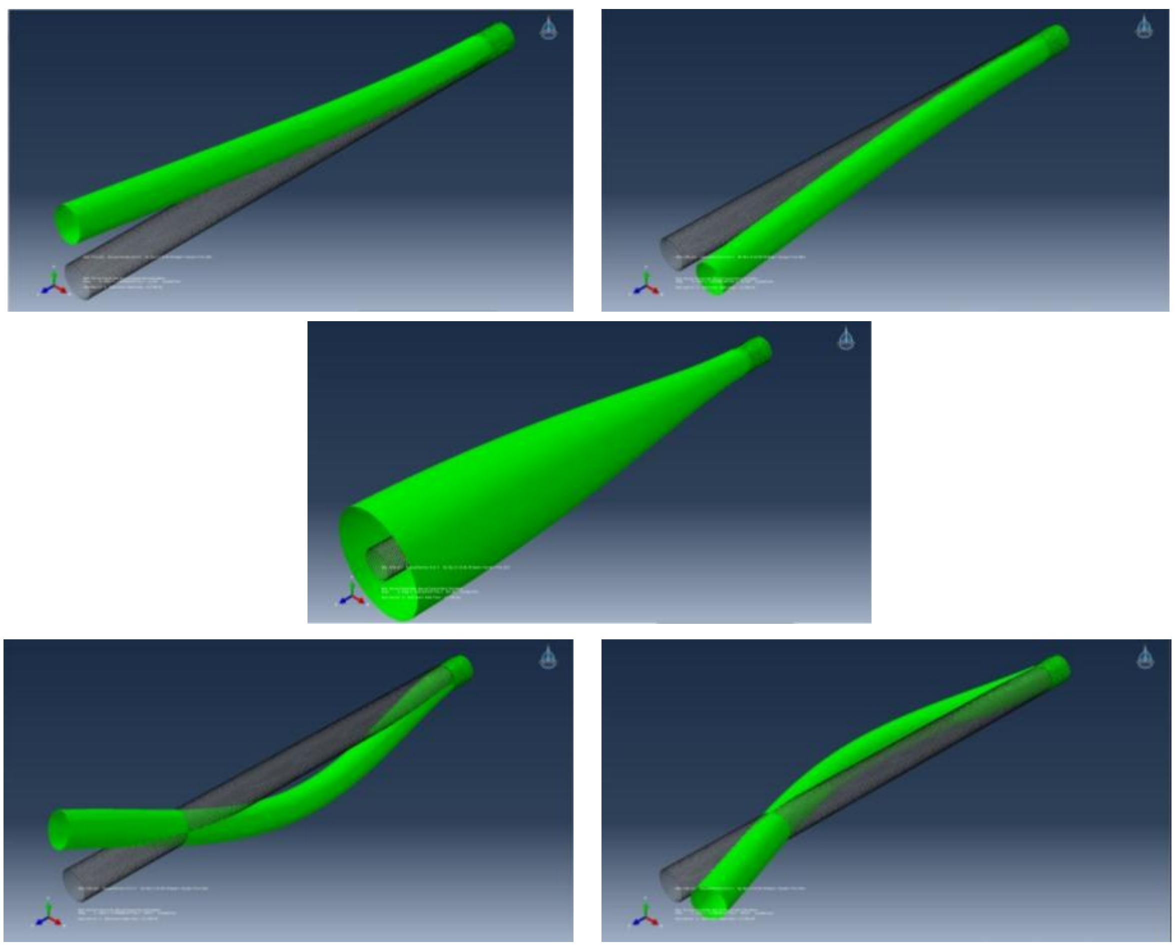

Figure 65 - Clamped Modal Shapes for Hollow Cylinder
Top: First *(Left)* and Second *(Right)* Modal Shape; *Centre:* Third Modal Shape; *Bottom:* Fourth *(Left)* and Fifth *(Right)* Modal Shape. Note for Samples BH and BF, the Third and Fourth/Fifth modal shapes were reversed.

5.2.4.2 Impact Hammer Technique

The averaged natural frequencies, damping factor, and time to equilibrium are presented in Section 5.2.4.3. The dynamic behaviour of the hybrid composite cylinders for the free-free boundary condition is shown in Table 16, and the clamped boundary condition in Table 18. There was good agreement with the FRF and FFT identified natural frequencies for the free-free boundary condition. However, due to noise present in the recorded FRF for the clamped boundary condition illustrated below with the benchmark handlebar sample (Figure 66), the FFT analysis presented very different results. Both are shown in Table 18.

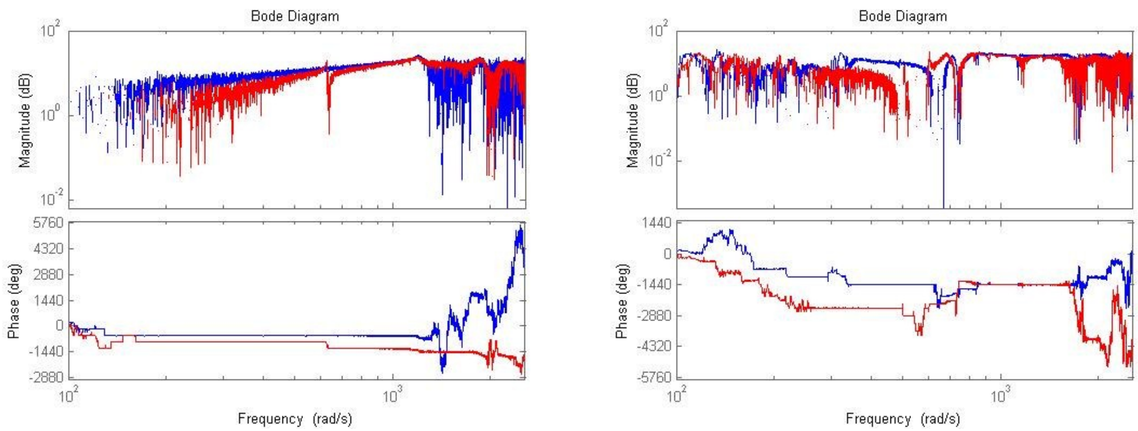

Figure 66 - Bode Plots of Benchmark (BH) Specimen Impact Hammer FRF Response
Left: Free-Free Boundary Condition Response; *Right:* Clamped Boundary Condition Response
For both: Blue indicates ‘y’ direction, Red indicates ‘z’ direction

In addition to the real-time convergence plot recorded by TestLab, characteristics of a noisy FRF plot include multiple spikes in magnitude over a short period associated with no phase change for the same frequency. For both Bode plots it is evident that the measurements between 300Hz-1000Hz are more coherent than from 100-300Hz and greater than 1020Hz. An example of coherent natural frequency identification is shown in the free-free Bode plot in Figure 66 above (left). The red change in magnitude at approximately 600Hz is associated with a phase change, indicating a natural frequency. The clamped Bode plot does not have equivalent characteristics throughout, and is thus can be considered noisy.

In theory, the cross-section of the hollow cylinder is symmetrical, and thus the dynamic response in the y and z directions should be simultaneous and equal in magnitude, as shown in the

ABAQUS model. However, this behaviour was not experimentally validated, as is illustrated in Figure 66. This may be due to sample variation including variation in cross-sectional area/thickness and deviation in the laminate orientation. This behaviour may also be due to human error during the test procedure, with the impulse not perfectly aligned with the measuring accelerometer direction. Boundary condition simulation may have also contributed to this deviation. For the free-free boundary condition it was difficult to obtain a clean impact signal in the y-direction due to double bounce back from the supporting elastics. This was verified with the coherence plot, generated by TestLab while measurements were occurring. For the clamped boundary condition, some vibration may be permitted at the base of the handlebar in the y-direction due to the small gap in the stem clamp (Figure 49), despite the rubber insert damper, intended for this purpose.

The free-free time domain behaviour is shown below in Figure 67 - Figure 69, and the clamped boundary condition in Figure 70 - Figure 72.

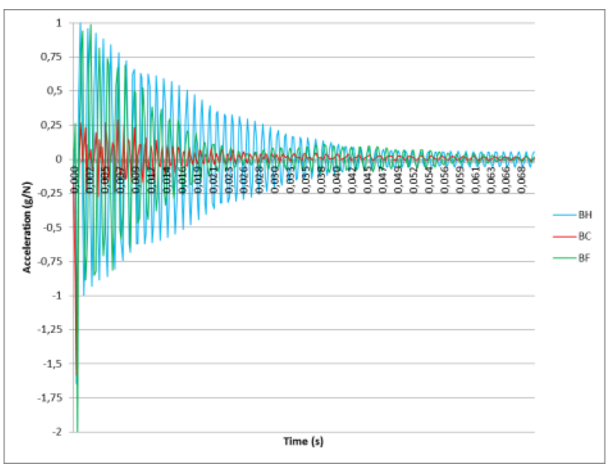

Figure 67 - Impact Hammer Dynamic Response: Free-Free Condition of Benchmark Samples

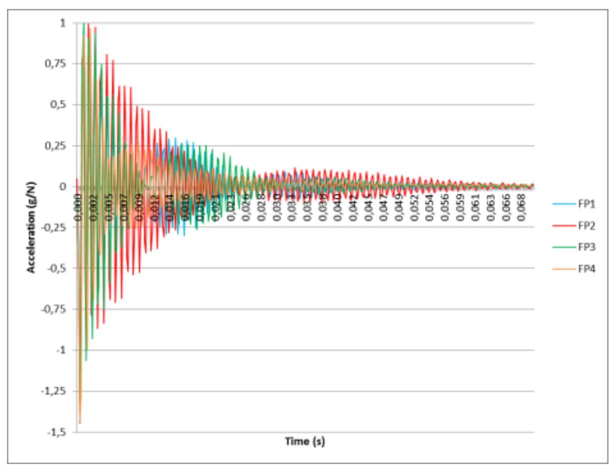

Figure 68 - Impact Hammer Dynamic Response: Free-Free Condition of Fiber Placement Samples

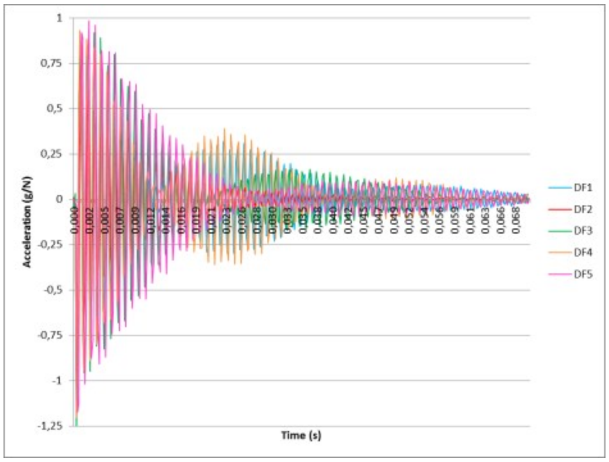

Figure 69 - Impact Hammer Dynamic Response: Free-Free Condition of Multiple Flax Layer Samples

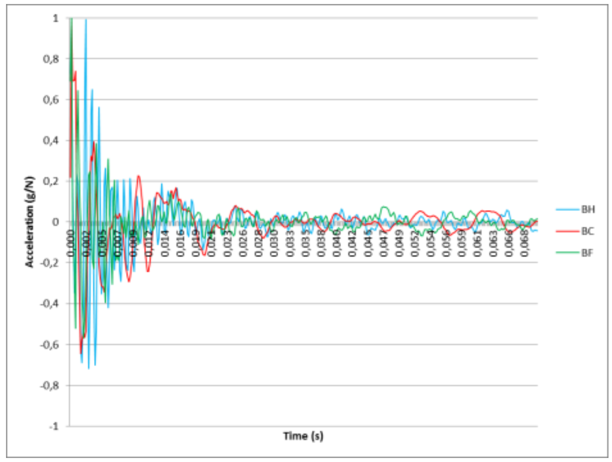

Figure 70 - Impact Hammer Dynamic Response: Clamped Condition of Benchmark Samples

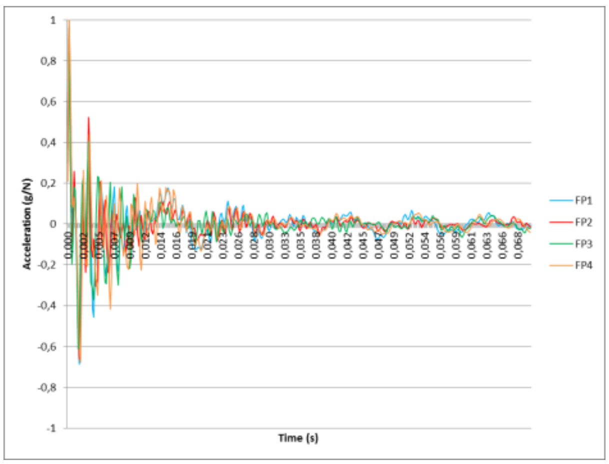

Figure 71 - Impact Hammer Dynamic Response: Clamped Condition of Fiber Placement Samples

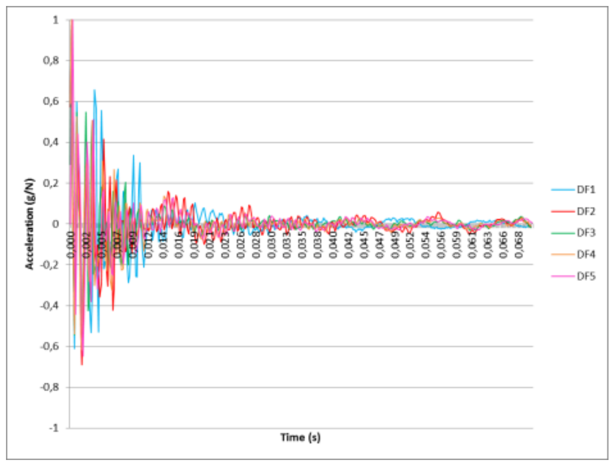

Figure 72 - Impact Hammer Dynamic Response: Clamped Condition of Multiple Flax Layer Samples

5.2.4.3 Summary of Dynamic Properties

5.2.4.3.1 Free-Free Boundary Condition

A summary table comparing the first three natural frequencies as identified by the model, impact hammer, and IET methods is shown below in Table 16. As is illustrated, the experimental data did not consistently identify the ABAQUS modeled third natural frequency, correlating to expansion along the longitudinal axis (Figure 64). Thus for comparison, the experimental natural frequencies were compared to the predicted natural frequencies associated with the sinusoidal mode shapes (Figure 64). This percent variation is shown in Table 16 in brackets.

Table 16 - Summary of Natural Frequencies: Free-Free Boundary Condition

Sample	Natural Frequency [Hz]	Model	Impact Hammer	IET: Microphone	IET: Laser
Benchmark Material Samples					
BH	First	1166	852.9 (26.9%)	958.6 (17.8%)	964 (17.3%)
	Second	3072	2287 (25.6%)	2607 (15.1%)	2630 (14.4%)
	Third	4203		4192	4170
BC	First	1463	1217 (16.8%)	1355 (7.3%)	1316 (10.0%)
	Second	2147	1908 (18.5%)	2094 (10.6%)	1358 (42.0%)
	Third	2341			2347
BF	First	801.6	750.7 (6.4%)	782.9 (2.3%)	779 (2.8%)
	Second	1502	1877 (0.1%)	1925 (2.6%)	1911 (1.9%)
	Third	1876			
Flax Layer Placement Samples					
FP1	First	1279	1112 (13.1%)	1184 (7.4%)	1209 (5.5%)
	Second	1954	1901 (32.1%)	2614 (6.6%)	
	Third	2799			
FP2	First	1270	1100 (13.4%)	1178 (7.3%)	1180 (7.1%)
	Second	1940	2165 (22.2%)	2695 (3.2%)	
	Third	2782			
FP3	First	1261	1107 (12.2%)	1187 (5.9%)	1216 (3.6%)
	Second	1926	1844 (33.3%)	2667 (3.5%)	2672 (3.3%)
	Third	2765		3523	
FP4	First	1252	1063 (15.1%)	1097 (12.4%)	1096 (12.4%)
	Second	1910	1597 (33.8%)	1169 (51.5%)	1170 (51.5%)
	Third	2412		2552	
Multiple Flax Layer Samples					
DF1	First	1130	980.9 (13.2%)	1052 (6.9%)	1060 (6.2%)
	Second	1802	2252 (10.4%)	2449 (2.6%)	2454 (2.3%)
	Third	2513		4169	
DF2	First	1113	936.9 (15.8%)	1012 (9.0%)	1012 (9.1%)
	Second	1776	1884 (24.0%)	2344 (5.4%)	2348 (5.3%)
	Third	2479		4182	
DF3	First	1095	957.4 (12.6%)	1023 (6.6%)	1010 (7.8%)
	Second	1749	2251 (7.8%)	2364 (3.1%)	2397 (1.8%)
	Third	2441		3444	
DF4	First	1121	977.2 (12.9%)	1014 (9.5%)	1050 (6.4%)
	Second	1789	2273 (8.9%)	2395 (4%)	2434 (2.4%)
	Third	2495		3554	
DF5	First	1104	969.3 (12.2%)	1024 (7.2%)	1037 (6.1%)
	Second	1762	2204 (10.4%)	2405 (2.2%)	2419 (1.6%)
	Third	2459			

Unlike the IET methods, the Impact Hammer damping factor was calculated as described in Section 5.1.4.1.1. Figure 73 below illustrates the calculated envelope of the time domain signal for the benchmark laminate specimen with the free-free boundary condition in MATLAB. The bold outline of the normalized time domain signal indicates the maximum envelope function of the signal. From this function, the logarithmic decay curve fit (Equation 5) was employed in

MATLAB to identify the damping factor. The identified damping factor for the first natural frequency is shown in Table 17.

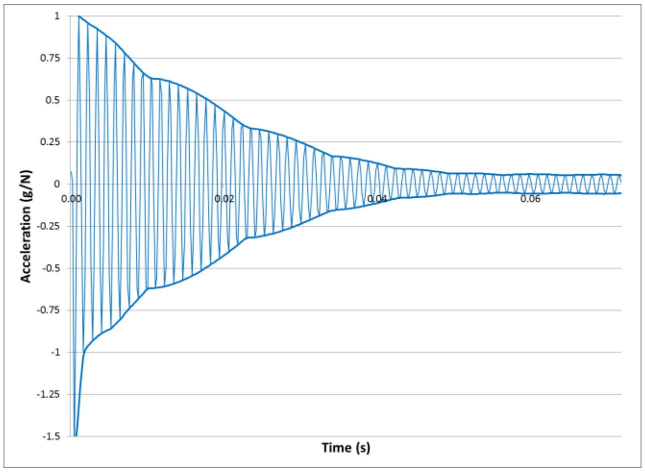

Figure 73 - MATLAB Normalized Time Domain Envelope for Damping Factor Calculation: Benchmark (BH) Specimen: Free-Free Boundary Condition

Table 17 - Summary of Damping Factors (%): Free-Free Boundary Condition

Sample	Impact Hammer		IET: Microphone	IET: Laser
	Decay Time (s)	Damping Factor		
Benchmark Material Samples				
BH	0.056	0.96	1.17	1.75
BC	0.018	1.91	0.92	0.51
BF	0.028	2.47	1.64	1.78
Flax Layer Placement Samples				
FP1	0.009	8.69	1.02	1.04
FP2	0.025	1.63	1.15	1.06
FP3	0.012	3.94	1.55	1.35
FP4	0.007	4.70	1.40	1.19
Multiple Flax Layer Samples				
DF1	0.013	3.61	1.62	1.33
DF2	0.050	1.41	0.80	1.20
DF3	0.022	2.98	1.11	2.03
DF4	0.013	3.78	1.08	1.04
DF5	0.028	1.94	1.44	0.90

5.2.4.3.2 Clamped Boundary Condition

A summary table comparing the first three natural frequencies as identified by ABAQUS and the experimental methods is shown below in Table 18 with the identified damping factor for the first natural frequency in Table 19. To determine the FFT natural frequencies for the impact hammer specimens, the transformed FFT data (Section 5.1.4.1.1) was plotted in MATLAB. From the plot, the local maxima were identified, corresponding to the natural frequencies of the system. This is illustrated below with the benchmark laminate specimen FFT plot (Figure 74).

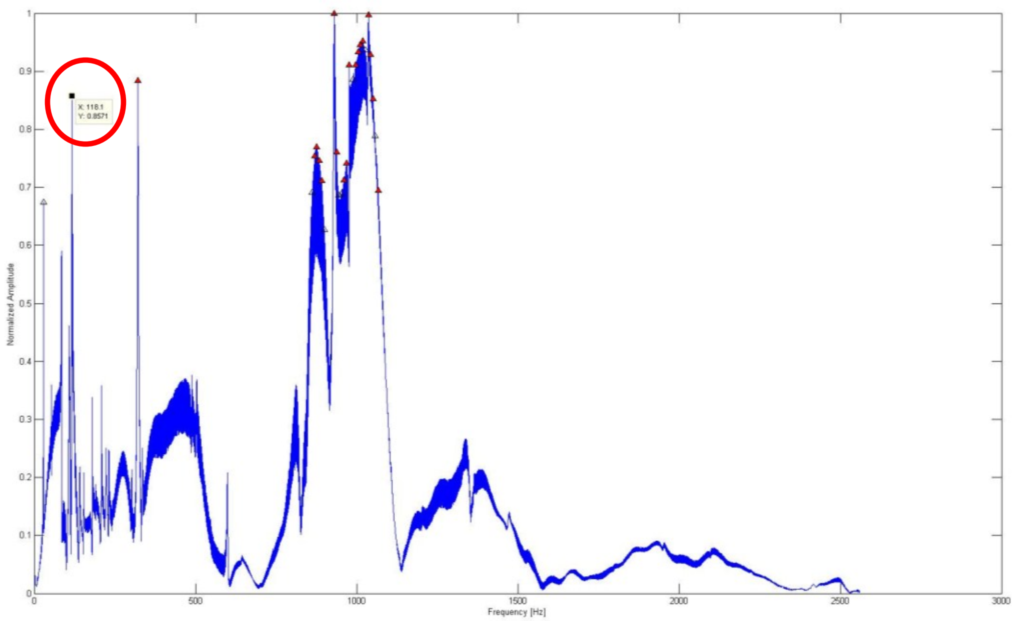

Figure 74 - MATLAB FFT Plot of Benchmark (BH) Specimen: Clamped Boundary Condition
The red circle indicates the first FFT peak, at 118.1Hz

Table 18 - Summary of Natural Frequencies: Clamped Boundary Condition

Sample	Natural Frequency [Hz]	Model	Impact Hammer		IET: Microphone	IET: Laser
			FRF	FFT		
Benchmark Material Samples						
BH	First	210.3	465.2	118.1	836.5	126.4
	Second	1262	825.8	876.3	3638	
	Third	2368	1464	1037		
BC	First	279.5	829.5	84.4	1711.7	128.4
	Second	1140	1406	597.0		1737
	Third	1357	1614			
BF	First	149.1	667.8	70.0	513.6	58.3
	Second	793.0	1745	317	1737	194.8
	Third	798.0		679.7		
Flax Layer Placement Samples						
FP1	First	243.1	934.7	82.5	952.3	94.3
	Second	1038	1424		2664	203.7
	Third	1200		1042		
FP2	First	241.4	924.9	80.0	968.8	100.9
	Second	1030	1870	326.9	3045	
	Third	1193		987.2		
FP3	First	239.7	952.5	82.5	934.5	100.6
	Second	1023	2124	515.0	3245	174.8
	Third	1185		1009		
FP4	First	237.8	879.4	81.3	479.5	95.3
	Second	1015	1577	408.1	2706	
	Third	1177		868.0		
Multiple Flax Layer Samples						
DF1	First	213.6	738.5	95.0	926.5	98.2
	Second	957.1	2116	311.6	2364	
	Third	1059		851.6	3712	
DF2	First	210.3	773.9	77.2	754.9	96.9
	Second	943.3	2109	321.3	966.3	178.6
	Third	1059		805.3	3460	
DF3	First	206.9	802.1	78.8	908.1	94.9
	Second	928.9	2327	320.9	2247	
	Third	1043		980.9	3417	
DF4	First	212.0	809.0	77.8	903.0	95.3
	Second	950.0	2132	335.9	2317	181.0
	Third	1066		904.0	3791	847.2
DF5	First	208.6	806.9	78.1	917.3	99.3
	Second	935.9	2174	333.8		
	Third	1051		958.1	3681	842.8

Table 19 - Summary of Damping Factors (%): Clamped Boundary Condition

Sample	Impact Hammer		IET: Microphone	IET: Laser
	Decay Time (s)	Damping Factor		
Benchmark Material Samples				
BH	0.1525	0.605	2.14	10.33
BC	0.1609	0.957	4.98	8.15
BF	0.0787	0.752	10.10	19.52
Flax Layer Placement Samples				
FP1	0.1641	1.10	1.86	9.16
FP2	0.1279	1.02	1.87	12.46
FP3	0.1410	0.671	1.68	14.58
FP4	0.1424	0.888	2.04	15.13
Multiple Flax Layer Samples				
DF1	0.0395	1.63	9.27	10.41
DF2	0.0961	0.787	1.66	6.99
DF3	0.0623	1.54	3.49	10.10
DF4	0.0656	1.027	2.90	7.84
DF5	0.0779	0.804	2.67	7.20

As is shown in Table 18, there is significant variance in the experimental natural frequencies identified, compared to both the modeled prediction and between methodologies. Due to significant signal noise in the impact FRF responses, the FFT identified natural frequencies are also presented. This comparison highlights the difficulty in identifying the natural frequencies experimentally, as by definition the FRF and FFT natural frequencies should be equivalent as was the case with the free-free boundary condition. This variance in the clamped data will be discussed further in the succeeding section. From inspection of Table 18, the impact hammer:FRF and IET: microphone data did not identify any natural frequencies consistently compared to the model predictions. Additionally, the IET:laser method consistently predicted the first natural frequency only, with subsequent frequencies unidentified due to noise in the signal. Thus for comparison, the experimental first natural frequency of the impact hammer:FFT and IET:laser will be compared to the modeled first natural frequency only. This comparison is shown below in Table 20.

Table 20 - Difference between Experimental First Natural Frequency and Model Prediction

Sample	Impact Hammer: FFT	IET: Laser
Benchmark Material Samples		
BH	43.8%	39.9%
BC	69.8%	54.0%
BF	53.1%	60.9%
Flax Layer Placement Samples		
FP1	66.1%	61.2%
FP2	66.9%	58.2%
FP3	65.6%	58.0%
FP4	65.8%	59.9%
Multiple Flax Layer Samples		
DF1	54.0%	55.5%
DF2	53.9%	63.3%
DF3	54.1%	61.9%
DF4	55.0%	63.3%
DF5	52.4%	62.5%

The damping factor and time to equilibrium for both the free-free boundary condition and the clamped boundary condition from the impact hammer data is shown below in Figure 75.

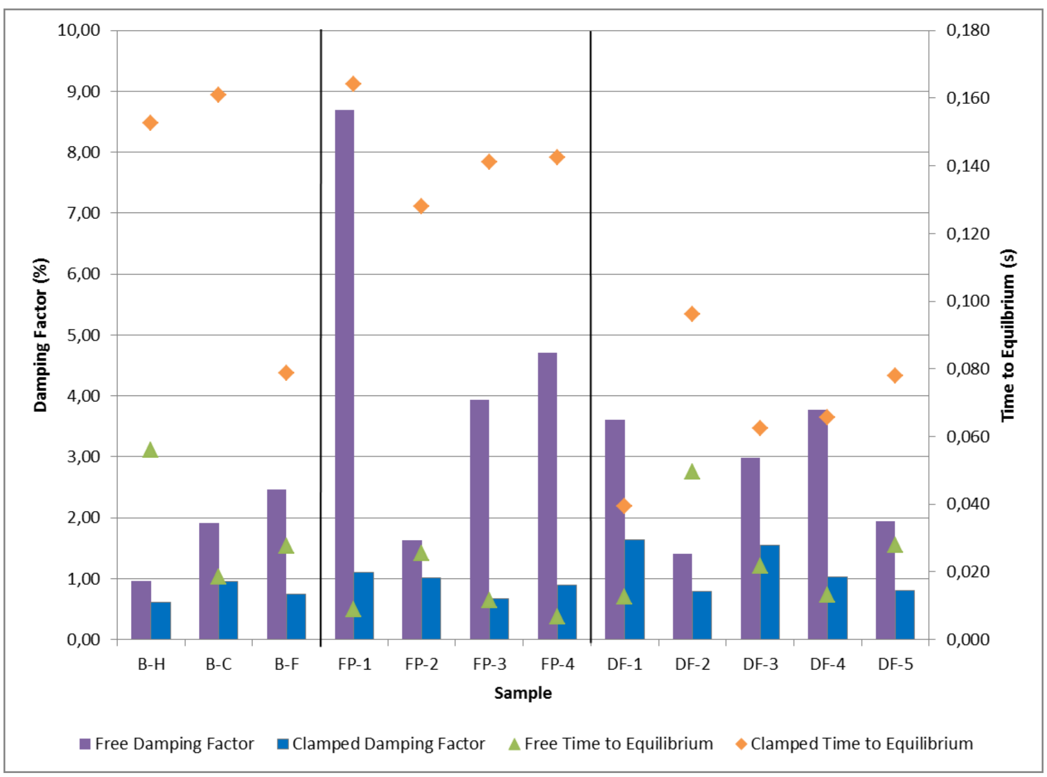

Figure 75 - Damping Factor (%) and Time to Equilibrium for Free-Free and Clamped Boundary Conditions

5.2.5 Dynamic Model Verification

5.2.5.1 Identified Natural Frequencies

The free-free and clamped natural frequencies for the 2D Continuum Shell and 3D Solid Brick models are shown below in Table 21 and Table 22 respectfully.

Table 21 - Free-Free Modeled Natural Frequencies using 2D Continuum Shell and 3D Solid Brick Elements

	First Natural Frequency [Hz]			Second Natural Frequency [Hz]			Third Natural Frequency [Hz]		
Sample	**2D**	**3D**	**Difference**	**2D**	**3D**	**Difference**	**2D**	**3D**	**Difference**
Benchmark Material Samples									
BH	1166	1106	5.2%	1166	1119	4.1%	3072	2781	9.5%
BC	1463	1412	3.4%	1463	1413	3.4%	2147	2146	0.1%
BF	801.6	727.4	9.3%	801.6	727.9	9.2%	1502	1499	0.3%
Flax Layer Placement Samples									
FP1	1279	1191	6.9%	1279	1191	6.8%	1954	1919	1.8%
FP2	1270	1212	4.6%	1270	1213	4.5%	1940	1938	0.1%
FP3	1261	1191	5.6%	1926	1261	34.5%	1926	1920	0.3%
FP4	1252	1085	13.3%	1252	1086	13.3%	1910	1842	3.6%
Multiple Flax Layer Samples									
DF1	1130	1045	7.5%	1130	1046	7.5%	1802	1776	1.4%
DF2	1113	1045	6.1%	1113	1046	6.0%	1776	1777	0.0%
DF3	1095	905	17.4%	1095	906	17.3%	1749	1681	3.9%
DF4	1121	1058	5.7%	1121	1058	5.6%	1789	1786	0.1%
DF5	1104	991.0	10.2%	1104	991.5	10.2%	1762	1739	1.3%

Table 22 - Clamped Modeled Natural Frequencies using 2D Continuum Shell and 3D Solid Brick Elements

	First Natural Frequency [Hz]			Second Natural Frequency [Hz]			Third Natural Frequency [Hz]		
Sample	**2D**	**3D**	**Difference**	**2D**	**3D**	**Difference**	**2D**	**3D**	**Difference**
Benchmark Material Samples									
BH	210.3	200.9	4.5%	210.3	201.6	4.1%	1262	1152	8.7%
BC	279.5	266.1	4.8%	279.5	266.2	4.7%	1140	1138	0.2%
BF	149.1	132.0	11.5%	149.1	132.1	11.4%	793.0	727.4	8.3%
Flax Layer Placement Samples									
FP1	243.1	222.2	8.6%	243.1	222.3	8.6%	1038	1018	2.0%
FP2	241.4	226.4	6.2%	241.4	226.5	6.2%	1030	1028	0.2%
FP3	239.7	222.6	7.1%	239.7	222.7	7.1%	1023	1018	0.4%
FP4	237.8	203.0	14.7%	237.8	203.1	14.6%	1015	978	3.6%
Multiple Flax Layer Samples									
DF1	213.6	193.4	9.5%	213.6	193.5	9.4%	957.1	941.7	1.6%
DF2	210.3	193.6	8.0%	210.3	193.7	7.9%	943.3	942.2	0.1%
DF3	206.7	167.7	18.9%	206.7	167.8	18.9%	928.9	891.8	4.0%
DF4	212.0	195.9	7.6%	212.0	196.0	7.5%	950.0	946.9	0.3%
DF5	208.6	183.7	11.9%	208.6	183.8	11.9%	935.9	922.7	1.4%

The mode shapes for the 3D Solid Brick model for both the free-free and clamped boundary conditions were observed to be identical to those identified in the 2D Continuum Shell model, shown in Figure 64 and Figure 65 respectfully.

5.2.5.2 Strain Energy Distribution

From the initial results of the strain energy distribution, **Element 70** (Figure 55) was chosen for further analysis due to the consistently high strain energy present for all laminates, boundary conditions, and natural frequencies. The strain energy densities at the midsection and top of each ply were compared to identify potential transitions that may lead to delamination and damping mechanisms. The total through-thickness strain energy magnitudes for all laminates in the free-free and clamped boundary conditions for the first three natural frequencies are shown below in Figure 76 - Figure 81. For comparison, the free-free and clamped boundary conditions for each natural frequency are side-by-side.

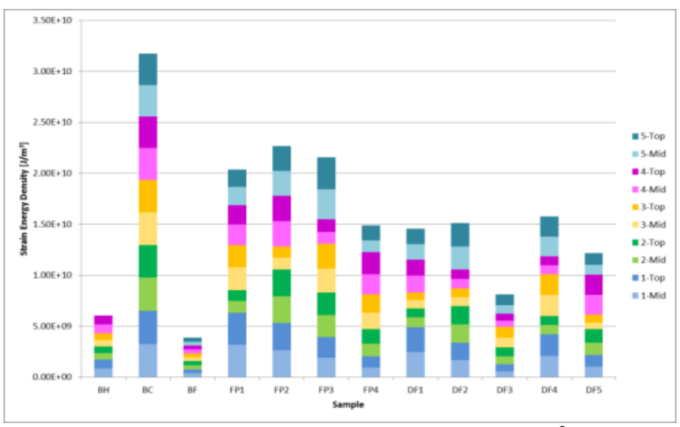

Figure 76 – Accumulative Strain Energy Density [J/m^3]: Free-Free, First Natural Frequency

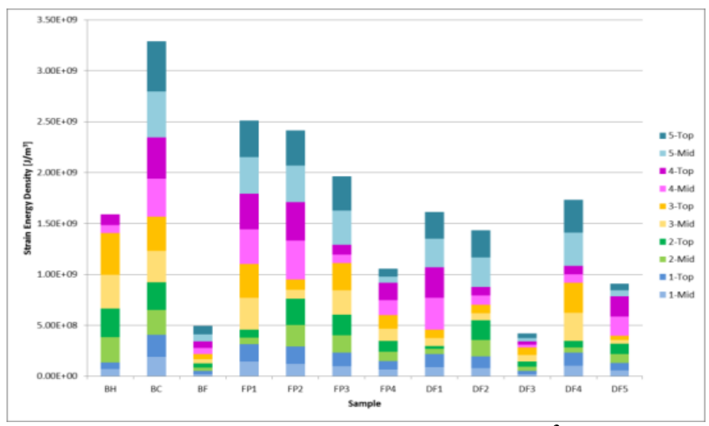

Figure 77 - Accumulative Strain Energy Density [J/m^3]: Clamped, First Natural Frequency

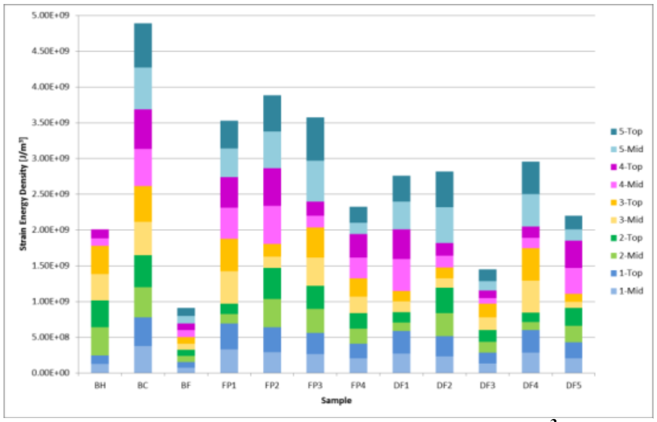

Figure 78 - Accumulative Strain Energy Density [J/m^3]: Free-Free, Second Natural Frequency

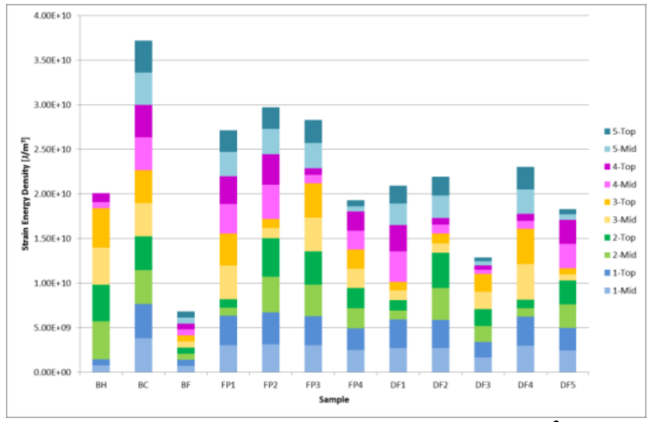

Figure 79 - Accumulative Strain Energy Density [J/m^3]: Clamped, Second Natural Frequency

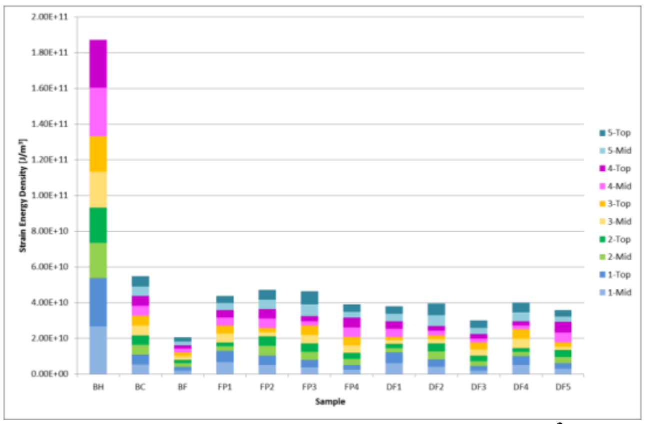

Figure 80 - Accumulative Strain Energy Density [J/m^3]: Free-Free, Third Natural Frequency

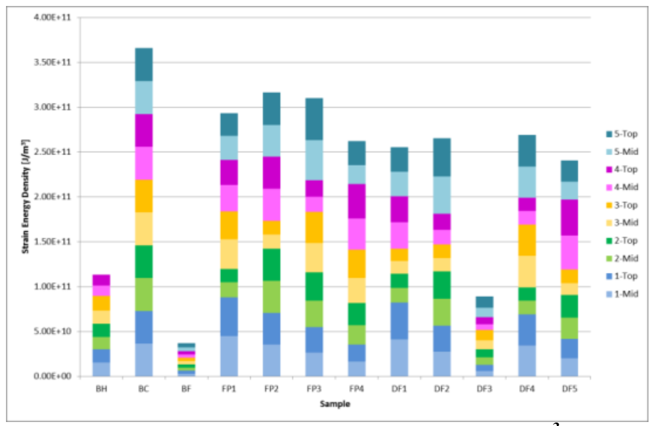

Figure 81 - Accumulative Strain Energy Density [J/m^3]: Clamped, Third Natural Frequency

5.2.5.2.1 Effect of Boundary Condition

As is shown above in Section 5.2.5.2, the magnitude of strain energy density is significantly different for the two boundary conditions. Therefore, to compare the relative distribution of the strain energy density and effect of boundary condition, the strain energy density of each sample was normalized to its own maximum. As the hybrid laminates are of primary interest, only the flax specimen placement (FP) and multiple flax layer (DF) groups are illustrated. These results are shown below in Figure 82 - Figure 84.

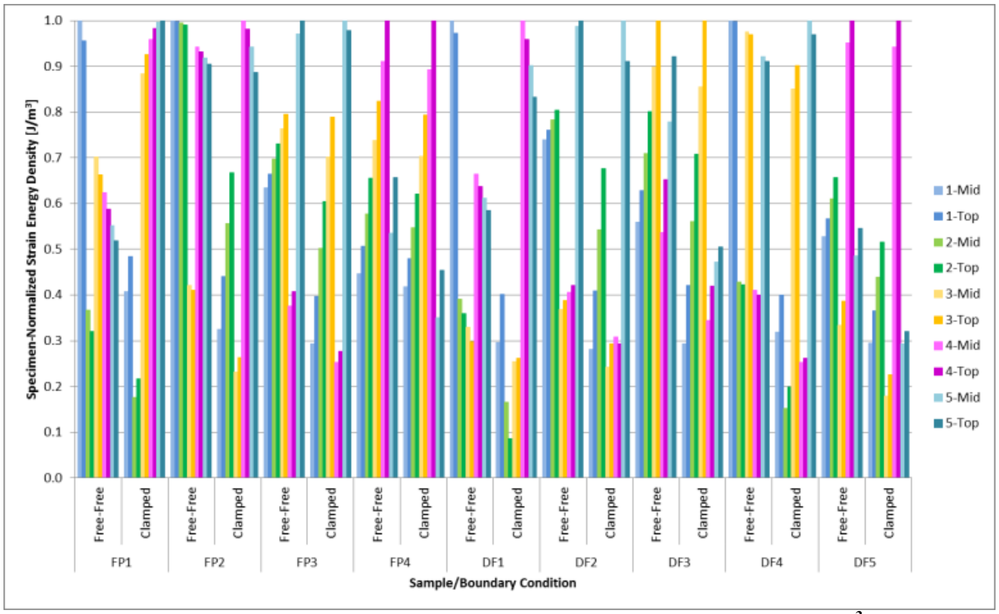

Figure 82 - Free-Free vs. Clamped: Through Thickness Strain Energy Density [J/m^3] Distributions: First Natural Frequency

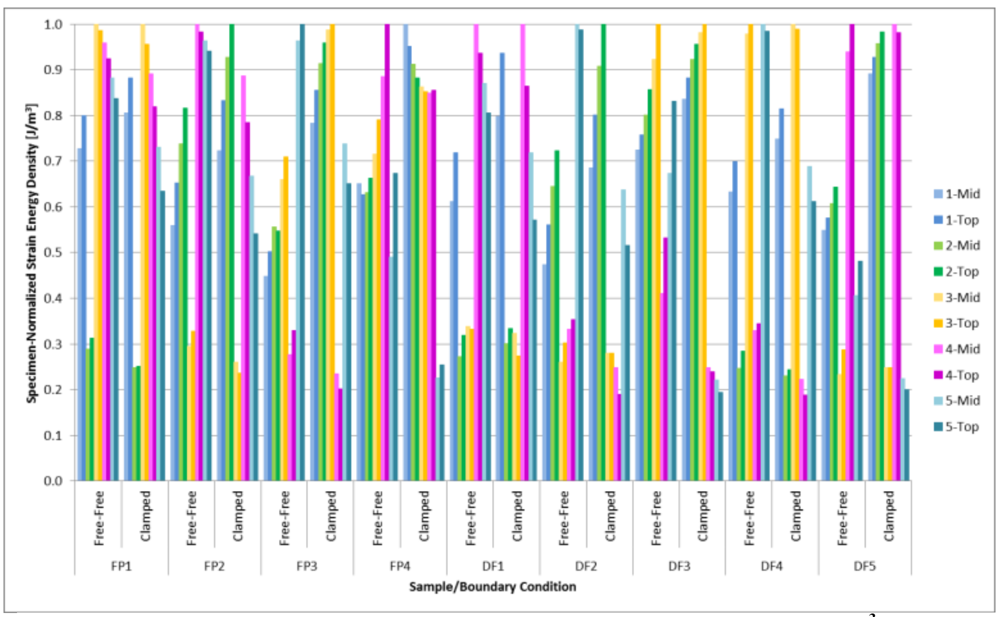

Figure 83 - Free-Free vs. Clamped: Through Thickness Strain Energy Density [J/m^3] Distributions: Second Natural Frequency

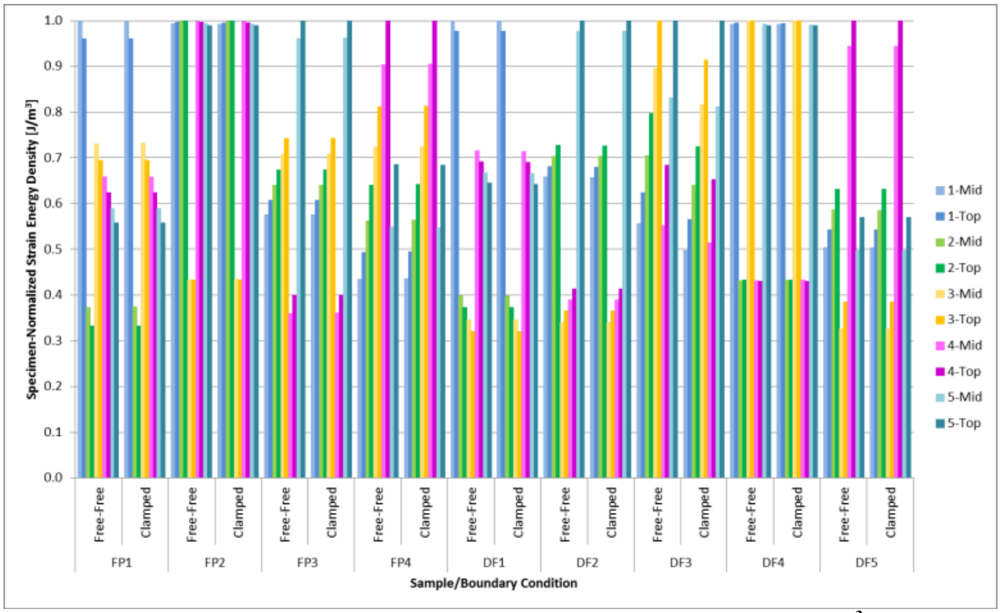

Figure 84 - Free-Free vs. Clamped: Through Thickness Strain Energy Density [J/m^3] Distributions: Third Natural Frequency

5.3 Discussion

5.3.1 Microscopy

The microscopy laminate quality assessment indicated that a high quality laminate composed of hybrid carbon and flax reinforcement composites was achieved. The average fiber volume fraction for the laminate was 37-40%, regardless of the layup order or number of flax layers (54). This is comparable to benchmark flax material fiber volume fraction of 40%. The microscopic images indicate that the laminate cross-section have minimum voids and good consolidation. Some care must be taken when interpreting the results, as the samples were prepared first by cutting and then by wet polishing. As previously discussed, this may have induced porosities or interlaminar cracks that may not be present in-situ. Additionally, these cross-sections are only from one sample location. Ideally, a non-destructive analysis of the laminate would be performed to give a better indication of the component actual quality and potential effects on the tested performance.

5.3.2 Dynamic Testing

5.3.2.1 Comparison of Experimental Technique

Experimental dynamic testing often results in high variability due to study design. Experimental design parameters which may affect data quality include measurement technique sensitivity, signal processing, impedance of vibration from applied boundary conditions, and in the case of the impact hammer, damping effects of the accelerometers. To determine the most appropriate experimental method for this investigation, three different techniques were used to assess the dynamic behaviour of the hybrid composites: the impact hammer method and the IET method using both a microphone and laser to measure the sample response. From these methods, the first three natural frequencies of the samples were extracted and compared to the ABAQUS predicted model behaviour. All three experimental methods did not measure the ABAQUS predicted third natural frequency, corresponding to a mode shape of rotational expansion along the longitudinal axis. Additionally, in ABAQUS the first and second natural frequency occur simultaneously in the free-free boundary condition, with deflections in the y and z directions. As Hay et. al. hypothesized, the multi-directional deformation may have been dampened in one direction due to the rigid body motion of the specimen subsequent to impulse. The nature of this deformation may also have been susceptible to damping due to the free-free boundary supports (54). Vanwalleghem et. al. (2014) found in their investigation regarding noise contributions to experimental vibration testing that misplacement of supports may result up to 82% error in the first natural frequency (55).

As was previously observed significant difficulty in obtaining a clean signal and data set was experienced with the clamped boundary condition. In theory, the cylinder end is restrained in all six degrees of freedom. However, this is not possible to achieve experimentally (55). Although vibration experiments are often performed with a cantilever beam, any method of clamping the specimen involving bolted connections and a specimen grip system may have significant discrepancy in measured behaviour with theoretical behaviour due to vibration and dampening of the grip system (55). Bolt vibration, micro-slipping between the specimen and grip interface, as well as weight of the specimen in relation to the gripping apparatus may result in experimental errors (55). Thus, for the clamped boundary condition the resulting dynamic behaviour may not be representative of material behaviour but rather structure (system) behaviour. Due to these significant experimental limitations, Vanwalleghem et. al. (2014) recommend to experimentally determine dynamic behaviour of materials using free-free boundary condition (55).

In addition to the above experimental difficulties associated with a clamped boundary condition, it was observed during testing that the stem fixture used to clamp the cylinder was not entirely encased in all directions. There was a small gap in the y-direction, due to the stem clamp design. Although this replicates the handlebar condition and thus structure response, it is not desirable for a material characteristic study as vibration may resonate in the gaps, contributing to potential sources of error as the experimental set-up was not an ideally clamped boundary condition. Thus, for the clamped boundary condition, model predictions may be the best method to identify the material natural frequencies of the tested geometry, with verification of approximate structure response experimentally tested using either the impact hammer:FFT technique or the IET:laser technique, as neither technique significantly improved the experimental discrepancy.

Table 16 illustrates the difference between predicted ABAQUS modeled natural frequencies and experimental values for the free-free boundary condition. For all hybrid laminates, the average difference for the first natural frequency for the impact hammer was 6%-15%, and 2-13% for the IET methods. The experimental second natural frequency had much higher variation, ranging from 0.1-34% for the impact hammer and 2-52% for the IET methods. This indicates that the first natural frequency can be experimentally validated, with acceptable error when compared to the theoretical model results. The higher degree of variation in the experimental second natural frequency prediction may be a systematic error of the experimental methodologies, with increasing difficulty in obtaining clean signals at higher frequencies. At higher frequencies, the variance in the laminate including thickness changes and/or potential misalignment of the plies may have a greater impact on experimental results. Additionally, the experimental free-free supports were not changed and were placed at the node locations identified for the first natural frequency. Therefore the higher frequency response may have been significantly dampened due to the interaction between the sample and the supports.

Although the variation in the IET technique for the first natural frequency is slightly less than that of the impact hammer technique, the variation for the second natural frequency is much greater. This is most likely a function of noise induced in the system at the measurement point. The impact hammer method used accelerometers directly attached to the specimens for vibration measurement. Although the mass of the accelerometer may have changed the dynamic response marginally, the apparatus was set up with one accelerometer at either end to balance the additional mass, and care was taken to ensure that the lead wires were loose, to minimize the damping effect of restraining wires (55). In theory, non-contact measurement systems such as microphone and laser should result in much higher repeatability and reliability of measurements. However, non-contact measurement systems are also highly susceptible to noise contributions from the surrounding environment. For the microphone measurements, it was observed during data collection that the ambient white noise had a significant impact on the measured results. This white noise may have multiple frequency components, which will directly impact the data collected. For the laser measurements, it was observed that the laser had difficulty maintaining the focal point on the specimen surface due to the convex surface and rigid body motion in the free-free boundary condition. This loss of focal point required multiple impulse trials for the laser to record the vibration displacement and process results. This rigid body movement may have also affected the accuracy of the results. Therefore, for the hollow cylinder specimens, the most repeatable and reliable method of dynamic analysis measurement was by using the impact hammer method with accelerometers placed at either end of the specimen, with loose lead wires to minimize the impedance on the specimen by the accelerometer apparatus. All succeeding discussion will thus focus on results obtained from the impact hammer method.

5.3.2.2 Free-Free Dynamic Behaviour

Comparing the experimental first natural frequencies of the hybrid laminates, we can observe the following trends. As is shown in Table 16, the unidirectional carbon fiber has the highest natural frequency, and is one order of magnitude greater than both the benchmark handlebar design as well as the unidirectional flax sample (54). The unidirectional flax sample has the lowest natural frequency of all benchmark samples, approximately 100Hz below that of the benchmark handlebar design. Natural frequency of the hybrid composite follows the rule of mixtures of material behaviour, with the natural frequency decreasing as the flax material moves to the outermost ply position(s) (54). All hybrid laminate frequencies are greater than the benchmark design, as well as the estimated human perception threshold of 100Hz. Thus, hybrid laminate configuration can be optimized for other design parameters such as damping and stiffness, with minimal effect on natural frequency.

The damping factor is an indication of how quickly the oscillating system returns to its state of equilibrium after stimulus (54). The optimally damped system is critically damped, as shown in Figure 4. From Table 17, the unidirectional flax material had a higher damping factor than the unidirectional carbon fiber, as expected (54). All laminates have superior damping characteristics compared to the benchmark handlebar, as is shown in Table 17 and Figure 75.

From the flax layer placement samples, it can be observed that damping behaviour improves as the number of consecutive carbon fiber layers increases. Comparing the results of FP3 ([C_3/F/C]) and FP1([C/F/C_3]), both of which have a carbon fiber grouping of three layers, it can be observed that the damping ratio and time to equilibrium can be further optimized with the flax layer closer to the innermost layer. From the multiple flax layers sample group, we can observe significant changes in damping behaviour based on laminate configuration. All samples have lower damping ratios compared to the flax placement group, contrary to what would be expected if only the rule of mixtures applied. However, the flax laminate samples that are grouped together behave with the same damping performance patterns as identified with a single flax layer. Comparing DF4 ([C/F/C/F/C]) to DF1 ([C/F/C_3]), DF4 has a slightly greater damping ratio and equivalent time to equilibrium, with no significant difference in natural frequency. Therefore, it can be inferred that hybrid laminates with one inner carbon layer will behave in the same manner with regards to damping, regardless of flax position. This behaviour is not observed with two inner carbon layers, as illustrated when comparing DF2 ([C_2/F_2/C]) with its counterpart DF5 ([C_2/F/C/F]): the damping characteristics are significantly improved with the flax fiber layers dispersed through the rest of the laminate. Finally, comparing all the sample sets, to optimize the damping behaviour of the hollow cylinder, the laminate with the smallest time to equilibrium and greatest damping factor is [C/F/C_3], with a damping ratio of 8.7% and time to equilibrium of 0.009s (54) in the free-free boundary condition.

5.3.2.3 Clamped Dynamic Behaviour

Comparing the identified theoretical natural frequencies of the hybrid laminates in the clamped condition we can observe the following trends. All samples had significantly lower first natural frequencies compared to the free-free condition, although none were below the human sensitivity threshold. As is shown in Table 18, the unidirectional carbon fiber had a higher natural frequency than the flax material, which was expected due to the damping behaviour of the flax material. There is no significant inter-group change in the hybrid laminate natural frequencies. Thus, the natural frequency of the hybrid composite follows the rule of mixtures of materials, and is independent on the laminate sequence.

From Table 19, contrary to the results obtained in the free-free condition, the unidirectional carbon fiber had a greater damping factor than the unidirectional flax material, and over double the time to equilibrium. From a human perception perspective, although it has a higher damping factor, the unidirectional flax may have superior damping characteristics based on the duration of perceived discomfort due to vibration. As in the free-free condition, the benchmark handlebar laminate had the lowest damping factor of all samples, indicating that the laminate can be optimized for damping.

From the flax layer placement sample group, it can be observed that for the clamped boundary condition the inner unidirectional carbon layers must not exceed two for optimal damping. Although the laminates FP1 ([$C/F/C_3$]) and FP2 ([$C_2/F/C_2$]) have similar damping factors, the time to equilibrium is shortest with the balanced hybrid laminate of [$C_2/F/C_2$]. Thus, the overall superior damping behaviour is exhibited with the balanced hybrid laminate within the flax layer placement group. From the multiple flax layer sample group, we can observe significant changes in damping behaviour based on the laminate configurations. Contrary to the free-free behaviour, the patterns observed in the flax layer placement sample group are not observed in the multiple flax layer sample group, indicating that the flax-specific mechanisms of damping are significant in the clamped condition. In the multiple flax layer group, the laminate with the largest damping factor and smallest time to equilibrium is DF1 ([$C/F_2/C_2$]), with the worst damping behaviour exhibited by DF2 ([$C_2/F_2/C$]). If the observations of the flax layer placement sample group were valid for the multiple flax layers, we would expect DF2 to have the best damping behaviour, marginally superior to DF1. However, as is observed in Table 19, DF1 has a smaller time to equilibrium by a factor of three and a greater damping factor by a factor of two when compared to DF2. Also significant in the multiple flax layer samples is laminate configuration. When comparing DF1 to the equivalent laminate DF4 ([C/F/C/F/C]) we can observe that when the flax layers are grouped together as in DF1, the damping factor is greater and the time to equilibrium is decreased by a factor of two. Considering DF2 and the equivalent laminate DF5 ([C_2/F/C/F]) the effect is converse to DF1 and DF4, with DF5 having a marginally greater damping factor and a lower time to equilibrium. This most likely is due to the outer flax layer, as we can see when comparing DF2 and DF3 ([C_3/F_2]) that the addition of the outer flax layer(s) results in an increase in damping factor and decrease in time to equilibrium. This behaviour indicates that the dynamic characteristics are highly dependent on laminate configuration, with the mechanism of damping critical and the flax-specific damping characteristics of greater importance in the structural dynamic behaviour with the clamped boundary condition. Finally, considering all hybrid laminates in the clamped boundary condition, optimal structural damping characteristics is achieved with the laminate configuration of [C/F_2/C_2] with a damping factor of 1.63% and a time to equilibrium of 0.04s.

5.3.2.4 Effect of Boundary Condition on Design Application

5.3.2.4.1 Comparison of Natural Frequency and Damping Behaviour

The boundary condition has a significant impact on the damping behaviour of the hybrid composites, as was shown above. With respect to the natural frequencies, the first natural frequency significantly decreased in the clamped boundary condition. The minor changes in natural frequency observed in the free-free condition associated with flax position were not observed with the clamped boundary condition. Instead, the natural frequencies followed the rule of mixtures, independent of flax position. This behaviour allows for the composite to be optimized for strength and/or stiffness without significantly affecting the natural frequency range of the composite.

The damping behaviour significantly changed from the free-free to the clamped boundary condition, as is illustrated in Figure 75. In the clamped boundary condition the damping factor was marginally greater for the unidirectional carbon fiber when compared to the flax material, contrary to results obtained in the free-free condition. The patterns of damping improvement were converse for the clamped boundary condition in the hybrid composites. If the free-free behaviour was used to optimize the damping behaviour, the optimal laminate was FP1 [$C/F/C_3$], with the greatest damping factor and shortest time to equilibrium. However, when considering the clamped boundary condition, the optimal laminate is DF1 [$C/F_2/C_2$]. This has a significant impact on the use of the laminates for design purposes, and also illustrates the difference in the damping mechanisms for each boundary condition of the hybrid laminates.

As previously discussed, natural fibers including flax are thought to be advantageous in damping applications due to their unique microstructure that allows for additional energy dissipation. Composites in general have superior damping compared to metals as they allow for energy dissipation via matrix cracking, fiber/matrix disbonding, and interlaminar shear. The clamped boundary dynamic characteristics representing the structural behaviour indicate that the flax-specific damping mechanisms are more significant than in free-free, with hybrids with multiple flax layers displaying optimal damping performance. One explanation of this change could be the increase in significance in out-of-plane shear in a cantilever structure. In isotropic materials such as metals, the out-of-plane shear is equivalent to the in-plane shear properties, and thus no difference in behaviour is expected. With anisotropic materials such as composites, and more significantly with natural fibers and hybrid composites, the shear behaviour is directional, and thus the out-of-plane shear may be considered significant when explaining the mechanisms behind the clamped dynamic properties.

With hybrid composites, the interface geometry between the carbon/fiber reinforcement layers may also be significant. From microscopy, it is evident that the much thinner unidirectional carbon fiber layers are slightly warped in the out-of-plane direction due to the presence of the larger flax bundles. This is shown in Figure 60, with the unidirectional carbon fiber layer adjacent to the flax layer displaying a ‘wave’ pattern due to the influence of the flax fiber bundles. The out-of-plane warping of the carbon fiber layers may explain the significance of the laminate configuration when the ratio of carbon fiber and flax is constant.

5.3.2.4.2 Comparison of Natural Frequency and Human Sensitivity Thresholds

Although the clamped boundary condition resulted in a significant decrease in the first natural frequency, all are over the human sensitivity range of 8-100Hz, and thus this parameter does not need to be optimized. However, this model neglects the influence of additional handlebar components, such as brake and shifter levers, which are commonly clamped onto the handlebar. Additionally, when taking into consideration the damping effect of the cyclist at the hand/handlebar interface, based on the behavioural trend of the change in natural frequency from free-free to clamped, we can anticipate a further reduction in the handlebar natural frequency, which will most likely fall within the human sensitivity threshold. Therefore, the natural frequency of the assembled structure should be taken into consideration when designing the handlebar laminate, with the anticipation that with the inclusion of the additional components and influence of the hand/handlebar contact the natural frequency of the structure will further decrease. Thus damping behaviour should be considered in the design, with optimization in the appropriate boundary condition. This hypothesis indicates that the laminate DF1 with its superior structural damping characteristics in the clamped boundary condition would result in the greatest improvement in perceived human discomfort. This laminate does not represent the optimal damping characteristics in free-free, further illustrating the importance of accurate modeling of boundary conditions for material characterization for design applications.

From the above discussion and analysis, for the boundary condition most representative of the application of the handlebar, the optimal dynamic behaviour when considering human discomfort is DF1 ([C/F_2/C_3]). As modeled, this laminate configuration satisfies the flexural strength requirement of EN 14766, while showing superior damping characteristics with a lower natural frequency and time to equilibrium with a greater damping factor when compared to the benchmark laminate.

5.3.2.5 Dynamic Model Verification

5.3.2.5.1 Identified Natural Frequencies

From Table 21 and Table 22, the importance of proper model construction and element identification is illustrated. For both models, care was taken to ensure that the material direction was consistent, as well as the geometry specifications including through-thickness. Therefore, the differences in predicted natural frequencies can be attributed to the type of element used and meshing operations for the 2D and 3D models.

For the free-free boundary condition, the difference between the two models ranged from 6-17% for the first natural frequency, 3-35% for the second, and 0.03-9% for the third. The variation may be a function of the mode shape observed. As the mode shapes were identical for both models, this may indicate the validity of the assumption of negligible shear in the thickness direction inherent in the 2D model. The clamped boundary condition had similar variations: from 5%-19% for the first and second natural frequencies, and from 0.1-9% for the third. Due to the thickness dimension in the 3D model the boundary condition is specified slightly differently, with the zero degree of freedom boundary condition applied to the outer surface only, allowing free movement for the inner surface of the hollow cylinder. In the 2D model, this boundary condition is applied for the entire thickness of the cross section, so in theory the inner surface is also restricted from movement. For rigid structures in static flexural loading this should not make a difference. However, for dynamic analysis and resonance, this variation may be significant in determining the natural frequencies and nuances of the mode shapes. For both boundary conditions, the 3D theoretical natural frequencies are marginally lower than that of the 2D natural frequencies, which results in closer agreement with the experimentally determined natural frequencies. Although the difference is small, this may indicate that for this particular application, the plane-strain assumption for thin walled structures may not be valid.

5.3.2.6 Strain Energy Distribution

Interpreting the results of the strain energy density through the thickness of the laminate is complicated and depends on multiple variables. As is shown in Figure 77 - Figure 84, the strain energy distribution depends not only on the laminate sequence, but also on the boundary condition and resonant mode shape. As the experimental method was a random excitation, all natural frequencies and associated mode shapes were present during the excitation process, making the resultant deflection a weighted ratio of all mode shapes present. Therefore, general trends in behaviour will be discussed below, with a focus on the samples that exhibited the best damping behaviour in the free-free and clamped boundary conditions.

5.3.2.6.1 Effect of Boundary Condition

As was observed experimentally, the boundary condition has a significant impact on the strain energy density magnitude and through-thickness distribution. First, as is shown in Figure 76 - Figure 80 the clamped boundary condition results in strain energy magnitudes one order lower than free-free in the first natural frequency and one order higher in the second. The third natural frequency has approximately equivalent strain energy magnitudes across all samples for the clamped condition, whereas in the free-free condition the benchmark design had almost one order of magnitude greater total strain energy density. Both the free-free and clamped boundary conditions exhibit the same trends with regards to strain energy magnitude: the unidirectional carbon fiber has the highest magnitude, the unidirectional flax the lowest, and the hybrid laminates with flax layer(s) at the outermost position(s) had the lowest strain energy density magnitudes. This behaviour is exaggerated for the samples with multiple flax layers in the second natural frequency for the clamped boundary condition.

To further examine the differences in the strain energy distribution through the thickness of the samples for the free-free and clamped conditions, the samples were normalized to their own maximum and plotted together, as shown in Figure 82 - Figure 84. For the first natural frequency, from Figure 82 we can observe that for the samples with outer flax layer(s) there is no significant difference in strain energy distribution from the free-free and clamped conditions. For hybrid laminates with one inner carbon layer or a single flax layer in the Ply-2 position, with the application of the clamped boundary condition the strain energy distribution is inverted, resulting in a change in local maxima difference from the inner carbon/flax interface (free-free) to outer carbon/flax interface (clamped).

The relative behaviour changes for the second natural frequency, as shown in Figure 83. For most hybrid laminates, the clamped boundary condition resulted in strain energy density increase for Ply 1-2, and decrease for Ply 4-5, with Ply 3 acting as the local maximum. This observation is unique to the second natural frequency and clamped boundary condition. Figure 84 indicates that there is no significant change in the strain energy distribution through the thickness of the laminates for the third natural frequency. Therefore, it is most likely that the third natural frequency was not a dominate experimental mode shape, and the damping behaviour changes between the free-free and clamped boundary conditions are most likely due to the changes observed in the first and second natural frequencies.

5.3.2.6.2 Strain Energy Distribution Change of Superior Clamped Damping Specimen

From the experimental data, the optimal damping for the free-free condition was with FP1 ([$C/F/C_3$]), and for the clamped boundary condition was DF1 ([$C/F_2/C_2$]). With respect to DF1, in the clamped boundary condition the strain energy density had the greatest relative strain energy difference between the carbon and flax layers. The overall magnitude of the strain energy density was not the greatest of the hybrids, including the other laminates with two flax layers. This result is interesting, as it contradicts the behaviour hypothesized by van Vuure et. al as the samples with the greatest overall strain energy density magnitude did not exhibit the best damping behaviour (29). Rather, it is the relative net difference between the flax layer and carbon layer as well as position of flax layer which appears to be the critical component to predict damping from strain energy density. Also important is the thickness of the flax layer: as is shown when comparing the damping behaviour of DF1 and DF4 ([C/F/C/F/C]) (Figure 75) although they both exhibit high relative differences in strain energy density between the flax and carbon layers, DF1 has superior damping performance, with the flax layers grouped together. In this regard, the results agree with that predicted by van Vuure et. al., as DF1 has the thickest flax layer located closest to the inner surface (29). This behaviour also explains the superior experimental damping performance of DF1 compared to DF3 ([C_3/F_2]). Both damping factors were approximately equivalent, however DF1 had a shorter time to equilibrium, and thus superior damping characteristics. From the strain energy densities, DF3 has significantly lower magnitude of strain energy density, and the compliant flax layers are located furthest from the inner surface; both factors which were considered detrimental to damping performance by van Vuure et. al. (29) .

In general, when comparing the relative strain energy distributions for all samples from the free-free to the clamped conditions (Figure 82 - Figure 84), all specimens show an increase in the relative difference between the flax layers and carbon layers. When the change in relative ranking of damping from free-free to clamped is considered, it is the samples with the flax layer(s) closet to the inner surface with the maximum net difference of strain energy density at the flax/carbon interface that exhibit superior structural damping behaviour. With the addition of the clamped boundary condition, the thickness of the flax layer at the closet location to the inner surface significantly improves the damping characteristics, as is illustrated by the behaviour of FP1 and DF1, the superior laminate configurations in free-free and clamped respectfully. Interestingly, none of the best damping behaviour samples had corresponding high total strain energy densities. Therefore, the contributing factor of the strain energy density to the damping behaviour is not the overall magnitude, but rather the relative distribution within the sample. This indicates that the primary mechanism of damping is most likely interlaminar strain, with effects from flax-specific damping characteristics increasing as the thickness of the flax layer increases in the clamped boundary condition.

5.3.3 Limitations

With regards to the ABAQUS modeling and results, one significant limitation is the material property assumptions that were required to run the analysis. Experimental data was used wherever possible, but as is shown in Table 11, significant assumptions were made for all other properties. As this is a systematic error, all inter-model comparisons of the various hybrid laminates are still applicable. The comparison between the model and the experimental values however may be impacted, depending on the variation of the assumptions to the actual values. This is a frequent problem when modeling composite behaviour, and without a standard material database of empirical results, the assumptions used in this study are the best estimations of property data available.

With regard to the experimental dynamic procedure, only one specimen was tested for each boundary condition, due to time constraints with sample manufacturing. Thus the standard deviation of the analyzed dynamic properties is unknown. For a more accurate representation of the behaviour, a sample set of five or more should be used and re-tested. This would give an indication of inter-specimen variability as well as the average dynamic characteristics of each hybrid laminate.

Also with regards to the dynamic testing, acoustic excitation was unsuccessful due to equipment difficulties and may have also been impacted by environmental white noise. Thus, for all tests, specific excitation frequencies could not be applied, with all natural frequencies of the structure were excited instantaneously via impact. This makes the comparison between the modeled behaviour and experimental result more difficult, as the modeled behaviour is natural frequency specific. The anticipated mode shapes for each natural frequency changes and with it the node and anti-node locations. With multiple natural frequencies simultaneously excited, those with node locations not in the location of the supports may have been dampened by the supports, as Vanwalleghem et. al. (2014) suggests (55). To improve the experimental data obtained, acoustic excitation in a sound-proof environment should be attempted. An acoustic 'sweep' of the sample could first be performed to identify the experimental natural frequencies. Then, the acoustic loudspeaker could be tuned to emit a sinusoidal signal at each identified frequency, with the resulting acceleration/displacement recorded. This would give frequency-specific damping data, and would further our understanding of the correlation between the experimental and modeled behaviour, and may result in a greater agreement between the two methods.

Finally with regards to the dynamic testing, multiple sensors should be used to measure the specimen response, positioned in all three planes. This is especially important for the test method described above, where each natural frequency is isolated and recorded. The ABAQUS model indicates that for the free-free condition the first two natural frequencies occur simultaneously, with displacements in two separate planes. This was not observed during this test, most likely due to the excitation method. If each individual natural frequency was isolated and tested separately, with multi-directional sensor measurements the cross-talk or effect of the mode shape in the anticipated plane to the displacement could be observed in all other planes. This may be valuable information when considering design improvements, as it has been shown that the human body is sensitive to vibrations occurring in the vertical plane. Thus, if as in the ABAQUS model the two natural frequencies occur simultaneously, from a design standpoint, the superior hybrid laminate would be the one with the greater damping factor in the natural frequency correlating to the mode shape in the plane of greatest sensitivity.

The modeled behaviour of the through-thickness strain energy density is a very brief introduction and focuses only on one element for the entire structure. As it was determined that the mode shape is significant when determining the trends in strain energy density, additional analysis is required to further understand the relationship between strain energy density and holistic damping behaviour of the laminates. Additionally, for correlations between experimental and modeled behaviour, experimental data isolating specific natural frequencies and associated damping behaviour would be beneficial when determining predominate damping mechanisms illustrated through the through-thickness strain energy density behaviour. With natural frequency specific experimental testing, the focus of this model behaviour and results could begin with the critical natural frequency based on the mode shape plane and human sensitivity. By correlating isolated natural frequency damping behaviour and through-thickness strain energy density patterns, one could draw conclusions as to what damping behaviour of the laminate is dominate for each natural frequency and mode shape.

6 Phase 3: Design of Demonstration Bicycle Handlebar

6.1 Methodology

6.1.1 Model Verification of Handlebar Design Properties

Subsequent to the experimental testing and analysis of the hollow cylinder specimens, the experimental hybrid laminates were modeled as in Section 5.1.2. The hybrid laminates were analyzed to ensure that the chosen designs satisfied the design criterion and the natural frequencies of the modeled handlebar and the experimental clamped hollow cylinder were compared. To further refine the developed model, the following changes were made:

1) *Change in ply-drop off strategy*: To eliminate stress risers at geometry changes, the ply-drop off schematic was refined so that ply drop off did not correspond to a geometry change. A third transition area was also added after the final change in diameter so only one ply was removed at a time. This is shown below in Figure 85, with the number of plies and schematic of ply layup identified.
2) *Assigned material direction:* Due to cross-section symmetry, it was initially assumed that only the longitudinal direction (1-axis) was critical in the model. As was shown with the 3D Solid Brick model, the 2-axis and 3-axis are also critical when determining the handlebar performance. Thus, the material direction of the handlebar was changed to agree with that of the 3D Solid Brick cylinder model, as shown below in Figure 86.
3) *Change in mesh size and advancing front:* The refined ply drop-off strategy resulted singularities at specific elements that did not correlate to a real stress riser. Thus, the number of elements was revised to 50 370 elements, and the advancing mesh schematic was changed from a free mesh generation with no restrictions to a free mesh generation advancing on the medial axis to allow for complete mesh convergence over the complicated geometry.

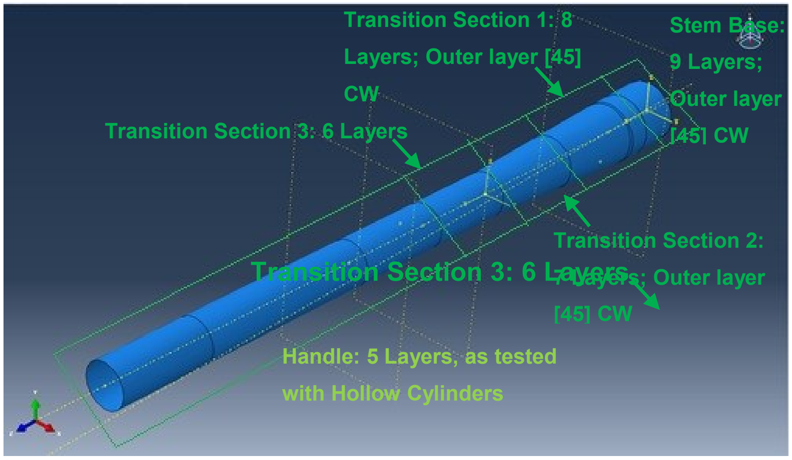

Figure 85 - Schematic of Handlebar Ply Drop-Off

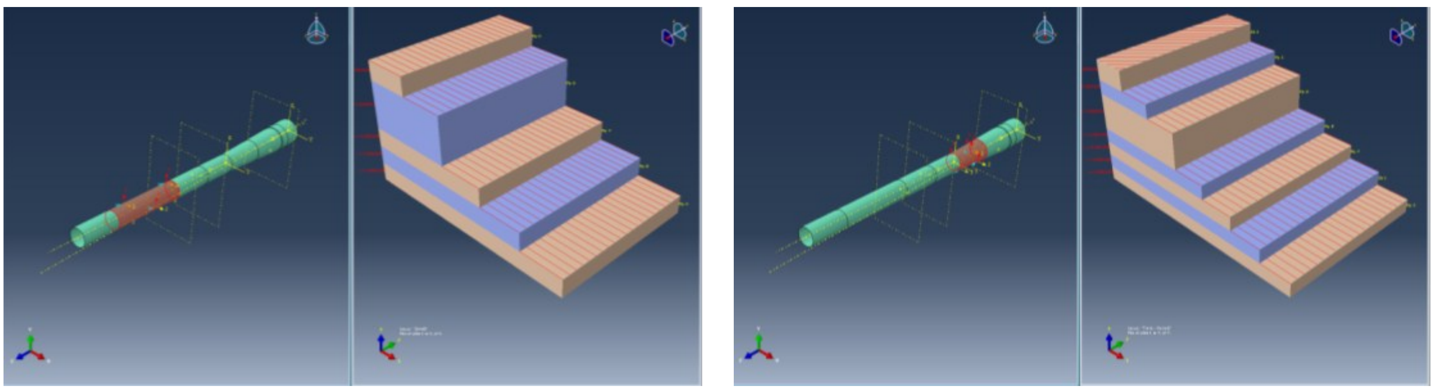

Figure 86 - Material Direction and Ply Stack Sequence for the Handlebar Model : FP3 Example
Left: Assigned Material Direction [1 (Blue – Longitudinal), 2 (Yellow – Radial), 3 (Red – through thickness)] for the Handle Section and associated Ply Stack Schematic
Right: Assigned Material Direction for the Transition Section 2 and associated Ply Stack Schematic

6.2 Results

The static and dynamic behaviour of the modeled hybrid laminates are shown below in Table 23 and Table 24.

Table 23 - Static Failure Criterion and Tip Deflection of Hybrid Laminate Handlebars

Sample Name	HSNFCCRT	HSNFTCRT	HSNMCCRT	HSNMTCRT	Deflection [m]
BH	0.35	0.05	0.41	0.31	0.026
Flax Layer Placement Samples					
FP1	0.53	0.07	0.29	0.39	0.016
FP2	0.51	0.07	0.28	0.39	0.016
FP3	0.52	0.07	0.29	0.40	0.016
FP4	0.55	0.07	0.30	0.42	0.016
Multiple Flax Layer Placement Samples					
DF1	0.64	0.09	0.29	0.41	0.017
DF2	0.62	0.09	0.33	0.42	0.017
DF3	0.63	0.09	0.31	0.46	0.018
DF4	0.64	0.09	0.33	0.42	0.017
DF5	0.63	0.09	0.32	0.45	0.017

Where the Hashin-Rotem Failure Criterion are as follows:

Hashin-Rotem Failure Criterion	
HSNFCCRT	Fiber Compressive Initiation Criterion
HSNFTCRT	Fiber Tensile Initiation Criterion
HSNMCCRT	Matrix Compressive Initiation Criterion
HSNMTCRT	Matrix Tensile Initiation Criterion
If the criterion value < 1.0, means that the criterion has not been satisfied, and a safety factor exists	
If the criterion value > 1.0, means that the failure criterion *has* been met, and failure has occurred	

Table 24 - Natural Frequencies [Hz] of Hybrid Laminate Handlebars

Sample Name	First	Second	Third	Fourth	Fifth
BH	317.73	318.52	1620.2	1624.9	2804.3
Flax Layer Placement Samples					
FP1	354.38	355.1	1455.5	1579.3	1582.2
FP2	352.6	353.31	1446.5	1570.8	1573.7
FP3	350.77	351.46	1437.3	1562	1564.9
FP4	348.83	349.5	1427.8	1552.5	1555.3
Multiple Flax Layer Placement Samples					
DF1	313.59	314.21	1341.1	1416	1418.6
DF2	310.08	310.68	1324.6	1398.8	1401.3
DF3	306.38	306.95	1307.3	1380.2	1382.6
DF4	311.81	312.41	1332.6	1407.2	1409.7
DF5	308.15	308.74	1315.7	1388.9	1391.4

The associated mode shapes are shown below in Figure 87. Note that as in the hollow cylinder model, the mode shape for the Benchmark handlebar for the third (expansion about the longitudinal axis) and fourth/fifth (deflection about the y- and z- axis) are reversed from the hybrid laminates.

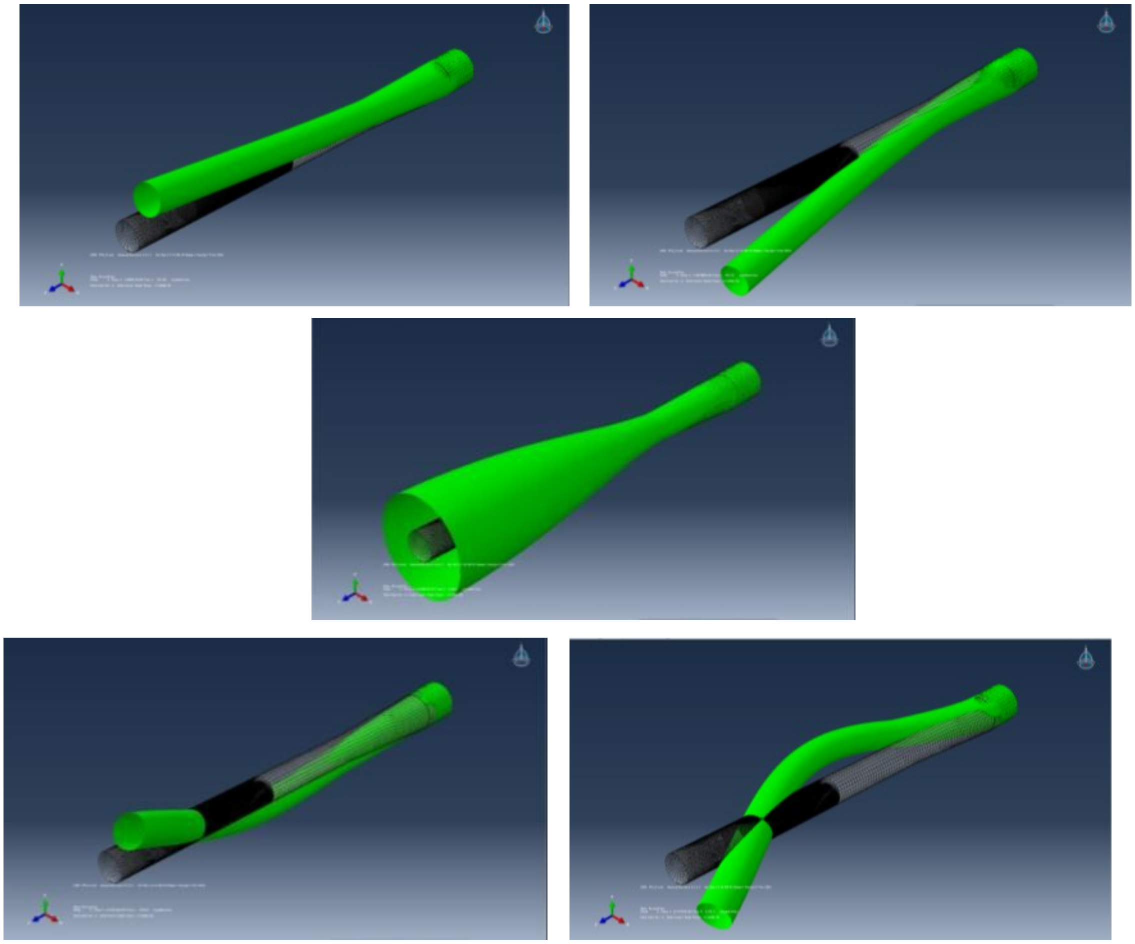

Figure 87 - Modal Shapes for Handlebar
Top: First *(Left)* and Second *(Right)* Modal Shape; *Centre:* Third Modal Shape; *Bottom:* Fourth *(Left)* and Fifth *(Right)* Modal Shape. Note for Sample BH the Third and Fourth/Fifth modal shapes were reversed.

6.2.1 Manufacturing of Demonstration Handlebar

Using the methodology described in Section 3.2, the demonstration handlebar was manufactured with the following complete layup, where ‘C’ denotes unidirectional carbon fiber, ‘F’ denotes unidirectional flax fiber, and ‘CW’ denotes plain weave carbon fiber.

Stem Base: $[0_{4\_C}/0_{2\_F}/0_{2\_C}/45_{CW}]_T$

Transition 1: $[0_{3\_C}/0_{2\_F}/0_{2\_C}/45_{CW}]_T$

Transition 2: $[0_{2\_C}/0_{2\_F}/0_{2\_C}/45_{CW}]_T$

Transition 3: $[0_{2\_C}/0_{2\_F}/0_{2\_C}]_T$

Handle: $[0_C/0_{2\_F}/0_{2\_C}]_T$

The final product is shown below in Figure 88.

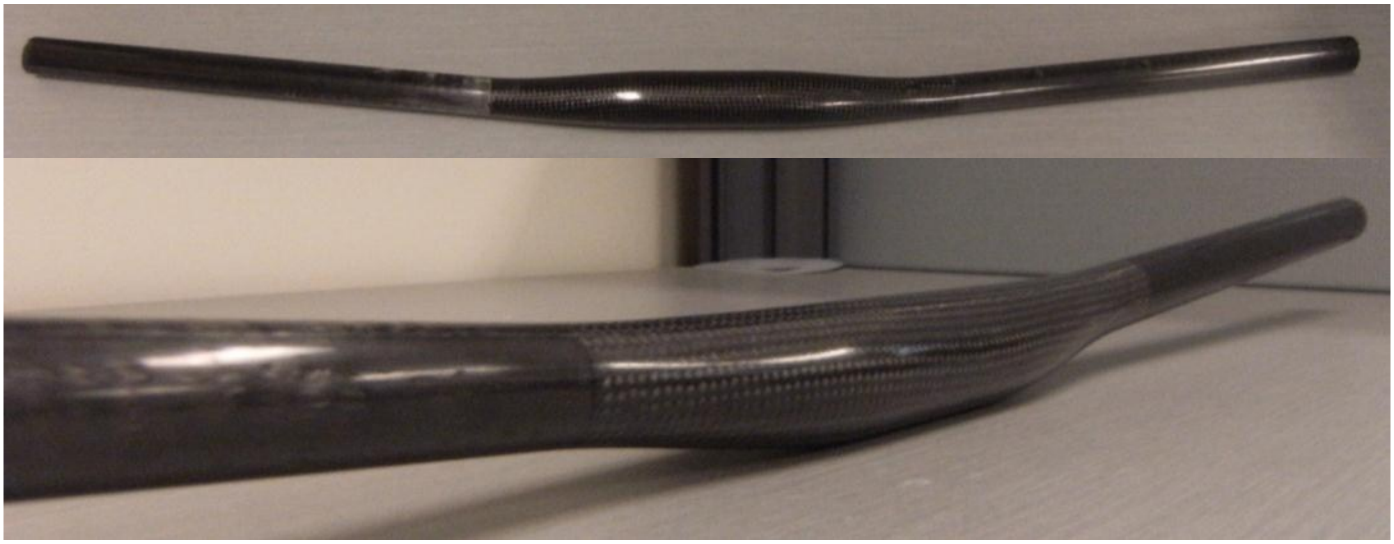

Figure 88 - Demonstration Handlebar
Top: Full Handlebar; *Bottom:* Side View

6.3 Discussion

From Table 23 although the safety factor of all laminates is greater than the benchmark handlebar, all satisfy the Hashin-Rotem Failure Criterion, and thus the flexural strength requirements. Interestingly, the maximum tip deflection for all the hybrid composites is approximately 1.7cm, half that of the benchmark handlebar at 2.6cm. Therefore, all hybrid laminates exceed the performance of the benchmark handlebar with respect to maximum tip deflection.

From Table 24 we can observe that the predicted natural frequencies of the hybrid composite handlebars exceed the human threshold of 8-100Hz, similar to the simplified hollow cylinder specimens. From inspection, the hybrid laminate handlebars have predicted natural frequencies approximately 100Hz greater than that of the modeled clamped hollow cylinder. As previously discussed, the natural frequencies of the clamped specimens were shown to follow the rule of mixtures, regardless of the flax position. Therefore, as the hybrid handlebar has four additional partial layers of carbon fiber, the hybrid handlebar natural frequencies agree with hypothesized predictions of performance based on the simplified cylinder geometry.

Based on the model results, all selected hybrid laminate designs meet the failure criterion as defined by the Hashin-Rotem Failure Criterion. Additionally, all hybrid designs exceed the maximum deflection performance of the benchmark handlebar design. Therefore, the hybrid laminates can be used to optimize the damping behaviour of the handlebar without compromising their strength performance. The optimized handle hybrid laminate of [$C/F_2/C_2$] with enhanced damping characteristics is predicted to result in a superior handlebar that meets and exceeds the current benchmark performance.

Subsequent to the manufacturing of the demonstration handlebar, numerous process improvements were identified, to be explored in future work. The primary suggestions for improvement are as follows:

1) *Net-Shape specific mandrel:* In this procedure, a straight mandrel was used for ply layup. This was difficult due to the local changes in thickness: as designed, there are five different thickness zones. Additionally, it was very difficult to centre the laminates using the straight mandrel due to their varying lengths. Therefore, for accuracy and ease of preparation, a net-shaped mandrel made of either silicon or foam is suggested for future use.
    a. <u>Silicon mandrel:</u> The mandrel geometry would be the handlebar net shape, with a maximum centre radius dimension smaller than the smallest inner radius, to allow for mandrel removal post-cure. The mandrel would be inserted into the pressure bladder prior to layup. The ply layers would then be applied as using the straight mandrel. The mandrel would remain in the bladder during the cure cycle, with the internal bladder pressure of 60psi. Subsequent to cure, the mandrel would be removed from one end (45).
    b. <u>Expanding foam core:</u> The foam mandrel would be designed and dimensioned such that during the cure cycle the foam would expand and apply an internal pressure of 60psi. This would simplify the manufacturing process, as no pressure bladder would be required. Subsequent to cure, the foam could be removed mechanically, through drilling and/or scraping methods. Foam cores are currently used to manufacture the ITM Aries NM Carbon Road Bicycle Handlebar (56).

2) *Bladder Removal:* For the final product, it would be aesthetically beneficial if the pressure bladder could be removed. Although it is insignificant with respect to performance, the final product would look cleaner without the inner bladder. Bladder removal was attempted by applying release agent to the bladder prior to layup. Although the bladder could be twisted at either end, the entire bladder could not be removed due to the handlebar length. Therefore, it is suggested that stronger release agent be applied to the surface of the bladder, or a change in bladder material to allow for removal. In the case of the foam core, release film could be loosely wrapped around the foam mandrel. This would also assist in the foam removal subsequent to cure.

7 Summary

Development in natural fiber composites is being driven predominately by increasing concern of the environmental impact of current manufacturing processes and materials. There is little known about the dynamic behaviour of natural fiber composites, and very little with regards to hybrid synthetic/natural fiber reinforcement behaviour. Dynamic properties such as damping are of special interest to the sports industry, where the demands of both strength and comfort are required by the users for optimal feel and performance. Previous development in the bicycle industry has focused on improving the strength-to-weight ratio, to enhance power transfer. This focus has come at the cost of damping, resulting in increased discomfort of the rider. Previous work in the area of rider discomfort has focused on structural response to experimental or road trial simulations, neglecting the area of material classification. Due to the complex interactions between the material, structure, and user, an understanding as to the baseline material performance in vibration is required for optimal design. The purpose of this investigation was to determine the differences in dynamic behaviour of hybrid flax/carbon fiber reinforced composites in the complex hollow cylinder geometry for the purposes of a mountain bicycle handlebar. This was achieved through experimental investigation of simple hollow cylinders of two groups of hybrid composites: one group to investigate the effect of the flax layer on performance and one group to investigate the effect of multiple flax layers. It was found experimentally that the boundary condition has a significant impact in the resulting damping and time to equilibrium behaviour of the specimens. In the free-free boundary condition, the optimum laminate was found to be [$C/F/C_3$], with a damping factor of 8.69%. In the clamped boundary condition, the optimum laminate was found to be [$C/F_2/C_2$], with a damping factor of 1.63%. All specimens had natural frequencies greater than the perceived human sensitivity range of 8-100Hz at the hand/handlebar interface. To further understand the prominent damping mechanisms of the samples, the through-thickness strain energy was modeled. It was shown that the damping behaviour is dependent on the mode shape of the natural frequency. Contrary to previous publication of sandwich structures, the total through-thickness strain energy was not indicative of the damping characteristics, but rather the relative difference between the damping flax layer and surrounding carbon fiber layer was significant. The position and thickness of the flax layer(s) was also shown to be significant, with the optimal position of the complaint flax layers located closest to the inner surface. This result agrees with previous literature. The model results indicate that the prominent structural damping mechanism in a clamped hollow cylinder hybrid composite is most likely interlaminar strain between the outer flax/carbon interface coupled with the flax fiber unique damping characteristics. Finally, the proposed optimal laminate based on the dynamic characteristics was modeled to verify that the design met the static strength requirements. The optimal design laminate met the Hashin-Rotem safety criterion for failure and had a 155% improvement in maximum deflection when compared to the benchmark handlebar. This design was successfully manufactured as a proof-of-concept design and showcased at the Composites Europe 2014 trade show.

8 Future Work

The results of this investigation are significant contributions to the area of natural fiber composites, hybrid composites, and their dynamic properties. Further work in this field is required in the following three key focal areas:

1) *Further investigation of the dynamic properties of hollow cylinders:* Experimental validation of the results in the free-free and clamped boundary conditions could be refined by using acoustic stimuli in a sound-proof environment. An acoustic sweep could first identify the natural frequencies, and then the stimuli could be tuned to each natural frequency to experimentally validate and determine the damping factor for each. This study should be conducted with a sample set of five or more for statistically significant results.
2) *Further investigation of through-thickness strain energy density:* A more comprehensive study for the whole structure is required, and should be generated to correlate to each natural frequency and damping factor as determined using the suggested acoustic method. This investigation may further illustrate the dominant damping mechanisms of a hollow hybrid composite cylinder and their dependence on the mode shape for that specific natural frequency. This investigation may also result in determining the dominant natural frequency and mode shape during impact stimulation.
3) *Further handlebar experimental testing:* The proposed design should be experimentally validated as follows:
    a. Dynamic testing as per the acoustic method described above to verify dynamic behaviour and also to correlate the hollow cylinder performance to the handlebar geometry performance. This would give an indication as to the effect of the change in geometry and laminate thickness on dynamic properties.
    b. Flexural testing as per EN 14766 to verify model predictions of behaviour
    c. Fatigue testing as per EN 14966 to ensure standard compliance

The resulting investigation and knowledge could be applied to other damping structures including but not limited to: sports equipment, pipelines, pressure vessels, civil structures, and automobile components.

9 References

(1) Fiore V, Valenza Al, Di Bella G. Mechanical Behaviour of Carbon/Flax Hybrid Composites for Structural Applications. Journal of Composite Materials 2012;46(17):2089-2096.

(2) Biagiotti J, Puglia D, Kenny JM. A Review on Natural Fiber-Based Composites - Part I. Journal of Natural Fibers 2004;1(2):37-68.

(3) Puglia D, Biagiotti J, Kenny JM. A Review on Natural Fiber-Based Composites - Part II. Journal of Natural Fibers 2005;1(3):23-65.

(4) Jawaid M, Abdul Khalil HPS. Cellulosic/Synthetic Fibre Reinforced Polymer Hybrid Composites: A Review. Carbohydrate Polymers 2011;86:1-18.

(5) Summerscales J, Dissanayake N, Virk A, Hall W. A Review of Bast Fibres and their Composites. Part 2 - Composites. Composites: Part A 2010;41:1336-1344.

(6) European Standard EN 14766:2006-09. Mountain Bicycles – Safety Requirements and Test Methods. European Committee for Standardization. 2006.

(7) Directive 2000/53/EC of the European Parliament and of the Council on End-Of-Life Vehicles. 2000;2000/53/EC.

(8) Meredith J, Ebsworth R, Coles SR, Wood BM, Kirwan K. Natural Fiber Composite Energy Absorption Structures. Composites Science and Technology 2012;72:211-217.

(9) Meredith J, Coles SR, Powe R, Collings E, Cozien-Cazuc S, Weager B, et al. On the Static and Dynamic Properties of Flax and Cordenka Epoxy Composites. Composites Science and Technology 2013;80:31-38.

(10) Ku H, Wang H, Pattarachaiyakoop N, Trada M. A Review on the Tensile Properties of Natural Fiber Reinforced Polymer Composites. Composites: Part B 2011;42:856-873.

(11) Phillips S, Baets J, Lessard L, Hubert P, Verpoest I. Characterization of Flax/Epoxy Prepregs Before and After Cure. Journal of Reinforced Plastics and Composites 2013;32(11):777-785.

(12) Anandjiwala RD, Blouw S. Composites from Bast Fibres – Prospects and Potential in the Changing Market Environment. Journal of Natural Fibers 2007;4(2):91-109.

(13) Duc F, Bourban PE, Plummer CJG, Manson J-E. Damping of Thermoset and Thermoplastic Flax Fibre Composites. Composites: Part A 2014;64:115-123.

(14) Abdel-Halim ES, El-Rafie MH, Kohler R. Surface Characterization of Differently Pretreated Flax Fibers and Their Application in Fiber-Reinforced Composites. Polymer-Plastics Technology and Engineering 2007;47(1):58-65.

(15) Faruk O, Bledzki AK, Fink H, Sain M. Biocomposites Reinforced with Natural Fibers: 2000-2010. Progress in Polymer Science 2012;37:1552-1596.

(16) Dhakal HN, Zhang ZY, MacMullen J, Bennett N. Development of Flax/Carbon Fibre Hybrid Composites for Enhanced Properties. Carbohydrate Polymers 2013;96:1-8.

(17) S. Phillips. Characterization of Flax Fibres for Application in the Resin Infusion Process McGill University; 2013.

(18) Goutianos S, Peijs T, Nystrom B, Skrifvars M. Development of Flax Fibre based Textile Reinforcements for Composite Applications. Appl. Composite Mater 2006;13:199-215.

(19) Shah DU, Schubel PJ, Clifford MJ, Licence P. The Tensile Behaviour of Off-Axis Loaded Plant Fiber Composites: An Insight on the Nonlinear Stress-Strain Response. Polymer Composites 2012;43(9):1495-1504.

(20) Phillips S, Lessard L. Application of Natural Fiber Composites to Musical Instrument Top Plates. Journal of Composite Materials 2011;46(2):145-154.

(21) Yan L, Chouw N, Jayaraman K. On Energy Absorption Capacity, Flexural and Dynamic Properties of Flax/Epoxy Composite Tubes. Fibers and Polymers 2014;15(6):1270-1277.

(22) Chandra R, Singh SP, Gupta K. Damping Studies in Fiber-Reinforced Composites – A Review. Composite Structures 1999;46:41-51.

(23) Yan L. Effect of Alkali Treatment on Vibration Characteristics and Mechanical Properties of Natural Fabric Reinforced Composites. Journal of Reinforced Plastics and Composites 2012;31(13):887-896.

(24) Kakogiannis D, Chung Kim Yuen S, Palanivelu S, Van Hemelrijck D, Van Paepegem W, Wastiels J, et al. Response of Pultruded Composite Tubes Subjected to Dynamic and Impulsive Axial Loading. Composites: Part B 2013;55:537-547.

(25) Damping Properties of Unidirectional Flax and Carbon Composites. SURE Poster Presentation Fair; 2014.

(26) Bagheri ZS, Sawi IE, Schemitsch EH, Zdero R, Bougherara H. Biomechanical Properties of an Advanced New Carbon/Flax/Epoxy Composite Material for Bone Plate Applications. Journal of the Mechanical Behaviour of Biomedical Materials 2013;20:398-406.

(27) Inman DJ. Engineering Vibration. 2nd Edition ed. Upper Saddle River, NJ.: Pretence Hall; 2001.

(28) Vanwalleghem J. Study of the Damping and Vibration Behaviour of the Flax-Carbon Composite Bicycle Racing Frames. 2010.

(29) Van Vuure AW, Verpoest I, Ko. FK. Sandwich-fabric Panels as Spacers in a Constrained Layer Structural Damping Application. Composites: Part B 2001;32:11-19.

(30) Vanwalleghem J, Mortier F, De Baere I, Loccufier M, Van Paepegem W. Design of an Instrumented Bicycle for the Evaluation of Bicycle Dynamics and its Relation with the Cyclist's Comfort. Procedia Engineering 2012;34:485-490.

(31) ISO 2631-2:2003. Mechanical Vibration and Shock - Evaluation of Human Exposure to Whole-Body Vibration - Part 2: Vibration in Buildings (1 Hz to 80 Hz). 2013.

(32) ISO 5349-1:2001. Mechanical Vibration - Measurement and Evaluation of Human Exposure to Hand-Transmitted Vibration - Part 1: General Requirements. 2011.

(33) Pradko F, Lee R, Kaluza V. Theory of Human Vibration Response. 1966.

(34) Griffin MJ. Handbook of Human Vibration. San Diego, CA: Academic Press Inc.; 1990.

(35) Griffin MJ. Chapter 25: Vibration and Motion. In: Salvendry G, editor. Handbook of Human Factors and Ergonomics. Second Edition ed. New York, NY: John Wiley & Sons; 1997. p. 828-857.

(36) Experimental Evaluation of Vibration Comfort for a Residential Environment. IMAC-XX Conference and Exposition on Structural Dynamics; 2002.

(37) Mortier F. Evaluation of the Dynamic Behaviour of Composite Racing Bicycles through Outdoor Field Testing. 2011.

(38) Modal Analysis of a Road Bike's Front Components. SEC-IMAC XXII: Conference and Exposition on Structural Dynamics; 26-29 January 2004; ; 2004.

(39) Thite AN, Gerguri S, Coleman F, Doody M, Fisher N. Development of an Experimental Methodology to Evaluate the Influence of a Bamboo Frame on the Bicycle Rider Comfort. Vehicle System Dynamics: International Journal of Vehicle Mechanics and Mobility 2013;51(1):1-18.

(40) Gribb TT, Worzala FJ, Gribb GW. Modeling Bicycle-Rider Vibrations: Implications for Materials Selection. MRS Bulletin 1998;23(3):56-58.

(41) Seifert JG, Luetkemeier MJ, Spencer MK, Miller D, Burke ER. The Effects of Mountain Bike Suspension Systems on Energy Expenditure, Physical Exertion, and Time Trial Performance during Mountain Bicycling. International Journal of Sports Medicine 1997;18(3):197-200.

(42) Development of a Metric Related to the Dynamic Comfort of a Road Bike. SEC-IMAC XXIV: Conference and Exposition on Structural Dynamics.; 30 January – 2 February 2006; ; 2006.

(43) Hay K. The Effect of Damping Behaviour of Bicycle Design on Cyclist Performance. 2013.

(44) Thomson Bike Products. MTB Carbon. 2014; Available at: http://bikethomson.com/mtb-carbon/.

(45) Bonvin Y, Burger M. Herstellung und Auslegung eines Fahrradlenkers. 2013.

(46) ASTM D5450-12. Standard Test Method for Transverse Tensile Properties of Hoop Wound Polymer Matrix Composite Cylinders. 2012.

(47) ASTM D3039-08. Standard Test Method for Tensile Properties of Polymer Matrix Composite Materials. 2008.

(48) ASTM D3410-03. Standard Test Method for Compressive Properties of Polymer Matrix Composite Materials with Unsupported Gage Section by Shear Loading. 2008.

(49) Chang RR. Finite Element Analyses and Experimental Considerations of the Deflection and Failure Behaviour of an Asymmetric Laminate Composite Bicycle Handlebar. Proceedings of the Institution of Mechanical Engineers, Part E: Journal of Process Mechanical Engineering 2002;216:207-218.

(50) Firehole Composites. Between the Plies: Solutions for Obtaining Unidirectional Composite Material Properties for a FEA Simulation.

(51) Dessault Systems. Abaqus Analysis User's Manual 6.11, Section 23.3.2: Damage Initiation for Fiber-Reinforced Composites. 2011; Available at: http://abaqus.ethz.ch:2080/v6.11/books/usb/default.htm.

(52) Flax and Hemp Fibers: A Natural Solution for the Composites Industry. 2012.

(53) ASTM C1259-08. Standard Test Method for Dynamic Young's Modulus, Shear Modulus, and Poisson's Ratio for Advanced Ceramics by Impulse Excitation of Vibration. 2012.

(54) Dynamic Properties of Hybrid Composite Hollow Cylinders: Application for Mountain Bicycle Handlebars. Canada-Japan Workshop on Composites; 2014.

(55) Vanwalleghem J, De Baere I, Loccufier M, Van Paepegem W. External Damping Losses in Measuring the Vibration Damping Properties in Lightly Damped Specimens Using Transient Time-Domain Methods. Journal of Sound and Vibration 2014;333:1596--1611.

(56) ITM. Aries NM Carbon Handlebar. 2014; Available at: http://bikecycle.co.nz/components/handlebars/road/aries-nm-carbon-handlebar/.

10 Appendix A: Static Strength Test Fixtures

The design specifications for the custom test fixtures used in tensile and compressive strength testing (Section 4) are shown below in Figure 89 and Figure 90.

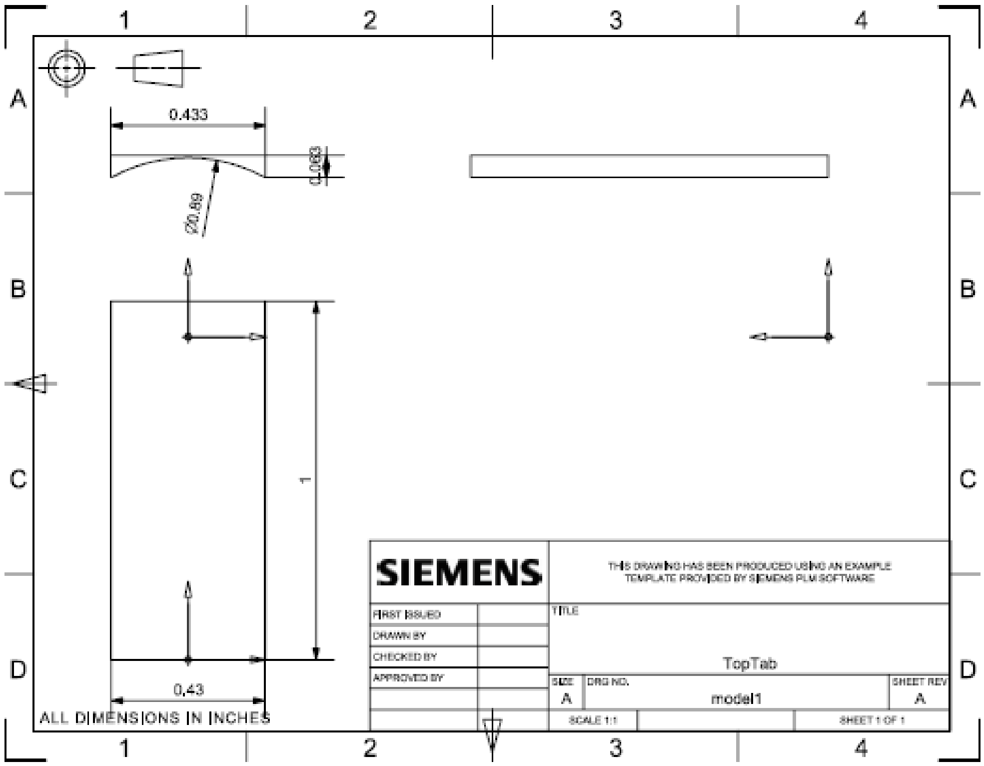

Figure 89 - Drawing of Top Tab for Static Strength Fixture

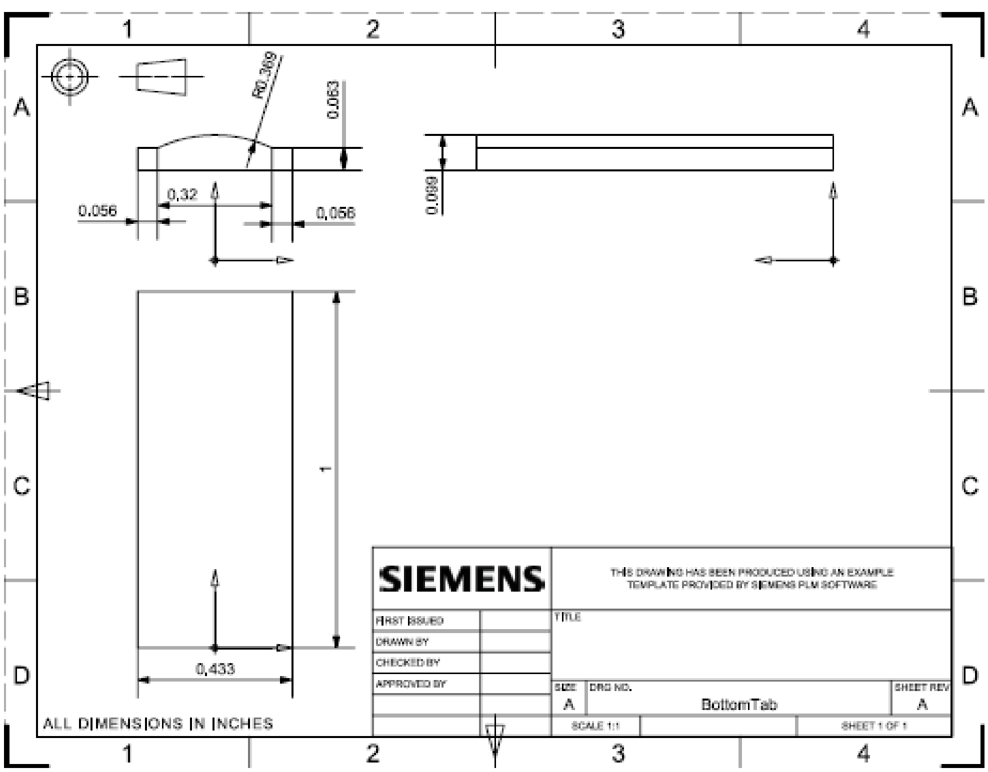

Figure 90 - Drawing of Bottom Tab for Static Strength Fixture